Tailored Formulation of Capillary Suspensions as Precursor for Porous Sintered Materials

zur Erlangung des akademischen Grades eines
DOKTORS DER INGENIEURWISSENSCHAFTEN (Dr.-Ing.)

der Fakultät für Chemieingenieurwesen und Verfahrenstechnik des
Karlsruher Institut für Technologie (KIT)

genehmigte
DISSERTATION

von
Dipl.-Ing. Johannes Maurath
aus Bühl (Baden)

Referent: Prof. Dr. Norbert Willenbacher
Korreferent: Prof. Dr.-Ing. Matthias Kind
Tag der mündlichen Prüfung: 05.03.2018

Preface

This publication based dissertation consists of five peer-reviewed articles published in scientific journals. They include the main results of my experimental work at the Karlsruhe Institute of Technology (KIT), Institute of Mechanical Process Engineering and Mechanics in the group of Applied Mechanics during September 2013 and February 2017.
The main part of this dissertation follows a brief introduction to the state of the art on porous materials in general and the recently developed processing route for manufacturing highly porous sintered materials based on capillary suspensions. It consists of the following publications:

1. Influence of particle shape on the rheological behavior of three-phase non-Brownian suspensions,
2. Fabrication of highly porous glass filters using capillary suspension processing,
3. Highly porous materials with unique mechanical properties from smart capillary suspensions,
4. Suppressing crack formation in particulate systems by utilizing capillary forces, and
5. 3D printing of open-porous cellular ceramics with high specific strength.

The dissertation concludes with a general summary, an outlook as well as a bibliography. The bibliography includes all references of the publications. Hereby the publications are slightly changed. The participation of other authors in the publications is exemplified in detail in chapter 11. For the reason of better readability, the term “we” is used in all chapters of this dissertation.

Acknowledgements

I would like to take the opportunity to thank all people who contributed to my dissertation due to active help on experimental work, fruitful discussions or general support in all cases during my time at the Karlsruhe Institute of Technology.

First of all I would like to thank Prof. Dr. Norbert Willenbacher for giving me the chance to write my dissertation at the Institute for Mechanical Process Engineering and Mechanics in the group of Applied Mechanics. The fruitful and creative discussions about new ideas and theoretical backgrounds in all fields were an important contribution to my dissertation. Furthermore, I would like to thank Prof. Dr.-Ing. Kind from the Institute of Thermal Process Engineering at the KIT for being my second referee.

Further thanks are given to Prof. J. Lewis from Harvard University (Cambridge, USA) for giving me the great chance to work for two months in her group at the School of Engineering and Applied Sciences. Here, I would also like to thank Joseph Muth for assisting me with organizational and experimental things to have a great and successful time abroad.

Thanks to the Schott AG, and to Dr. N. Schultz for the nice cooperation during the glass filter project, and to Dr. W. Bauer from the Institute of Material Process Technology of the KIT for the fruitful discussions.

It was a pleasure for me to work with the students Daniel Müller, Yvonne Schwegler, Monika Wolf, Kathrin Dyhr, Felix Braun, Moritz Weiß, and Vinzenz Rogg who wrote their bachelor or master thesis as a part of my project.

Furthermore, I would like to thank Dr. Bernhard Hochstein for helping me on technical and organizational questions, as well as the technical staff including Karsten Sasso, Thomas Lebe, Klaus Hirsch, and Astrid Huber for help with technical constructions and analysis.

Special thanks also to all my colleagues at the Institute for Mechanical Process Engineering. It was a great time to work, discuss and party with all of you.

Great thanks I would like to give my parents Johanna and Wolfgang, my sister Melanie and my brother Stephan as well as my love Maria, who supported me all the time during my studies and my time as PhD student. Without your support it would not have been possible to write this thesis.

Contents

Notations

Latin symbols

B_0	constant of Gibson & Ashby model
C	constant
d_p	pore size
F_c	capillary force
g	function
G‘	storage modulus
G‘‘	loss modulus
h_{max}	critical cracking thickness
k	constant
k	permeability
k_g	gas permeability
k_l	liquid permeability
N_{bridge}	number of a capillary bridges
$p_{1..2}$	pressure
p_c	capillary pressure
p_M	pressure in the middle of a filter
q_3	density distribution
Q	volume flow
r	aspect ratio
r_c	radius of a cylindrical pore
R	particle radius
R_1	radius of the curvature of a capillary bridge
R_2	radius of the neck of a capillary bridge
$R_{50,3}$	average radius
s	separation distance
$\tilde{s}$	normalized particle separation
S	saturation
S_v	specific surface
t	time
t_{sinter}	sintering time
T	temperature

T	tortuosity factor
T_{sinter}	sintering temperature
V	capillary bridge volume
V_{bridge}	capillary bridge volume
x	diameter
$x_{50,3}$	average particle diameter, volume based
$x_{50,3}$	average pore diameter, volume based
$x_{particle}$	particle diameter
x_{pore}	pore diameter
$x_{pore,\ av}$	average pore diameter
z	constant of Gibson & Ashby model

Greek symbols

β	half filling angle
γ	deformation
γ	surface tension
γ_{2l}	interfacial tension
Γ	surface tension
$\Gamma_{B,a}$	surface tension of bulk fluid
$\Gamma_{S,a}$	surface tension of secondary fluid
$\Gamma_{S,B}$	interfacial tension of bulk fluid against secondary fluid
Δp	pressure drop
ε	porosity
ε_s	strut porosity
ε^*	true porosity
η	dynamic viscosity
θ	contact angle
θ_{2l}	two-liquid wetting angle
$\theta_{B,a}$	contact angle of bulk fluid against air
$\theta_{S,a}$	contact angle of secondary fluid against air
θ_{SB}	three phase contact angle
λ	wave length
ν	stretching resonance frequency
ρ	density
ρ_m	matrix density

ρ^*	overall density
σ	shear stress
σ_0	shear stress amplitude
$\sigma_{0,c}$	critical shear stress amplitude
σ_c	compressive strength
σ_y	yield stress
$\sigma_{y,0}$	yield stress of corresponding pure suspension
σ_f	flexural strength
$\sigma_{f,0}$	flexural strength of dense ceramic matrix material
$\sigma_{ts,m}$	tensile strength of matrix material
$\sigma_{ts,s}$	tensile strength of struts
σ^*	compressive strength
τ_0	stress amplitude
τ_y	yield stress
ϕ	volume fraction
ϕ_{sec}	volume fraction of secondary liquid
ϕ_{solid}	volume fraction of solid powder
ω	frequency

Abbreviations

ATR	attenuated total reflection
CCT	critical cracking thickness
CLSM	confocal laser scanning microscopy
CVD	chemical vapor deposition
DINP	diisononylphtalat
DIW	direct ink writing
HLB	hydrophilic-lipophilic balance
ICE	internal combustion engine
LVE	linear viscoelastic
MSA	minimum solid area
PCC	precipitated calcium carbonate
PVC	polyvinylchloride
RT	room temperature
SEM	scanning electron microscopy
SEM-BSE	SEM with detection of backscattered electrons

SEM-SE	SEM with detection of secondary electrons
UHMWPE	ultrahigh molecular weight polyethylene
vdW	van der Waals
ZTA	zirconia toughened alumina

1 General introduction

Macroporous sintered materials are used in various technical applications, e.g. as filtration membranes for processes with hot or chemical reactive media [1–4], catalyst supports [5,6], tissue-engineering scaffolds [6–8] or lightweight construction materials [6,9]. Industrial companies increasingly focus on porous ceramics and glasses from sintering processes for manufacturing high performance components that exhibit an excellent heat resistance, good chemical stability and high mechanical strength. In hot and chemical aggressive environments these ceramics and glasses are mechanical stable and show long life cycles. Numerous manufacturing processes for macroporous sintered materials are established, but especially the range of pore sizes < 10 µm at porosities > 50% is rarely covered. In 2013 Dittmann et al. [10] published an innovative and smart manufacturing process for covering this pore size - porosity range by using so-called capillary suspensions as precursors for sintered materials. This process is versatile, can be applied to all types of sintered materials and is based on standard unit operations.

Capillary suspensions are ternary disperse systems consisting of two immiscible liquid phases and a solid phase (ϕ_{solid} < 30 vol%), dispersed therein. One of the liquid phases, the so-called secondary liquid phase is added in small amounts (ϕ_{sec} < 5 vol%) and forms capillary bridges between the dispersed particles, surrounded by the bulk phase. A sample spanning particle network emerges, which is stabilized by the dominating capillary forces and prevents phase separation and sedimentation. These so-called *capillary suspensions* show a pronounced shear thinning behavior, are gel-like and exhibit a high yield stress, even if the pure suspensions were not gel-like before [11]. Various product formulations based on capillary suspensions have been reported, benefitting from the unique rheological flow properties and the stable sample-spanning particle network in capillary suspensions. Formulations range from low-fat chocolate spreads [12,13], over pastes for printed electronics [14] up to electrode slurries for lithium-ion battery electrodes [15]. This thesis focusses on capillary suspensions as precursors for highly porous sintered materials with an unprecedented pore size – porosity range (ε > 50% at x_{pore} < 10 µm) [10,16]. It focusses on adapting this concept to product formulations in the field of microfiltration and lightweight construction materials. This includes first a fundamental study on the dependency of rheology and microstructure of capillary suspensions on particle shape. Then we show strategies to tune mechanical strength and pore shape of sintered capillary suspensions. Subsequently we introduce sintered capillary suspensions that exhibit good properties for microfiltration purposes and show that capillary suspension based-pastes are excellent to

produce porous, crack-free coatings. Finally, we present a processing route for manufacturing cellular ceramics with high specific strength via 3D printing of ceramic capillary suspension based inks.

In this chapter we discuss the characteristics and economical significance of porous materials in industrial applications. Then, the most important manufacturing routes for highly porous inorganic materials are introduced and compared with sintered materials based on the capillary suspension concept developed by Dittmann et al. [10,16] which is the basis of the product formulations, developed within this thesis. Finally, this chapter closes with an outline and an overview about open questions that will be answered within this dissertation, consisting of five peer-reviewed publications.

1.1 State of the art

1.1.1 Porous sintering materials in industrial applications

Application of porous sintering materials diversifies widely with the material type, since thermal and chemical resistivity and mechanical properties of ceramics, metals and polymers vary strongly. Ceramics and glasses are next to metals the most important group of sintered materials. Typically, they exhibit a high thermal and chemical resistivity at a high mechanical strength, what makes them feasible for applications in extreme conditions.

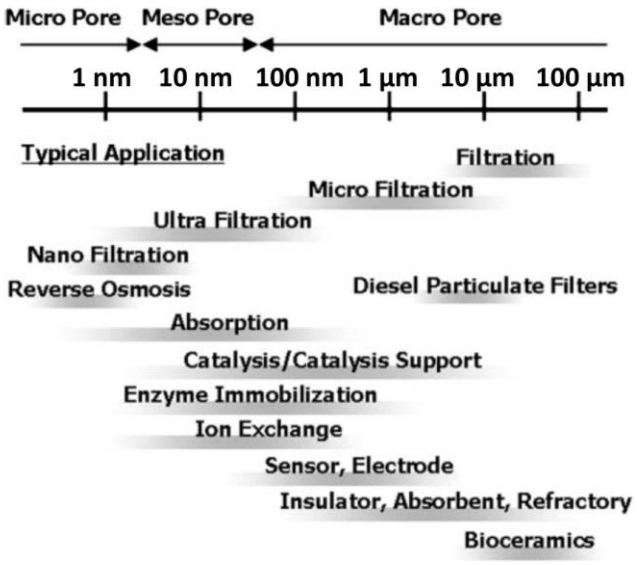

Fig. 1: Classification of porous materials by pore size. Several applications are mentioned and related to the particular pore size [17]. *Reproduced from Macro-porous ceramics: processing and properties, T. Ohji, M. Fukushima, International Materials Reviews 57 (2012) 115–131. Copyright © Institute of Materials, Minerals and Mining, reprinted by permission of Taylor & Francis Ltd (www.tandfonline.com) on behalf of Institute of Materials, Minerals and Mining.*

Both material type and structure of highly porous sintering materials determine the field of application. Open porous ceramics have a high accessible surface and a high permeability, closed porous materials exhibit a high resistance to thermal transport [18] and typically have a higher mechanical strength [19]. Also pore size x_{pore} is important for the particular application of the sintered materials. Generally, porous materials can be divided into three groups of materials, depending on the pore size: microporous (x_{pore} < 2 nm), mesoporous (2 < x_{pore} < 50 nm) and macroporous (x_{pore} > 50 nm) materials. Fig. 1 shows typical applications of porous materials and their requirements regarding average pore size between less than 1 nm and larger than 100 µm. Next to the pore size also porosity and pore structure (smoothness, tortuosity) have a strong impact on the specific application. In the case of macroporous filter media the performance of the specific filter medium is a function of pore size, porosity and pore structure. Pore size dictates the largest particle that passes the filter, while pore size, porosity and tortuosity all together determine the filtrate flux and consequently the energy consumption of the filtration process. However, for an optimum of functionality in a distinct application, the material type and the microstructure of a material, including pore size, porosity and tortuosity, have to be selected or designed wisely.

Up to now inorganic membranes find their applications in niche markets, but forecasts expect that inorganic membranes will play a significant role in the field of microfiltration not later than during the next 10 to 20 years [20]. Porous ceramics and glasses for filtration purposes are of high economic importance, since they show distinct advantages compared to other materials regarding life time, resistivity to extreme environments and filtrate flux. This eclipses disadvantages like enhanced manufacturing or material costs, clearly.

Further interesting industrial fields that have a high demand for highly porous ceramics are the sector of (lightweight) construction materials and catalysis. The latter market is growing monotonically [21] since it includes heterogeneous catalysis as well as the so-called environmental sector, where the demand for emission control catalysts in the automotive industry, like diesel oxidation catalysts, becomes more important.

1.1.2 Processing of macroporous ceramics and glasses

Various processing routes are established for fabrication of porous ceramics and glasses. All subsequently summarized manufacturing methods are sintering processes and apply to ceramics [17,22] as well as glasses. Common processes are partial sintering, the replica technique, the sacrificial template method and direct foaming. Porosity, pore size and pore structure (open or closed porosity) can be well controlled and depend strongly on the

manufacturing process. Fig. 2 schematically visualizes the main processing steps of established routes for manufacturing macroporous sintered materials.

The most common technique is *partial sintering*. Here, powdery materials are compacted into the desired shape and sintered until the requested porosity is reached. Hereby pore size and porosity of the specimens can be adjusted to obtain sintered parts with the required microstructural characteristics. Average pore size can be controlled by the particle size and particle size distribution of the used powder while porosity is a function of particle size distribution, forming pressure and thermal treatment. Generally, porosities $\varepsilon < 50\%$ and pore sizes < 10 µm are obtained by partial sintering [17].

The *replica technique* relies on the replication of porous organic structures. Natural or synthetic organic templates are filled with a suspension or a ceramic precursor (e.g. preceramic polymers, sols). After drying of the infiltrated templates, all organic components are burned in a debinding step. The sintering step follows to consolidate the replicated structure. Porosities up to 95% and pore sizes between 10 µm and 3 mm are accessible using this technique [6,22].

The *so-called sacrificial template method* is based on mixing a disperse phase into a ceramic suspension or a ceramic precursor (in solid or liquid form) that can be removed by pyrolysis or extraction. The removed disperse phase defines the macropores. The porous ceramic or preceramic scaffold is sintered afterwards. A wide range of sacrificial materials are applied as pore formers, including natural or synthetic organic materials, metals or salts. Due to this diversity of templates a broad range of porosities (20% - 90%) and pore sizes (1 µm - 700 µm) is available, but in most cases reported porosities are limited to $\varepsilon < 40\%$ at pore sizes < 10 µm [22]. Furthermore, liquids can serve as pore forming agents. In so-called Pickering emulsions, emulsion droplets are stabilized using ceramic particles with appropriate surface modification [18,23]. These stabilized suspensions serve as precursor for open or closed-porous ceramics with spherical pore size and a narrow pore size distribution is accessible. A further process where emulsion droplets may serve as pore forming agents is the sol-gel process. Here, surfactant stabilized oil droplets are dispersed in a sol that is gelled afterwards [24,25]. Pore sizes ranging from 200 nm to 100 µm and porosities up to 90% are obtainable. Nevertheless, the need of a strict control of the chemical reactions during the sol-gel process and the need of surface modified particles limit the use of liquids as pore forming agents and to our knowledge this approach is not used commercially so far.

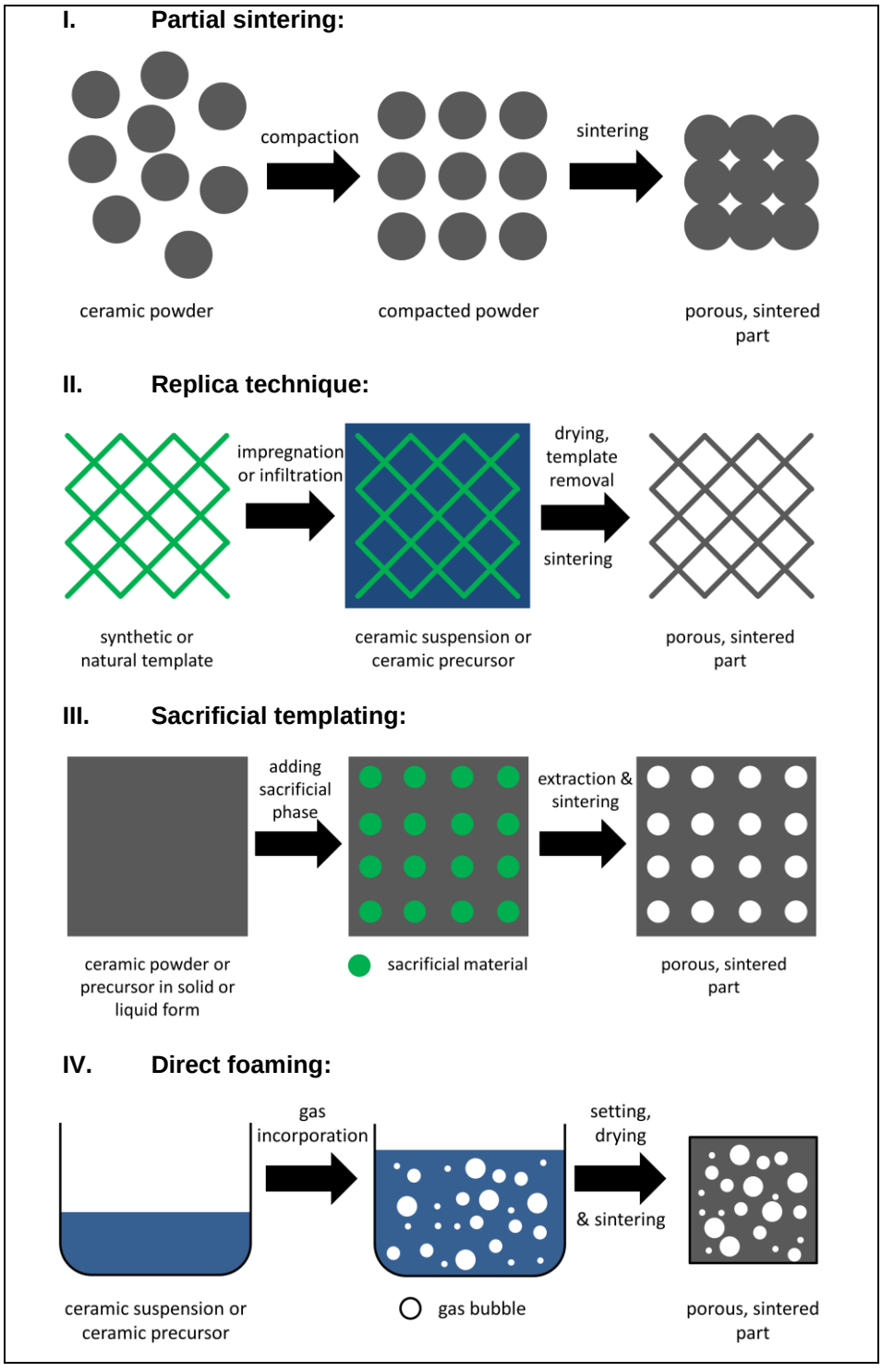

Fig. 2: Schematic of the four representative manufacturing processes for porous sintered ceramics and glasses [after [17,22]].

In the *direct foaming* process a ceramic suspension or preceramic solution gets foamed via gas intrusion or a chemical reaction and stabilized with surface-active substances like surfactants or colloidal particles. Afterwards the foam gets dried, debinded and sintered. Sintered foams exhibit high porosities (> 60%) and quite large pore sizes > 20 µm [22].

Fig. 3 summarizes porosities and pore sizes covered by the introduced conventional manufacturing methods. However, covering high porosities (ε > 50%) at small pore sizes ($x_{50.3}$ < 10 µm) concurrently is not economically available via common manufacturing methods. In the following chapter of this thesis we will introduce an innovative manufacturing process for macroporous ceramic materials using so-called capillary suspensions as precursors. The porosity/pore size region that is so far exclusively accessible by using this new process is marked in orange. Experimental data collected are shown as orange stars [10,16].

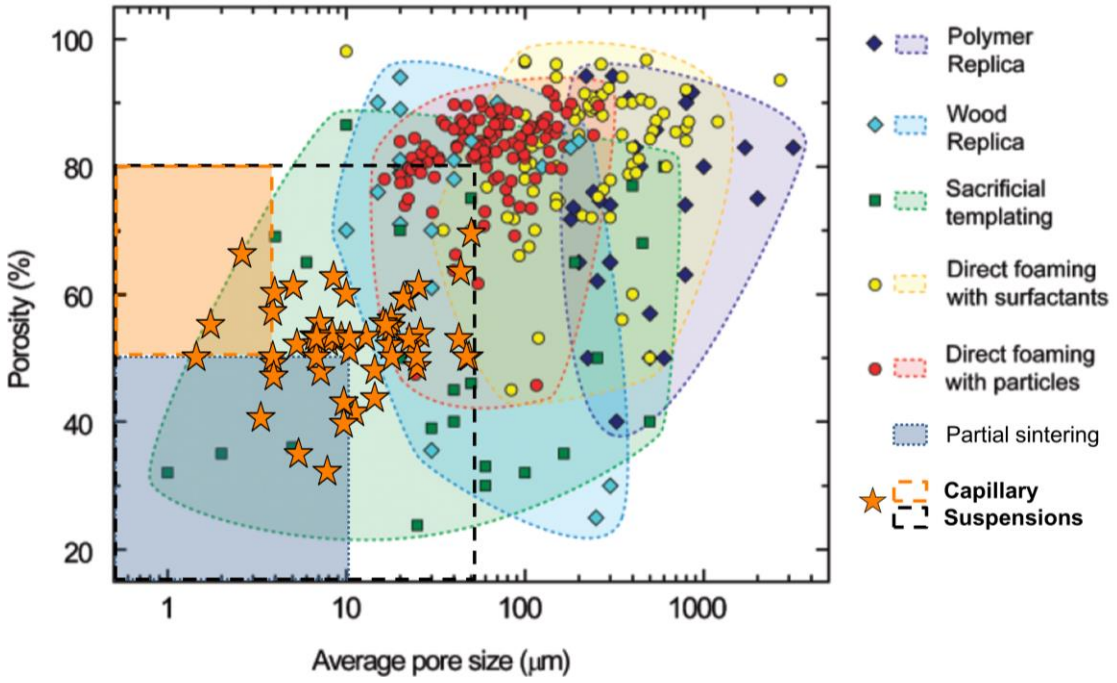

Fig. 3: Typical porosities and pores sizes via common manufacturing methods for macroporous ceramic materials. The dashed rectangle marks the area which can be reached so far via capillary suspensions [10,16]. The orange shaded area marks the field which is exclusively covered by samples made from capillary suspensions [adapted from [22] with [17]]. *Reproduced and adapted with permission from A.R. Studart, U. Gonzenbach, E. Tervoort, L. Gauckler, J. Am. Ceram. Soc. 89 (2006) 1771–1789. © 2006 The American Ceramic Society.*

1.1.3 Highly porous ceramics based on capillary suspensions

I. Capillary suspensions

Capillary suspensions are ternary systems consisting of solid particles suspended in two immiscible fluid phases and represent a distinct class of new materials. After addition of an appropriate secondary fluid to a suspension a sample spanning network of particles connected via capillary bridges occurs and the rheological behavior of the suspension changes from fluid or weakly elastic to gel-like, cf. Fig. 4. This phenomenon not only alters the rheology of the system, it also stabilizes the suspension. Settling and phase separation are prevented since particles are trapped in the network [11].

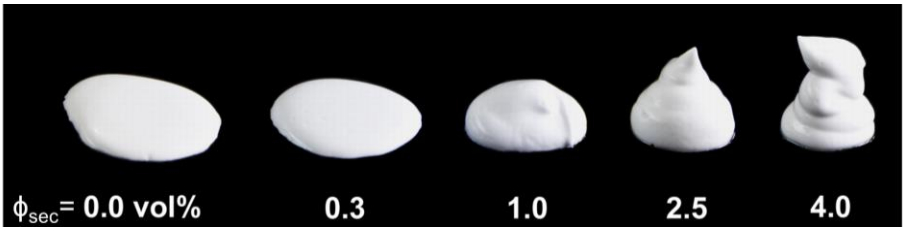

Fig. 4: Transition from fluid like, weakly elastic to highly elastic, gel-like state upon addition of an appropriate secondary fluid to an oil-based ceramic suspension (α-Al_2O_3, $x_{particle}$ = 1.6 µm, ϕ_{solid} = 20 vol%). The added secondary phase is an aqueous sucrose-solution (1.9 M) [10]. *Reproduced with permission from J. Dittmann, E. Koos, N. Willenbacher, J. Am. Ceram. Soc. 96 (2013) 391–397. © 2012 The American Ceramic Society.*

One of the fluid phases, the so called bulk phase, fills nearly the whole liquid volume. The secondary fluid phase occupies only a small fraction of the liquid volume (< 5 vol%). In analogy to wet granular media, two types of capillary suspensions are defined: The *pendular state* where the secondary phase preferentially wets the particles ($\theta_{S,B}$ < 90°) and forms pendular shaped bridges between the particles and the *capillary state* where the secondary phase does not preferentially wet the particles ($\theta_{S,B}$ > 90°). In this latter case the particles form clusters around small volumes of the second liquid [11]. Here, we will focus on the *pendular state*, since nearly all used material systems within this dissertation are in this state [10,16]. Fig. 5a shows a confocal image of the sample spanning network in a capillary suspension in the pendular state. The typical structure in pendular suspensions gets visible. The image is taken from a suspension with dyed secondary liquid (yellow) and dyed glass beads (red), the bulk phase appears black [26].

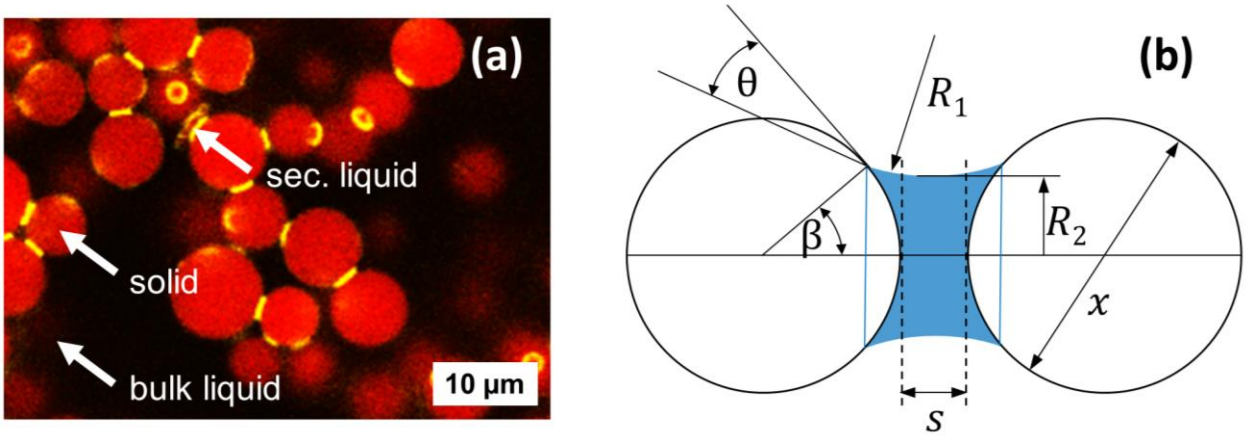

Fig. 5: (a) Two-dimensional confocal image of a capillary suspension. The spherical particles are interconnected by capillary bridges of the secondary phase. Solid phase (red): glass beads $x_{particle}$ = 6.4 µm, bulk phase: oil, secondary phase (yellow): water/glycerol mixture [26]. *Reproduced and adapted with permission from F. Bossler, E. Koos, Langmuir, 32 (2016) 1489–1501 (link). © 2016 American Chemical Society. For further permissions please contact ACS.* (b) Schematic of a pendular capillary bridge between two spherical particles.

In a pure suspension, the particles are either well dispersed or they form already a sample-spanning fractal network due to dominating van der Waals (vdW) attraction. Upon addition of the secondary fluid, capillary bridges between particles are formed, leading to a strong sample-spanning particle network. Fig. 5b shows a pendular liquid bridge between two spherical particles in air to illustrate the principle correlations in capillary networks that can be transferred to capillary suspensions. Here, θ is the contact angle, R_1 the radius of curvature, R_2 the radius of the neck, β the half filling angle, and x the particle diameter. With the fluid's surface tension Γ the capillary force F_C is given as [27]:

$$F_C = \Gamma\,\pi\,x\,sin\beta\,\underbrace{\left[\sin(\beta+\theta)\right]}_{I} + \underbrace{\frac{x}{4}\left(\frac{1}{R_1}-\frac{1}{R_2}\right)sin\beta}_{II} \qquad (1)$$

It is easy to see that the emerging capillary force consists in general of two parts: the axial component of the surface tension acting at the liquid/gas interface (I) and the Laplace pressure acting inside the fluid bridge (II).

A more simplified equation for the capillary force between two spherical particles with identical diameter is [28]:

$$F_C = \pi x \Gamma cos\theta \quad (2)$$

Boundary condition for this equation is a separation distance of s = 0 and a small bridge volume compared to the particle size. This simplified equation is often used in the context of capillary suspensions [11,28,29], to illustrate the main factors that can be influenced during paste formulation.

The influence of the capillary force in capillary suspensions increases with increasing solids content and decreases with increasing particle size, analogous to van der Waals forces [27,30]. The following estimations for the regarded interparticular forces show the unique potential of capillary suspensions: While the omnipresent vdW force significantly contributes only within a range about 10 nm, the capillary force can act up to 10 µm. Typical values of capillary forces in suspensions are about 10^{-7} N, while the vdW force reaches roughly 10^{-9} N for a particle size of 1 µm. Since the emerging capillary forces are generally much stronger than the vdW forces, the latter can be neglected in capillary suspensions [11].

The rheological behavior of capillary suspensions has been investigated empirically in detail [16,28,29,31]. Furthermore, important correlations between yield stress and material properties have been explained theoretically. The following equation describes the yield stress σ_y of a capillary suspension consisting of equally sized particles in direct contact (s = 0) [26,32–34]:

$$\sigma_y = f\left(\phi_{solid}, N_{bridge}\right) g\left(V_{bridge}\right) \frac{4\pi\Gamma cos\theta}{x} \quad (3)$$

with $f(\phi_{solid}, N_{bridge})$ being a function of the solids content and the number of capillary bridges and $g(V_{bridge})$ a function of the bridge volume. Evidently, N_{bridge} and V_{bridge} are related to the secondary fluid content in the suspension. Both functions are not yet described completely and some approaches are inconsistent. For instance, it is known that σ_y scales with ϕ_{solid} in a power law $\sigma_y \sim \phi_{solid}^{\nu}$, but the exponent ν varies in the literature between 2 [35] and 3.3 [31]. However, in homogeneous capillary suspensions the yield stress increases with increasing secondary liquid and solid content, since the bridge volume as well as the number of particle-particle contacts and capillary bridges increases [10,28,29].

Equation (3) shows that σ_y scales with the reciprocal particle diameter x^{-1} which was demonstrated empirically by Koos et al. [29] for capillary suspensions in the pendular state. Furthermore, yield stress is a function of interfacial tension Γ and the contact angle θ in the three phase system. These parameters have a direct impact on the capillary force F_c, cf. equation (2). Studies applying wetting agents in capillary suspensions showed a strong dependency of surfactant concentration on the yield stress, since Γ is sensitive on small

amounts of surfactants [29] and also θ may change if the surfactant molecules adsorb on the solid. Further investigations regarding influence of θ on rheology and microstructure of capillary suspensions were performed by Bossler et al. [26], but this will not be elucidated in more detail, here.

II. Capillary suspensions as precursors for porous materials

Recently, Dittmann et al. [10,16] developed a versatile processing route for manufacturing highly porous and mechanically stable sintered parts with porosities higher than 50% at pore sizes < 10 µm. This method uses capillary suspensions of ceramic particles as precursors for ceramic materials. Ceramic capillary suspensions show a well controllable formation of a strong capillary network that can be used as precursor for highly porous sintering materials. The homogeneous sample spanning network can be preserved during debinding and even in the sintered part. Completely open-porous sintered structures are accessible [10].

The main process steps for manufacturing such porous ceramics are summarized in Fig. 6. The capillary network formation is induced by adding the secondary phase to a ceramic suspension with low particle concentration (ϕ_{solid} = 10 – 25 vol%). After homogenizing the suspension (e.g. with a ball mill) green bodies can be formed (e.g. by casting, extrusion). Most of the bulk phase can be removed from the green bodies via an adsorbing bedding layer or solvent extraction. Using a binder dissolved in the secondary phase (e.g. sucrose), which solidifies in the capillary bridges as the secondary phase is removed by evaporation, helps to create stable green parts. The porous particle network is stabilized and settling is prohibited. Without a secondary liquid the particle network would at least partially collapse. After bulk debinding, the green parts are thermally treated to remove all organic components and finally sintered.

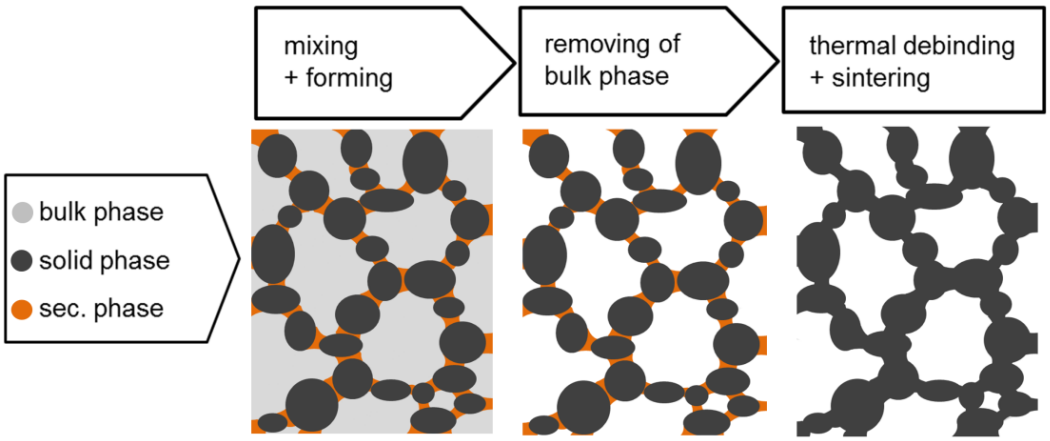

Fig. 6: Flow sheet with the main process steps for highly porous sintering materials based on capillary suspensions [40]. *Reproduced with permission from Elsevier. © Elsevier.*

Until now, ceramic capillary suspensions based on paraffin oil as bulk fluid, Al_2O_3 as solid phase and an aqueous sucrose solution (1.9M) as secondary phase were examined [10,16]. In addition to at room temperature liquid phases (e.g. alcohols, H_2O, oils) also molten liquids (waxes, nonpolar and polar polymers) can be used as bulk or secondary phases if the suspensions are processed at appropriately elevated temperature. SEM crosscut images of sintered bodies of suspensions with and without secondary liquid show the structural change due to the formation of the capillary network, see Fig. 7. The average pore diameter $x_{50,3}$ was determined via image analysis (Linear Intercept Count Method [36]) and increases from 11.5 ± 1.1 µm to 24.5 ± 0.3 µm. Simultaneously, the porosity increases here from 40% up to 56% (determined by Archimedes density, DIN EN 993-1).

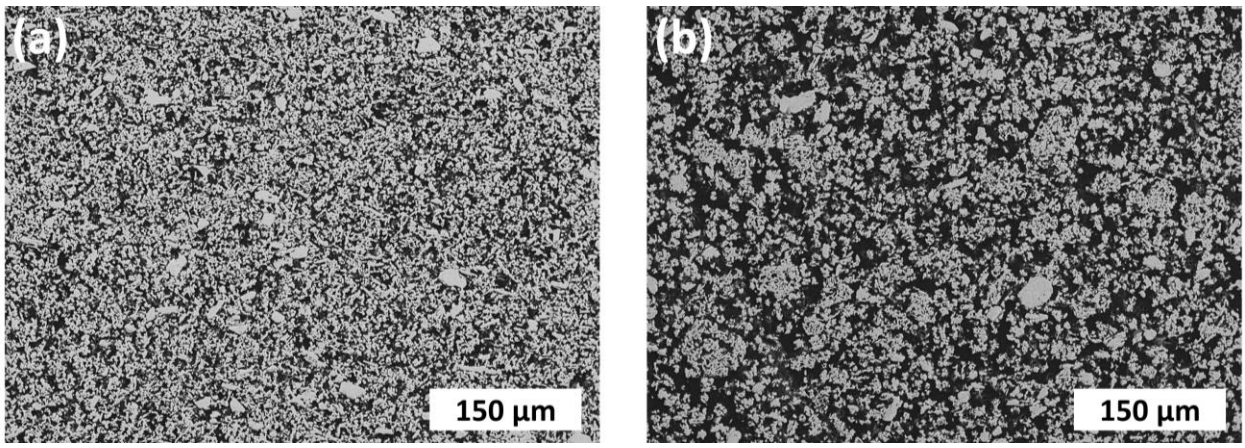

Fig. 7: SEM crosscut images of sintered capillary suspensions (α-Al_2O_3, $x_{particle}$ = 5.8 µm). (a) ϕ_{solid} = 20 vol%, no secondary liquid phase and (b) ϕ_{solid} = 20 vol%, 4 vol% secondary liquid phase. Solid Al_2O_3 particles appear light grey and pores are black in these images.

Investigating capillary suspensions with a broad range of added secondary liquid fraction Dittmann et al. [16] suggested a characteristic three-regime-model describing the changes in the network structure. Fig. 8 shows three characteristic regimes indicated by a yield stress change depending on the secondary phase content and SEM images of sintered capillary suspensions. Homogeneous capillary suspensions with a strong particle network are only available in a specific range of secondary liquid content (*regime II*). *Regime I* marks the transition from a weak particle network controlled by van der Waals forces to the fully developed paste-like capillary suspensions (*regime II*). *Regime III* is characterized by increasing inhomogeneities. Large spherical agglomerates dominate the suspension structure, but the attraction between these aggregates is weak and results in a low yield stress.

Rheological behavior (i.e. yield stress) of the suspensions but also porosity and pore size of the sintered parts can be adjusted by varying particle size $x_{50,3}$, solids content ϕ_{solid}, and secondary

phase content ϕ_{sec}. Yield stress increases with increasing solids content and decreasing particle size. Porosity decreases with increasing solids content and pore size decreases with decreasing particle size at constant sintering conditions. Yield stress, porosity and pore size increase with increasing secondary liquid content as long as the capillary suspension is in *regime II*. Sintered parts from *regime III* typically exhibit a broad particle size distribution but no further increase in porosity is observed [10,16].

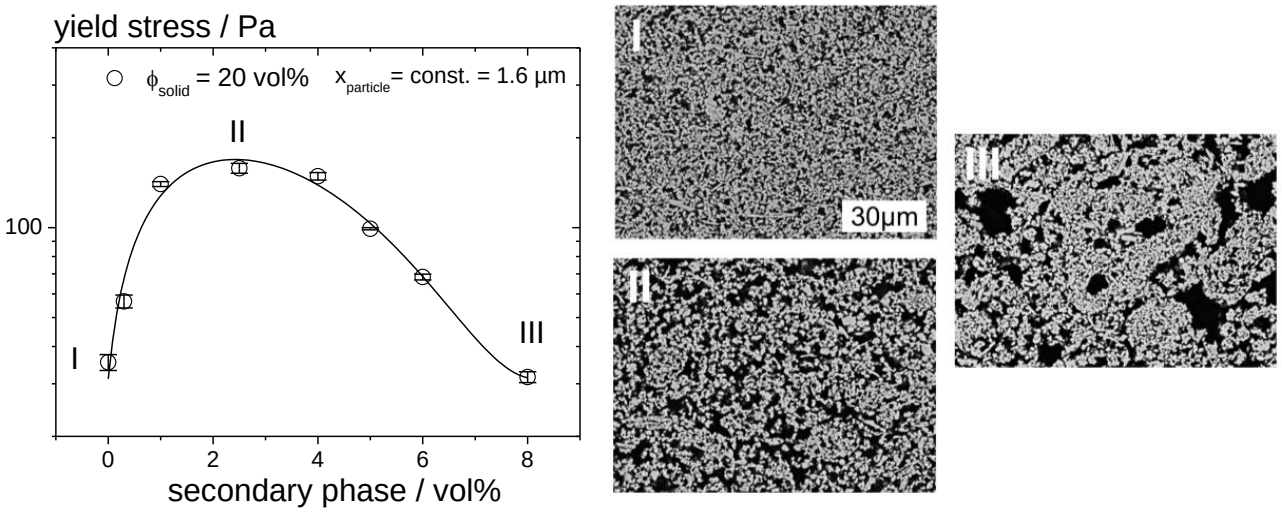

Fig. 8: Three-regime-model of capillary suspensions illustrated via the yield stress (left) and appropriate SEM crosscut images of sintered capillary suspensions (right). Solid particles appear light gray and pores as black. Solid: α-Al_2O_3, $x_{particle}$ = 1.6 µm. Bulk phase: paraffin-oil. Secondary phase: aqueous sucrose-solution (1.9 M) [16].

Sintered parts made from capillary suspensions can easily reach average pore diameters between 1 – 50 µm at porosities > 50%. As it is shown, using capillary suspensions as precursors for sintered materials is versatile and cost-efficient since it is based on standard unit operations. This process gives access to a broad range of pore structures, including previously hardly accessible porosity and pore size ranges (ε > 50% at x_{pore} < 10 µm) or a controlled, well-defined broad pore size distribution [10,16].

III. Mechanical strength of sintered capillary suspensions

Mechanical strength is a key parameter for dense as well as porous ceramic materials. In most technical structural ceramics it is required to eliminate all pores, since they act as defects and lower reliability and mechanical strength of the components [17]. This is opposite if the application requires certain functionality, like a high inner surface or a low specific density, which can only be realized by a porous structure. In porous ceramics pore shape, pore size and in particular the porosity determine the mechanical strength of the specimens. It is a general

characteristic of porous ceramics that mechanical strength decreases with increasing porosity. In the recent publications this correlation was also shown for porous ceramic parts based on capillary suspensions [16].

Flexural strength, compressive strength and Young's modulus strongly correlate with the porosity ε of the sintered parts. Dittmann et al. [16] showed that the mechanical strength of sintered capillary suspensions is not affected by the average pore size but only porosity of the sintered part. Considered porous parts were in a pore size range of 5 – 25 µm, at porosities between 52 – 60 %.

Fig. 9 shows the relative compressive strength of sintered capillary suspensions in comparison with porous ceramics from other manufacturing processes as a function of the relative density 1-ε. The relative compressive strength is defined as the compressive strength of the porous part, divided by the flexural strength of the dense matrix material (for Al_2O_3, $\sigma_{f,0}$ = 400 MPa). The capillary suspension data is in the same range as those of porous ceramics from other processes. All materials to which the data in Fig. 9 refer and especially the sintered porous ceramics from *regime I* and *II* capillary suspensions share the property of the very sharp-edged pore structure that is presumably responsible for the brittle fracture. As expected the ceramic capillary suspensions of regime III clearly show lower mechanical strength due to their strong heterogeneity.

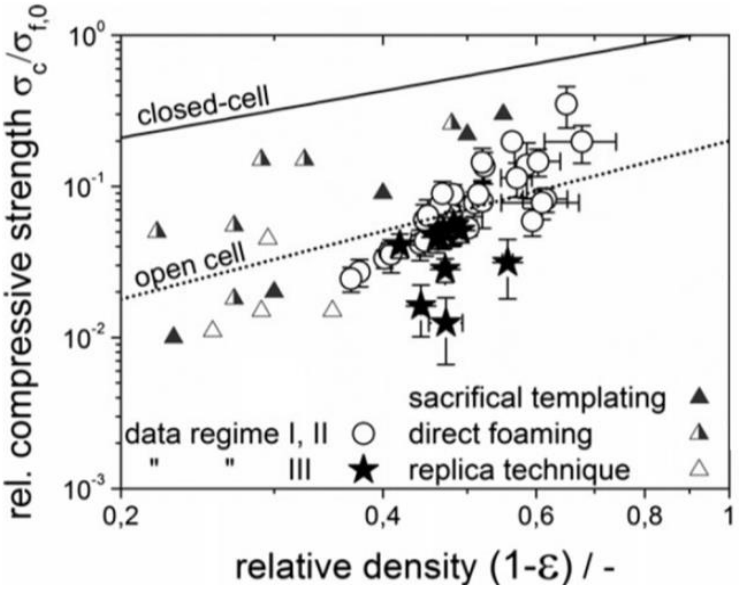

Fig. 9: Relative compressive strength as a function of the relative density of porous sintered parts of various manufacturing methods. The model of Gibson & Ashby [19] shows good agreement with the ceramic capillary suspension data of regime I and II. $\sigma_{f,0}$ = 400 MPa for Al_2O_3 [16]. *Reproduced with permission from J. Dittmann, N. Willenbacher, J. Am. Ceram. Soc. 97 (2014) 3787–3792. © 2014 The American Ceramic Society.*

The mechanical strength and its variation with ε is well described by the Gibson & Ashby model [22]. This model describes the fracture strength of porous materials [19] considering two possible cases for brittle cellular materials with a cubic cell structure: porous media with an open-cellular structure and porous media with a closed-cellular structure. Since sintered parts from capillary suspensions always result in an almost completely open porous structure, the open-cell model will be discussed in more detail. This model relates the compressive strength of the porous material σ_c normalized to the flexural strength of the dense material $\sigma_{f,0}$ to the open porosity ε:

$$\frac{\sigma_c}{\sigma_{f,0}} = B_o\,(1-\varepsilon)^z \qquad (4)$$

B_0 is an empirical prefactor, z is a factor depending on the mode of failure. The exponent z is 3/2 for the brittle fracturing materials discussed here. The mechanical strength of a large variety of brittle cellular materials is described by Eq. (4) using B_0 = 0.2 [19]. This model is based on the high notch effect which appears at the very sharp cell edges of the described materials under load. This effect is responsible for the fracture of the solid part under load.

1.2 Motivation and manuscript overview

The previous chapters introduced an innovative concept for using capillary suspensions as precursors for highly porous sintering materials that gives access to previously hardly accessible porosity and pore size ranges. For a tailored product development the complete understanding of capillary network formation and its influence on rheological behavior is of importance. This includes knowledge how paste composition affects rheology and product properties (e.g. microstructure, strength) of the sintered materials. Previous work focused on the empirical and theoretical investigation of numerous influencing factors, including wetting properties of the solid, interfacial tension of the liquids, solids content, secondary phase content, particle size, additives (wetting agents [29], thickeners [37]), and mixing conditions [38]. These studies focused on ideal model systems [26,31] as well as compositions for several product formulations [10,13,35]. However, there are still open questions regarding network structure in the wet state of capillary suspensions. How the shape of the dispersed particles affects rheology and microstructure of capillary suspensions still remains elusive. Previous studies focused on spherical or approximately isometric particles and shape effect was ignored. Understanding its impact on microstructure and rheology facilitates product formulation of capillary suspensions that are made of irregular shaped, flake-like or elongated particles. Being aware of the influence of all these parameters on rheology and microstructure of capillary suspensions will facilitate to create products with good handling properties and also sintered products with a tailored microstructure (i.a. porosity, pore size, pore roughness, homogeneity).

Mechanical properties of porous ceramics are strongly dependent on their microstructure, since brittle failure results from emerging cracks at the notches of the porous structure (cf. chapter 1.1.3). The mechanical strength of ceramics based on capillary suspensions is well comparable to that of ceramics from other processes. So far, there are no publications about strategies that allow for increasing mechanical strength of sintered capillary suspensions. This is a challenging task, since strength results from number and strength of particle-particle bondings, what means in most cases increasing the density, viz. reducing porosity, of the material.

In previous work [10,16] capillary suspension based ceramics were manufactured as slip-cast samples with rectangular shape. This is feasible for developing and testing a new material, but not for using the material in a real application. Up to now, there is no literature about tailored processes or formulations of capillary suspensions that are suitable for other molding processes, like thin film coatings or 3D printing. However, the rheology of capillary suspensions with their high yield stress and their strong shear thinning behavior makes them a promising material system for these processes. Asymmetric filtration membranes or hierarchical lightweight

construction materials may be interesting products, realized by capillary suspension based coatings or 3D printing inks.

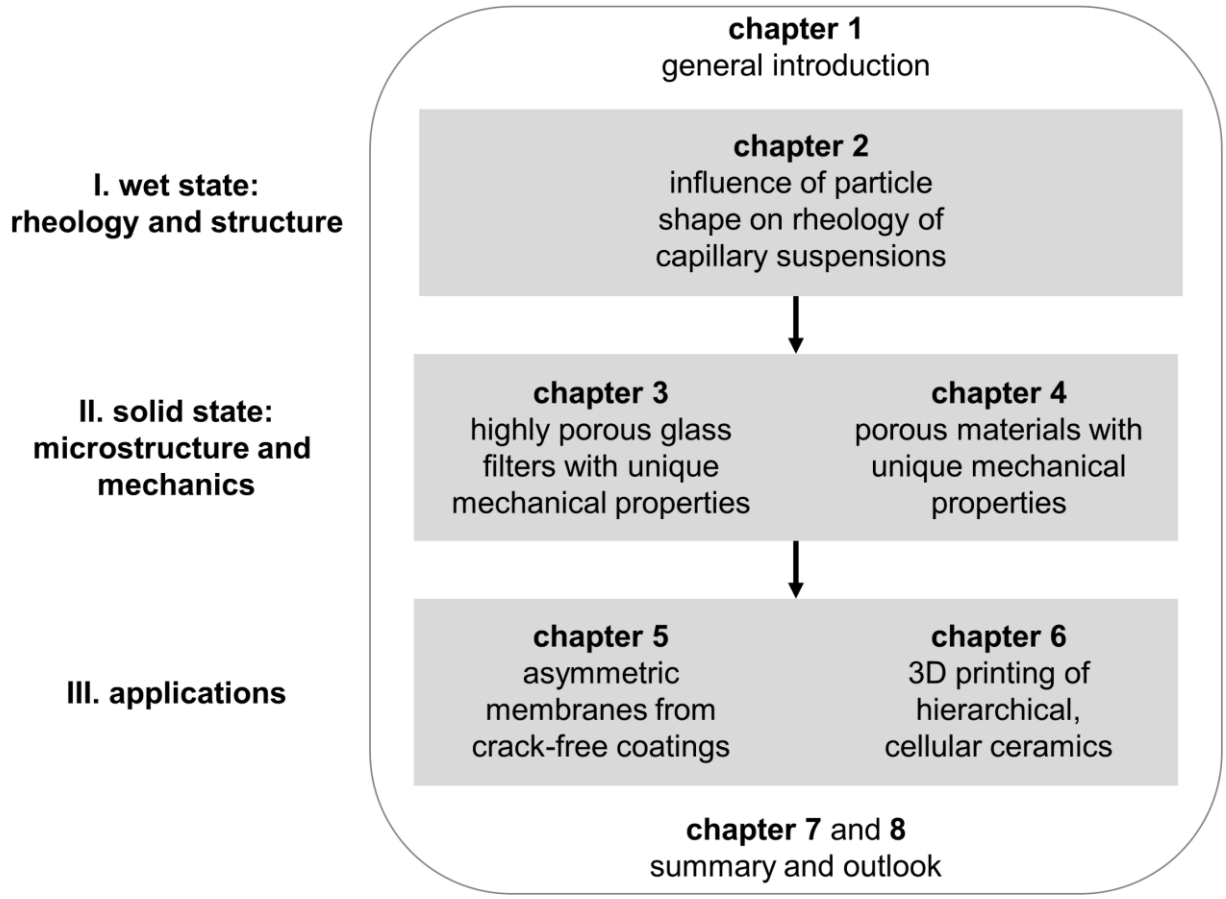

Fig. 10: Schematic overview of this dissertation. The thesis is divided into three thematic sections: I. wet state: rheology and structure, II. solid state: microstructure and mechanics, and III. applications.

This thesis presents an experimental study on the tailored formulation of capillary suspensions as precursors for sintered materials. Various ways for tailoring the processing properties (wet state), the microstructure (wet and solid state) and the mechanical strength (solid state) are demonstrated. The following main part of this thesis consists of five publications which may be divided into three sections:

I. wet state: rheology and structure,

II. solid state: microstructure and mechanics, and

III. applications.

Section I includes one peer-reviewed publication, while section II and III include two publications, each. Fig. 10 outlines the structure of this dissertation in a schematic. The publication in **section I** discusses the influence of particle shape on the rheology and microstructure of capillary

suspensions [39]. **Section II** includes one publication about sintered capillary suspensions based on glass particles that show a smooth microstructure with high mechanical strength and excellent filtration properties [40], and a second article about capillary suspension based materials in which the secondary liquid works as carrier for active ingredients [41]. The active ingredients enable point-welding in porous membranes, improve sintering or decrease pore roughness; especially the latter two properties are inspired by the sintered glasses with their particular smooth pore structure, which results in good mechanical properties. In **section III** the developed concepts for sintering materials are used to design products that benefit from the distinct rheological and structural behavior of capillary suspensions in wet and solid-state, respectively. In the first publication capillary suspensions are used for thin, porous coatings, e.g. for manufacturing asymmetric filtration membranes [42]. The second publication introduces an innovative concept for 3D printing complex, cellular ceramics with high specific strength and exclusively open-porous struts [43].

The experimental results of this thesis begin with section I about rheological and microstructural investigations of capillary suspensions. Therein, **chapter 2** discusses how the addition of a second immiscible fluid affects microstructure and rheology of suspensions including anisotropic particles. We investigated differently shaped calcium carbonate, graphite and aluminum particles. Yield stress and oscillatory shear measurements illustrate which particles tend to form stable capillary suspensions while others do not. Optical as well as electron microscopy confirm the observations from rheological measurements. For particles with a shape that allows for the formation of a stable particle network, the investigations show strong differences in the amount of secondary fluid that can be accommodated in the capillary bridges.

Following chapters focus on the microstructure and properties of solid parts based on capillary suspensions. In **chapter 3** we introduce a novel processing route for manufacturing sintered glass filters with a remarkable smooth and round pore structure based on capillary suspensions. These filters exhibit porosities ≥ 50 %, a narrow pore size distribution and average pore sizes between 1 – 50 µm. Sintered filters were characterized regarding compressive strength as well as gas and liquid permeability. Benchmark tests compared the new products with commercial filters. Common models for compressive strength (Gibson & Ashby model for brittle, open-porous materials [19]) and permeability (Darcy's law [44,45]) were used to scale the data.

In **chapter 4** we introduce the *smart capillary suspension* concept for manufacturing macroporous solids from various materials with outstanding microstructure and mechanical strength. This includes sintered materials, like ceramics and polyethylene (UHMWPE), but also carbon, where a high-temperature treatment is not feasible. Findings of chapter 3, that sintered

materials with a smooth pore structure exhibit a high mechanical strength, are applied to manufacture high-strength porous ceramics. With the new manufacturing concept we tailor neck and pore shape of the sintered parts by a controlled deposition of small, sinter-active particles at the particle contact points. Mechanical strength of the sintered parts is increased significantly.

Chapter 5 presents an innovative, universal approach to suppress crack formation in thin coatings from various different materials. Using coatings based on capillary suspensions we are able to suppress cracks during drying of films that are much thicker than the critical cracking thickness of corresponding pure suspensions. The strong capillary network preserves the particle cohesion and depending on the choice of the secondary fluid it also decreases the drying rate. Films of capillary suspensions based on ceramic (Al_2O_3, TiO_2, ZnO) and metallic (Ni) particles are prepared, dried and characterized via microscopy. Furthermore, metal films are examined with respect to electric conductivity; after coating on a porous substrate Al_2O_3-films are sintered and tested on permeability and filtration cut-off.

In **chapter 6** we use a filamentary based direct ink writing (DIW) technique for manufacturing hierarchically structured, open porous ceramics that are excellent candidates for lightweight construction applications. We develop capillary suspension based inks with ceramic particles that show appropriate rheology for DIW. With an innovative drying, debinding and sintering strategy we manufacture crack-free and undeformed honeycomb structures with porosities up to 88% and high specific strength. The cellular samples exhibit fully open-porous struts with porosities between 45-60 % and pore sizes $x_{50,3} < 6$ µm. Strength of the lattice structures excels that of slip-cast specimens based on capillary suspensions and is well predicted by established scaling laws for hexagonal honeycomb structures.

2 Influence of particle shape on the rheology of capillary suspensions

Full title: Influence of particle shape on the rheological behavior of three-phase non-Brownian suspensions

Authors: Johannes Maurath, Boris Bitsch, Yvonne Schwegler, Norbert Willenbacher

Status: published

Bibliographic data: Colloids and Surfaces A: Physicochem. Eng. Aspects 497 (2016) 316–326 10.1016/j.colsurfa.2016.03.006

Abstract

Capillary suspensions are three-phase fluids comprising a solid and two immiscible, liquid phases with unique texture and flow properties. So far, research focused on isometric particles, here we discuss how the addition of a second, immiscible fluid affects structure and flow of suspensions including anisotropic particles. Differently shaped calcium carbonate as well as graphite and aluminum particles have been investigated.

For needle-shaped and scalenohedral particles no increase in yield stress σ_y or storage modulus G' characteristic for a strong capillary force controlled, percolating particle network is observed when a secondary fluid is added. In contrast, a pronounced increase in σ_y and G' is found when a secondary fluid is introduced to suspensions of plate-like particles and optical as well as electron microscopy confirm the formation of a sample-spanning network characteristic for capillary suspensions.

Suspensions of isometric particles exhibit a distinct maximum in σ_y or G' at low fractions of secondary fluid to particle volume fraction $\phi_{sec} / \phi_{solid} \approx 0.1 – 0.2$, whereas suspensions of plate-like particles exhibit constant σ_y and G' values over a wide range of $\phi_{sec} / \phi_{solid}$ values up to ≈ 1 until spherical agglomeration occurs. Due to the different shape of the capillary bridges suspensions of plate-like particles can accommodate much larger fractions of secondary fluid

until spherical agglomeration sets in than systems including spherical particles thus offering a versatile basic concept for the design of complex multi-component paste-like products.

2.1 Introduction

Capillary suspensions are three-phase fluids including a solid and two immiscible liquid phases. Addition of a small fraction (typically < 5vol%) of a secondary liquid phase to a suspension of particles dispersed in the so-called primary or bulk phase leads to the formation of a strong, sample spanning particle network, even at low particle loadings. The particle network gains its strength from the capillary forces inferred from the added secondary liquid no matter whether it wets the particles better or worse than the primary liquid. Generally, non-Brownian particles are employed (particle size varies between 0.5 and 50 µm) and particle loadings range between 5vol% and 40vol% [11,35,46–48].

Two types of capillary suspensions are distinguished depending on the three-phase wetting angle θ_{SB} the secondary liquid (S) forms against the solid surface in the bulk phase environment (B). In the pendular state ($\theta_{SB} < 90°$), the secondary liquid wets the solid phase better than the bulk fluid and forms pendular bridges between the particles. In the case where $\theta_{SB} > 90°$, termed the capillary state, the particles form clusters around small volumes of the second fluid [48]. Both scenarios finally result in a percolating particle network.

The capillary force F_c between two particles connected by a pendular bridge is composed of two parts: the Laplace pressure inside the bridge and the interfacial tension acting at the solid-liquid-liquid contact line. F_c depends on the diameter x of the particles, their separation distance s, the surface tension of the liquid Γ, as well as the volume V and shape of the liquid bridge. Analytical as well as computational solutions for F_c assume a certain bridge shape (e.g. toroidal, cylindrical, etc.) or solve the Laplace-Young equation directly [[35] and references therein]. For a finite particle separation of equally sized spheres connected by a fluid bridge, the capillary force is given by

$$F_C = \frac{x\,\pi\,\Gamma\,cos\,\theta_{SB}}{1 + 1.05\hat{s} + 2.5\hat{s}^2} \quad with \quad \hat{s} = s\sqrt{\frac{x}{2\,V}} \tag{5}$$

which simplifies to the well-known expression $F_c = x\pi\Gamma\cos\theta_{SB}$ for spheres that are in contact [49]. The equation for the capillary force may be modified to account for spheres of different sizes [32], rough spheres [50], and changes to bridge volume [33,51]. The typical range for the ubiquitous van der Waals force is on the order of a few nanometers and depletion forces in colloidal systems typically act on the order of 100 nm. In contrast, the capillary force acts on a

much longer length scale of typically 10–100 µm and its absolute value is generally orders of magnitude larger than that of the vdW force. The yield stress σ_y of a pendular state suspension similar as for wet granular matter is related to the capillary force [29,52]

$$\sigma_y = f(\phi) g(V,s) \frac{\Gamma \cos\theta}{x} \quad (6)$$

where f(ϕ) is a function of the particle volume fraction and depends on the number of contacts per particle. The volume of the bridge V and the distance between the two particles s are included in the function g(V,s).

For the capillary state, calculations and experiments have shown that clusters of different shape and structure are formed within the suspension strongly depending on the amount of secondary liquid and its wetting behavior. With higher amounts of secondary liquid, particles tend to form octahedral clusters that have a stronger cohesion than tetrahedral clusters which are more favored for lower secondary liquid contents [29,41,48].

In both, the capillary and the pendular state, capillary suspensions exhibit a unique paste-like texture. They exhibit an apparent yield stress σ_y, gel-like elastic behavior with a high, frequency independent storage modulus G' much larger than the loss modulus G'', and a strongly shear thinning flow behavior which renders this class of materials a promising generic formulation platform for a broad variety of applications. Capillary suspensions are highly resistant to sedimentation, and flow properties can be tuned in a wide range to meet different processing or application demands. Even the flow behavior of methane hydrates turned out to be strongly affected by capillary bridging [53]. A broad range of innovative products including novel food formulations, such as heat stable and low calorie chocolate spreads [12,13], capillary suspension based foams [54,55] or pastes for printed electronics, e.g. lithium-ion battery electrodes or front side metallization of solar cells with unique shape accuracy and surface uniformity have been developed [15]. The capillary suspension concept has also been used to control structure formation in particle-laden polymer blends [56] and to assemble metals and nanoparticles into novel nanocomposite superstructures [57]. Beyond that capillary suspensions can be utilized as precursors for highly porous sintering materials to be used as light weight construction materials, filters or membranes [10,16,40,41].

So far, investigations have been restricted to suspensions including spherical, close-to-spherical or isometric particles. However, understanding capillary phenomena in three-phase suspensions of non-isometric particles is of fundamental academic interest, and beyond that many technically important materials include non-spherical, highly anisotropic particles like fibers or plates. E.g.

they are used as pigments in coatings and inks, as fillers in adhesives and sealants or to provide strength to polymeric materials. Also the flow behavior of suspensions of organic matter, like rigid macromolecules (e.g. xanthan, schizophyllan) viruses or coke particles, is of high interest. Accordingly, the rheology of anisotropic, non-Brownian particle suspensions has been explored for a century including experimental, theoretical, and numerical investigations [58–67]. The intrinsic viscosity of differently shaped particles has been calculated [60–62]. Basically, the viscosity at a given volume fraction is higher the more the particle shape differs from a sphere [63], e.g. the higher the aspect ratio r for fibers [64], and prolate, fiber- or needle-like particles yield a higher viscosity than plate- or disk-shaped, oblate particles [63,68]. For concentrated suspensions structural order, particle interactions and number of particle contacts as well as particle orientation and flow-alignment have to be considered and empirical models for the limiting low and high shear viscosity as a function of particle volume fraction have been suggested [63,67]. However, it should be kept in mind the maximum packing fraction for anisotropic particles is higher than for spheres [69]. Complex phase behavior including liquid crystalline structures and arrested states may occur at particle loadings well below maximum packing resulting in complex flow behavior [70,71].

Here we focus on the question how the addition of small amounts of secondary immiscible fluids affects the flow behavior of non-Brownian suspensions including anisotropic particles. We have investigated whether capillary suspensions similar as for spherical particles can be formed, and how their characteristic flow behavior depends on particle shape and secondary fluid content. Precipitated calcium carbonate (PCC) particles with different shape (spherical, scalenohedral, needle-shaped, plate-shaped) have been employed as model systems. Yield stress and storage modulus have been measured since these quantities are very sensitive to structural changes. Confocal laser scanning microscopy (CLSM) and scanning electron microscopy (SEM) have been utilized to visualize the suspension microstructure in the wet and in the solid state. In addition, two material systems potentially relevant for printed electronic applications or energy storage and conversion systems have been investigated, namely aluminum flake suspensions with different diameter to width ratio and graphite suspensions based on particles with spherical and oblate shape. For such applications conductivity in the final dry film is a key feature and is supposed to be higher using oblate instead of spherical particles [72,73]. The capillary suspension based formulation concept is of special relevance in this field since it allows for a demand-oriented adjustment of flow behavior and sedimentation stability without conventionally used organic additives (e.g. surfactants or thickeners) generally deteriorating electronic properties of the final dry film.

2.2 Experimental

Experiments were carried out using three different material systems: a set of four PCC samples with varying length over diameter ratio, i.e. aspect ratio r varying between 0.1 (plate-like) and 7.9 (needle-shaped), a pair of spherical and plate-like or flaky graphite samples, and two plate-shaped species of aluminum flakes with different aspect ratio. All these systems were characterized rheologically, additional structural investigations were performed on the PCC-based suspensions using confocal laser scanning microscopy (CLSM) and scanning electron microscopy (SEM).

2.2.1 Raw Materials

Commercial grade precipitated calcium carbonate particles (PCC) were obtained from SCHAEFFER KALK GmbH & Co. KG (Diez, Germany). Four samples with different aspect ratio but also different crystal or amorphous structure were investigated, characteristic parameters are summarized in Table 1. Scanning electron microscopy (S-4500; Hitachi High-Technologies Europe GmbH, Krefeld, Germany) was used to determine the particle aspect ratio r via image analysis of at least 20 particles (Fig. 11). Fraunhofer diffraction (Helos H0309; Sympatec GmbH, Clausthal-Zellerfeld, Germany) was used to determine the equivalent sphere diameter distribution. A wet dispersing unit (Quixel; Sympatec GmbH) was used and particles were dispersed in ethanol, corresponding results are shown in Fig. 11. All PCC particles except the needle-shaped species show a similar equivalent sphere diameter distribution and average particle size. The apparent bimodality observed for the needle-shaped particles is a consequence of the large anisotropy [74,75]. Particle aspect ratio and average equivalent particle diameter are sufficient to describe the shape of all used particles, since they can be approximated as rotationally symmetric ellipsoids (oblate and prolate spheroids).

Table 1: Material properties of used PCC powders. Crystal structure, density and specific surface are given by manufacturer.

product	**plate-shaped**	**spherical**	**scalenohedral**	**needle-shaped**
crystal structure	calcite	amorphous	calcite	aragonite
density (g/cm³)	2.7	2.7 – 2.9	2.7	2.9
specific surface S_v (m²/g)	17	8	9	10
aspect ratio r (-)	0.1 ± 0.0	1.0 ± 0.1	2.9 ± 0.8	7.9 ± 3.1
av. particle size $x_{50,3}$ (µm)	1.92 ± 0.0	1.4 ± 0.02	1.7 ± 0.02	2.2 ± 0.03

The bulk phase was paraffin oil (Carl Roth; Karlsruhe, Germany) with Newtonian flow behavior and a dynamic viscosity η(20 °C) = 0.03 Pa s. The nonionic wetting agent Polysorbat 20 (Tween20; Carl Roth) with HLB = 16.7 was used at a concentration of 0.2 vol% based on bulk phase to prevent unwanted agglomeration in the pure suspensions. The secondary liquid phase was pure water.

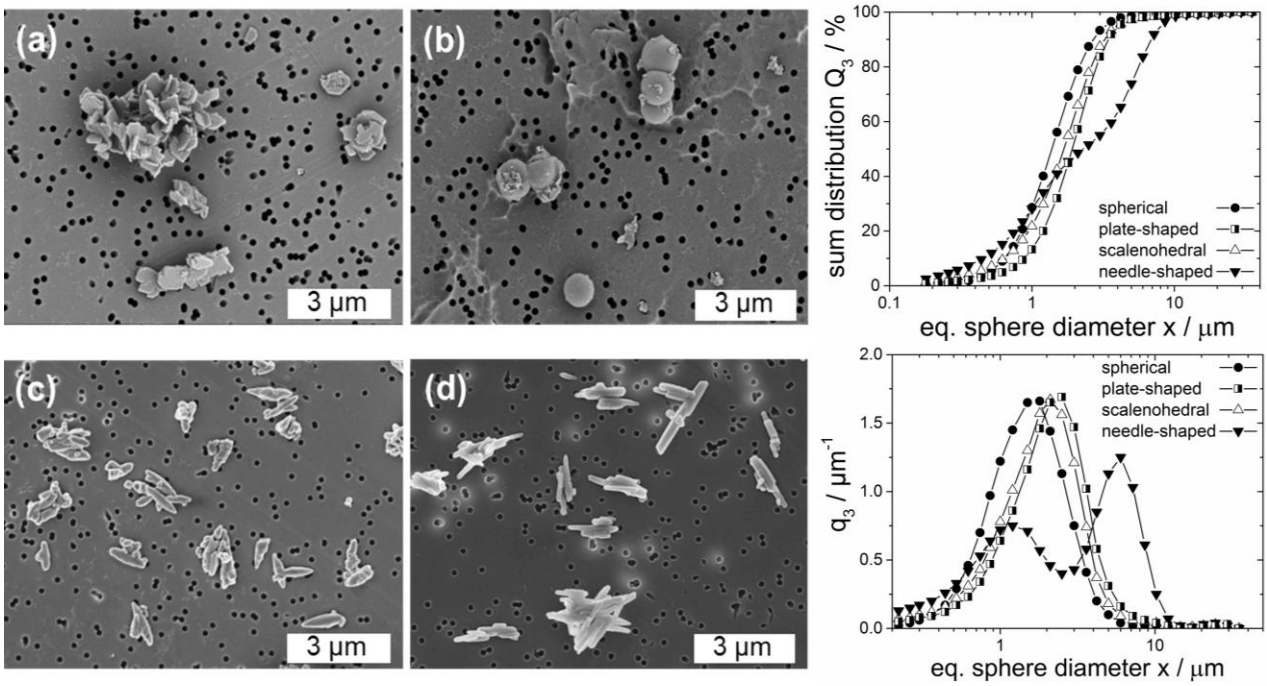

Fig. 11: Left: SEM images of the used PCC powders with different particle shapes: (a) plate-shaped, (b) spherical, (c) scalenohedral, (d) needle-shaped. Black dots in the background of the images result from sample preparation. Right: Particle size analysis of the used PCC powders. Differential particle size distribution q_3 and sum distribution Q_3 were determined through Fraunhofer diffraction. *Reproduced with permission from Elsevier.*

Two different, commercially available graphite powders were used as carbon material: SLP 30 (Imerys Graphite & Carbon; Bironico, Switzerland) contains plate-shaped particles with a density of ρ = 2.27 g/cm³, an average equivalent particle diameter of $x_{50,3}$ = 15.6 ± 0.1 µm determined by Fraunhofer diffraction and a specific surface of 7 m²/g (manufacturer information). SMGPA powder (China Steel Chemical Corporation; Kaohsiung, Taiwan) consists of spherical shaped particles with a density of ρ = 2.21 g/cm³, an average equivalent particle diameter (volume median diameter) of $x_{50,3}$ = 7.7 ± 0.1 µm determined by Fraunhofer diffraction, and a specific surface of 2.2 m²/g (manufacturer information). SEM-images (Fig. 12) of graphite particles were used to determine aspect ratio r via image analysis of at least 20 particles (plate-shaped: r =

0.15 ± 0.04, spherical: r = 1.2 ± 0.1). Glycerol (Carl Roth; η(20 °C) = 1.48 Pa s) was used as bulk phase for this material system. 1-Octanol (purity > 99%; Merck Millipore, Darmstadt, Germany; η(20 °C) = 0.009 Pa s) was utilized as secondary liquid.

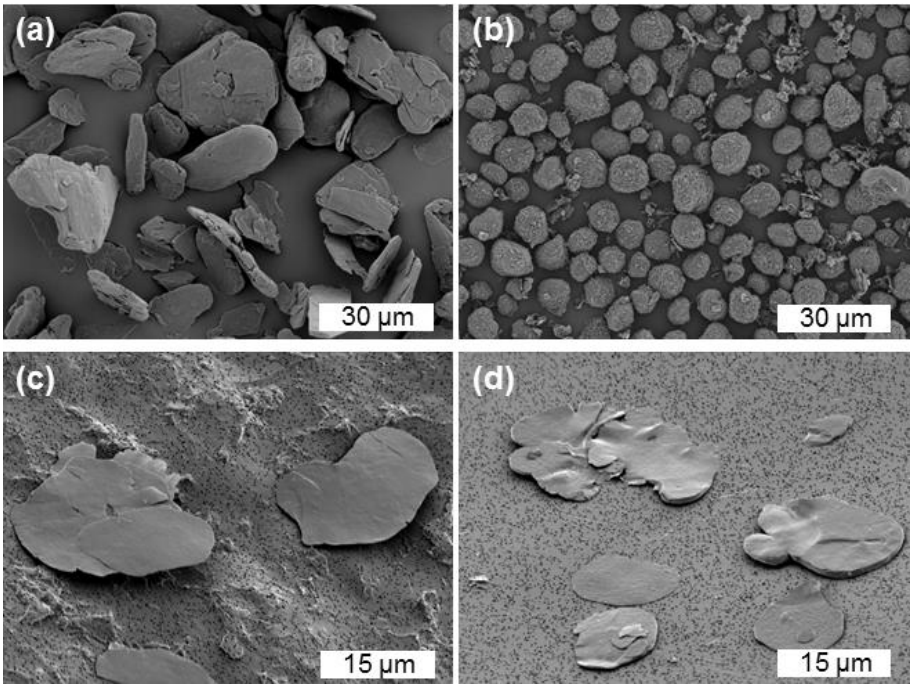

Fig. 12: SEM images of the graphite particles: (a) plate-shaped (aspect ratio r = 0.15 ± 0.04), (b) spherical (aspect ratio r = 1.2 ± 0.1), and of the aluminum particles with varying aspect ratio: (c) pigment 1, r_1 = 0.013, (d) pigment 2, r_2 = 0.020. *Reproduced with permission from Elsevier.*

Aluminum particles (Schlenk Metallic Pigments GmbH; Roth, Germany) with two different aspect ratios (pigment 1: r_1 = 0.013, pigment 2: r_2 = 0.020; manufacturer information) were utilized. The particles exhibit the so-called silver dollar morphology, as shown by SEM micrographs in Fig. 12. Average equivalent particle diameter for both particle types is in the same range with $x_{50,3}$ = 16 - 18 µm (manufacturer information). The particles were delivered dispersed in mineral spirit with a particle volume fraction of 30-35 vol%. The bulk phase for this material system was a mixture of paraffin oil (Carl Roth; η(20 °C) = 0.03 Pa s) and mineral spirit (η(25 °C) ≈ 0.001 Pa s). Since mineral spirit is a mixture of paraffins, cycloparaffins and aromatic hydrocarbons it is completely miscible with paraffin oil. The mixing ratio of paraffin oil to mineral spirit was 1 : 0.3-0.5. The secondary liquid phase was pure water.

2.2.2 Sample Preparation

Suspensions based on PCC particles were prepared by mixing the solid powder into the bulk phase with a high shear dissolver (diameter: 35 mm) at a speed of 1000 rpm for 15 min. Adding a small amount of the nonionic wetting agent Polysorbate 20 (0.2 vol% based on bulk phase) to the suspensions prevents unwanted agglomeration. This concentration guarantees a full coverage of the solid particles by the wetting agent (approximated with an average surface area per adsorbed Polysorbate 20 molecule on $CaCO_3$ of ~6 nm² [76]). The secondary fluid phase was added to the pure suspension using a high shear dissolver at a speed of 1000 rpm for 2 min, followed by a period of 2 min with reduced stirring speed at 500 rpm.

Graphite based suspensions were prepared by mixing the solid powder into glycerol using a high shear dissolver (diameter: 35 mm) at a speed of 1000 rpm for 10 min. Subsequently, secondary fluid was added to the suspension while stirring at 1000 rpm for 2 min. Afterwards the stirring speed was reduced to 500 rpm and mixing was continued for 5 min.

For preparation of the suspensions based on aluminum particles paraffin oil as bulk phase was added to the mineral spirit / particle mixture. The pure suspension was mixed with a high shear dissolver (diameter: 25 mm) at a speed of 1200 rpm for 10 min. Then the secondary fluid phase was added while stirring at a speed of 2000 rpm for 2 min. Afterwards the stirring speed was reduced to 800 rpm for 2 min.

2.2.3 Measurements

For contact angle measurements on $CaCO_3$ we used a rectangular calcite (2 x 2 cm) and a circular aragonite crystal (diameter 1 cm). The three-phase contact angle of the secondary fluid to the $CaCO_3$ was determined via the sessile drop method (OCA 15; Dataphysics) by applying the tangent method. Therefor small water drops were put on the CaCO3 crystals surrounded by paraffin oil. The wetting agent Polysorbate 20 was added to the paraffin oil at a concentration of 0.2 vol%. The $CaCO_3$ crystals were stored in paraffin oil for ~10 minutes to allow for equilibrium adsorption of the wetting agent on the solid surface. Afterwards the secondary fluid drops were put on the $CaCO_3$ crystal; after another 10 minutes waiting time during which the wetting agent could diffuse into the secondary fluid drops the equilibrium contact angle was measured. Contact angles for the aluminum and the graphite system were determined via the same measuring procedure on an aluminum plate and a graphite plate, respectively.

Corresponding data are summarized in Table 2. The crystalline PCC systems and the graphite system exhibit three-phase contact angles below 90° and the corresponding value for the

aluminum system is slightly above 90°. Data for amorphous PCC are not available since a macroscopic amorphous sample for θ_{SB} measurement was lacking.

Table 2: Three-phase contact angle of all investigated material systems.

material system	**θ_{SB} (°)**
calcite, paraffin oil (+ Polysorbate 20), pure water	32 ± 4
aragonite, paraffin oil (+ Polysorbate 20), pure water	79 ± 8
amorphous $CaCO_3$, paraffin oil (+ Polysorbate 20), pure water	-
graphite, glycerol, octanol	78 ± 5
aluminum, paraffin oil, pure water	98 ± 14

Rheological properties of all suspensions were studied using rotational rheometry. Steady and oscillatory shear measurements for the suspensions based on PCC and aluminum particles were performed with the stress-controlled rheometer Haake Mars II (Thermo Scientific, Karlsruhe, Germany). All measurements were done at a temperature of T = 20 ± 0.5 °C. For steady yield stress measurements a vane geometry with an appropriate Searle cylinder (diameter of 20 mm after DIN 53019-1) was used [77]. Yield stress measurements were carried out by increasing shear stress stepwise in a shear stress range from σ = 0.1 – 4000 Pa, the dwell time at each stress level was set to 10 s. Oscillatory shear measurements were carried out using plate-plate geometry (diameter: 35 mm, gap height: 1.5 mm). To prevent wall slip of the suspensions a sandblasted lower steel plate (surface roughness ~1.2 µm) and a sandblasted upper titanium plate were used.

Yield stress measurements of the graphite suspensions were carried out by increasing shear stress stepwise in a shear stress range from σ = 0.08 Pa or 0.3 Pa to 80 Pa or 300 Pa respectively, using a stress-controlled rheometer RheoStress 1 (Thermo Scientific) with a plate/plate geometry (diameter: 35 mm, gap height: 1 mm). Each stress level was held constant for 5 sec, total duration of a measurement run was 750 sec.

Yield stress measurements for suspensions including aluminum flakes were carried out using a stress-controlled rheometer (Haake Mars II) by increasing shear stress stepwise in a shear stress range from σ = 0.1 – 1000 Pa, the dwell time at each stress level was set to 5 s.

For characterizing the microstructure of the PCC suspensions in the wet state a confocal microscope (TCS SP8; Leica Microsystems) with two solid state lasers (wave lengths λ = 488 nm and 552 nm) was used. Therefor the secondary liquid phase in the capillary suspensions was colored with a fluorescence dye (PromoFluor-488 Premium; PromoKine, Heidelberg, Germany), excitable at a laser wave length of 488 nm. The slight transparency of the

suspensions allowed for taking images of the laser beam reflections in a sample depth of approximately 10 µm, due to using the reflection mode all interfaces in the sample were visible.
The microstructure of selected PCC suspensions was also characterized in the solid state. For this purpose suspensions were cast in spherical molds (diameter 30 mm, height = 2 mm) dried and afterwards slightly sintered at a temperature of 500 °C for 1 h, and SEM micrographs (ESEM-mode at p = 70 Pa, Quanta 650 FEG; FEI, Hillsboro, USA) of fracture surfaces were taken.

2.3 Results and Discussion

2.3.1 Determination of Yield Stress

A prominent characteristic feature of capillary suspensions is their high yield stress due to a strong sample-spanning particle network generated by capillary forces. Yield stress values for all three-phase suspensions consisting of PCC particles, paraffin oil and varying amounts of water as secondary liquid phase, were determined from steady and oscillatory shear experiments.

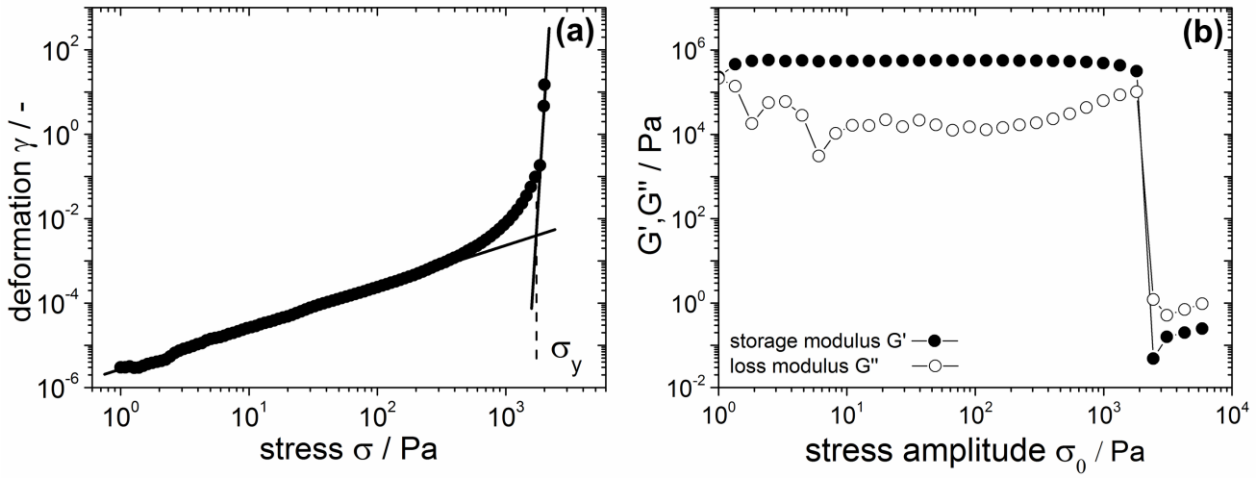

Fig. 13: Determination of yield stress of a three-phase suspension of plate-like PCC particles (ϕ_{solid} = 10 vol%, bulk fluid = paraffin oil, secondary fluid = pure water, ϕ_{solid} = 4 vol%). (a) Deformation vs. applied shear stress in stress ramp experiments performed using a vane geometry (σ = 0.1 – 4000 Pa, t_{dwell} = 10 s, vane dimensions: 22 x 10 mm). The yield stress is determined as the critical stress at the intersection of the tangents to the two branches of the curve. (b) Storage modulus G' and loss modulus G'' as a function of applied stress amplitude in oscillatory shear experiments (ω = 1 s^{-1}). Two critical stresses are obtained: the stress $\sigma_{0,y}$ at which G' drops for more than one decade compared to the average value in the LVE regime and the stress $\sigma_{0,c}$ at which G' = G''. *Reproduced with permission from Elsevier.*

In steady shear stress was increased stepwise and the transition from solid to liquid-like behavior, i.e. the yield stress σ_y, was determined using the tangent method [78]. Typical deformation vs. stress data are shown in Fig. 13a, yield stress data provided below are average values and standard deviations were calculated from at least three measurements.

Oscillatory shear amplitude sweep measurements at constant frequency ω provide two characteristic stress values also related to the transition from solid to fluid-like behavior. Typical G' and G'' vs. shear stress amplitude data are shown in Fig. 13b. G' is much larger than G'' and an extended linear viscoelastic regime (LVE) is observed. A drop of G' for more than one decade compared to the LVE regime is defined as the criterion to determine the onset of nonlinear response and the last data point before this drop occurs may also be treated as a yield value $\sigma_{0,y}$. The third yield value considered here, is $\sigma_{0,c}$ at the crossover of G' and G'' (G' = G'').

As will be shown below all three methods represent reliable and robust methods for determining yield stress of the three-phase suspensions investigated here without deviating much from each other.

2.3.2 Rheology of Two-phase Suspensions

Yield stress σ_y was determined for suspensions consisting of PCC particles with four different particle shapes (spherical, scalenohedral, needle-shaped, plate-shaped), dispersed in paraffin oil at two different solids concentrations ϕ_{solid} = 7 vol% and 10 vol%; no secondary liquid phase was added. Yield stress values σ_y as determined via steady shear rheometry are shown in Fig. 14 as a function of the specific surface of the PCC particles, given in Table 1. The high yield stress values found for these dilute suspensions indicate strong vdW attraction and corresponding formation of a sample spanning network.

The suspensions yield stress strongly varies with increasing specific surface S_V. Especially at S_v < 10 m²/g, small increases of S_v result in a strong increase in yield stress. However, it has to be considered that the change of specific surface also corresponds to a change in the particle shape here. This also has a significant influence on suspension rheology. The elongated, needle-shaped particles tend to have the highest yield stress at constant solids content although they do not show the highest specific surface. Similar results have been reported in literature for various other material systems [63,68].

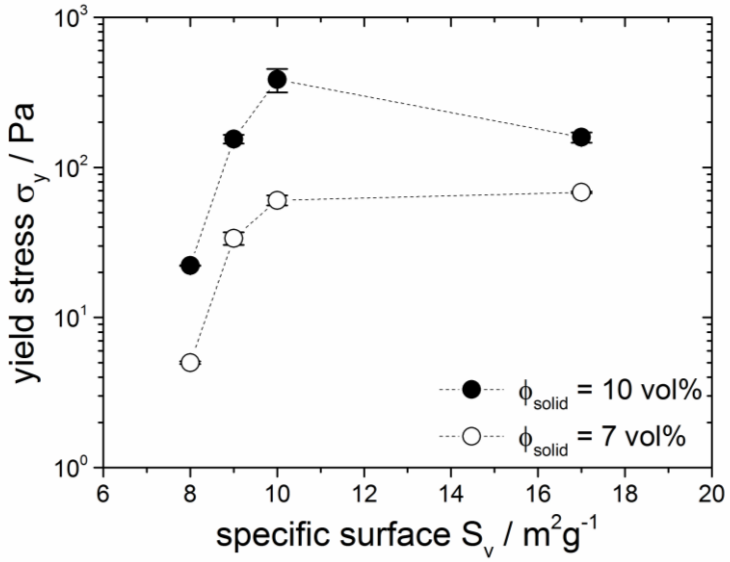

Fig. 14: Yield stress of suspensions consisting of PCC particles with varying particle shape dispersed in paraffin oil: spherical (Sv = 8 m²/g), scalenohedral (Sv = 9 m²/g), needle-shaped (Sv = 10 m²/g), plate-shaped (Sv = 17 m²/g). *Reproduced with permission from Elsevier.*

2.3.3 Rheology of Three-phase Suspensions

Yield stress data for three phase suspensions based on PCC particles with different shape have been obtained from steady and oscillatory shear rheometry. Fig. 15a shows corresponding results obtained at a particle loading ϕ_{solid} = 10 vol% as a function of secondary fluid content. Within experimental uncertainty yield stress values obtained in different ways agree very well for the suspensions investigated here and especially they reveal the same trends regarding the effect of secondary fluid content on yield stress, i.e. network strength within the suspensions.

As shown in Fig. 15a only the three phase suspensions including spherical and plate-shaped particles show the increase in yield stress upon addition of a secondary liquid phase typical for the so-called capillary suspensions with their strong capillary force controlled particle network [11]. The yield stress of suspensions consisting of plate-shaped particles increases by about a factor of ten while the spherical particles show an increase of about a factor of four compared to the yield stress of the respective pure suspensions $\sigma_{y,0}$. Whereas the yield stress of the plate-shaped particle suspensions exhibits an almost constant value for secondary fluid volume 2 % < ϕ_{sec} < 10 %, the yield stress of suspensions including spherical particles exhibits a pronounced maximum at $\phi_{sec} \approx$ 1-2 % and drops at higher ϕ_{sec} presumably due to spherical agglomeration [16]. Remarkably, elongated particles (scalenohedral and needle-shaped) do not show this behavior indicating that no capillary network is formed in these suspensions. An additional homogenization step in a ball mill did not change results significantly (data not shown here).

Characteristic differences regarding the effect of adding a secondary fluid to suspensions of different shaped particles showing up in yield stress measurements are further corroborated by storage modulus data. All suspensions show strong gel-like behavior with G' >> G'', but only when spherical or plate-shaped particles are included the addition of secondary fluid results in an increase in G' typical for capillary suspensions (Fig. 15b). A broad plateau of G' vs. ϕ_{sec} again is found for the plate-shaped particle suspensions, whereas a maximum in G' around $\phi_{sec} \approx 2$ % as well as a drop in G' at higher ϕ_{sec} again indicating spherical agglomeration is found for the suspensions including spherical particles [16].

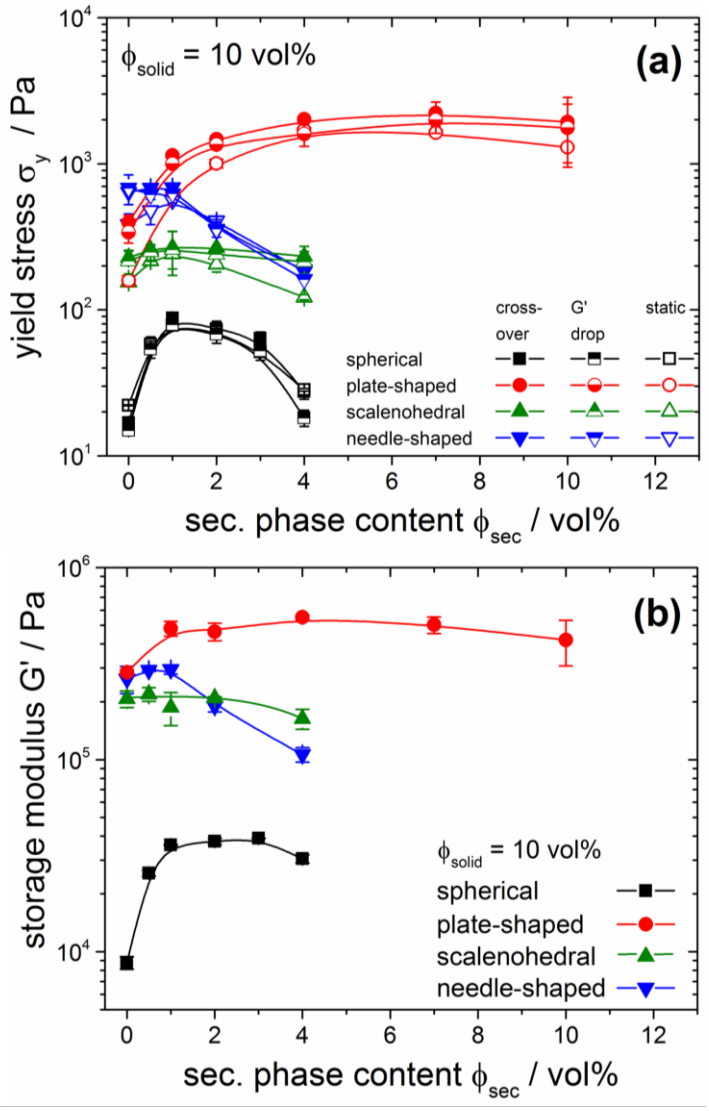

Fig. 15: (a) Yield stress σ_y vs. secondary phase content ϕ_{sec} for capillary suspensions consisting of PCC particles with varying particle shapes. Yield stress was determined with oscillatory shear experiments (crossover of G' and G'' in amplitude sweep; drop of G') and with steady shear experiments (vane geometry). Error bars are the standard deviation calculated from at least three measurements. (b) Storage modulus G' vs. secondary phase content ϕsec for three-phase suspensions consisting of PCC particles with varying particle shapes. G' from amplitude sweep measurements at a frequency ω = 1 s^{-1}. *Reproduced with permission from Elsevier.*

The pure two-phase suspension of the needle-shaped particles exhibits high σ_y and G' values indicating the existence of a strong particle network, but G' and σ_y do not increase upon addition of a secondary liquid instead both quantities quickly drop when the amount of secondary fluid is increased. So in this case the network cannot be reinforced by capillary forces, the drop in G' and σ_y instead may be due to spherical agglomeration.

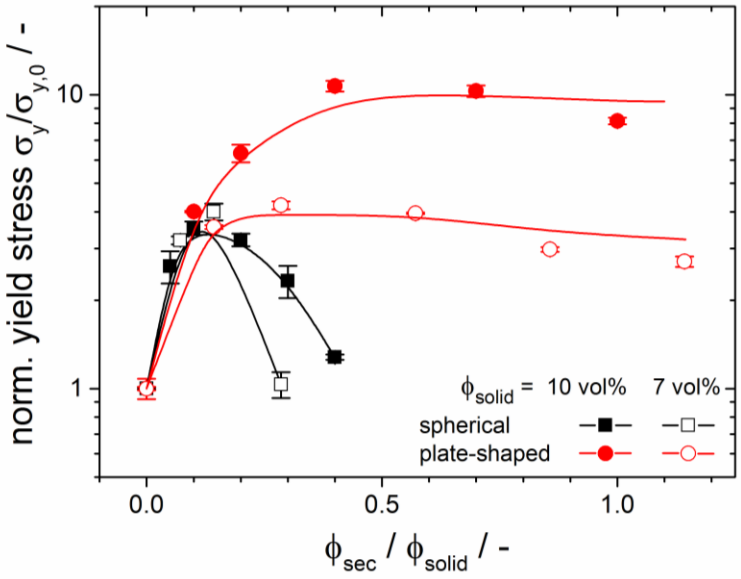

Fig. 16: Normalized yield stress σ_y / $\sigma_{y,0}$ vs. on particle solids fraction based secondary phase content ϕ_{sec} / ϕ_{solid}. Suspensions consist of spherical and plate-shaped PCC particles. *Reproduced with permission from Elsevier.*

An outstanding characteristic of the flake-shaped particles is the broad plateau observed in the σ_y and G' data. Obviously, these suspensions are able to incorporate large amounts of secondary liquid phase without change in rheological properties compared to spherical particles. This is directly evident from Fig. 16 where the relative increase in σ_y, i.e. $\sigma_y(\phi_{sec})$ / $\sigma_y(\phi_{sec}=0)$, is plotted vs. the ratio of secondary fluid volume ϕ_{sec} over particle volume fraction ϕ_{solid} for the plate-like and spherical particle suspensions at two different solids contents. For small ϕ_{sec} / ϕ_{solid} ratios, both types of suspensions exhibit a similar strong increase in yield stress. The suspensions with spherical particles then show a maximum in σ_y at ϕ_{sec} / ϕ_{solid} ≈ 0.1 and for the plate-shaped particle suspensions σ_y further increases to reach its maximum at ϕ_{sec} / ϕ_{solid} ≈ 0.3 - 0.4. When ϕ_{sec} / ϕ_{solid} = 0.1 is exceeded the normalized yield stress of suspensions including spherical particles drastically drops, and this decrease which is attributed to spherical agglomeration is more pronounced at lower particle loading since the lower number of aggregates can not provide a sample spanning network resulting in a measurable apparent yield

stress. In contrast, the normalized yield stress of suspensions with plate-like particle remains almost constant up to $\phi_{sec} / \phi_{solid} \approx 1$, i.e. the network existing in the plate-like particle suspensions can accommodate an equal volume of secondary fluid and particles without change in σ_y, only at $\phi_{sec} / \phi_{solid} > 1$ a weak decrease in σ_y (and also G') occurs presumably due to the formation of dense aggregates. The oblate particles tend to absorb much more secondary liquid until the capillary bridges are supersaturated and spherical agglomeration sets in.

We assume these differences in rheological behavior are related to the shape of capillary bridges formed in suspensions of spherical and plate-like particles. Spherical particles in an ideal pendular state capillary suspension exhibit strongly localized, point-like contacts [35,56]. Increasing the liquid volume in pendular capillary bridges between two spherical particles leads to a maximum value of the resulting capillary force at a critical volume of the bridge [79]. Exceeding this limit, the curvature of the capillary bridge changes from concave to convex [33,80]. This results in a positive Laplace pressure in the capillary bridge and hence a reduced capillary force finally leading to the collapse of the capillary particle network. The bridges oversaturate and depending on secondary fluid volume and particle wetting properties a funicular network morphology may occur. At high enough ϕ_{sec} spherical agglomerates, consisting of large secondary liquid droplets including the suspended particles are formed [16,31]. In contrast, the curvature of the capillary bridge between two plate-shaped particles remains constant until the capillary bridge is completely filled. Capillary force increases monotonically with increasing capillary bridge volume [79] and the transition to spherical agglomeration and network collapse does not happen before the capillary bridges are completely filled.

Another factor affecting network strength and rheology of suspensions is the number of particle contacts, i.e. the coordination number. In dense packed granular matter oblate particles show a higher coordination number than spheres [81,82]. Accordingly, oblate particles should be able to build up more capillary bridges among each other than spherical particles. This should result not only in a higher yield stress of the pure suspension (see Fig. 14), but also in a stronger increase of the normalized yield stress of the three-phase suspension if enough secondary fluid is provided as it seems to be the case for the plate-like particle suspensions investigated here at $\phi_{sec} / \phi_{solid} > 0.1$.

2.3.4 Microstructure in Three-phase Suspensions

Confocal laser scanning microscopy (CLSM) of wet suspensions and scanning electron microscopy of slightly sintered parts have been employed to gain insight into the microstructure of the investigated capillary suspensions consisting of PCC particles of different shapes.

Samples with different secondary fluid content have been investigated and we attempt to relate the observed structural features to the rheological properties discussed above.

Fig. 17 shows CLSM images of wet suspensions of plate-shaped (Fig. 17a-c) and needle-shaped (Fig. 17d-f) particles with varying amounts of secondary liquid. Using the reflection mode of the confocal microscope all interfaces in the samples are visible. The microstructure of the suspensions with and even without secondary fluid (i.e. without fluorescence die) is directly observable. For suspensions of plate-like PCC particles three types of microstructure are observed depending on secondary fluid content: Without secondary fluid the particles are homogeneously distributed and only small textured areas indicate a vdW particle network (Fig. 17a). At secondary fluid content of 4 vol% the sample spanning particle network and the coarsening of the microstructure similar as previous observed for suspensions of spherical ceramic particles is apparent from the formation of flocs lancing through the suspension (Fig. 17b). Further increasing ϕ_{sec} results in a distinct heterogeneous suspension characterized by dense agglomerates, typically for supersaturated capillary suspensions [16]. In contrast, CLSM images of suspensions including needle-shaped PCC particles show similar microstructure irrespective of secondary fluid content: For all investigated ϕ_{sec} spherical clusters dominate the microstructures of the suspensions. Adding a secondary fluid to a pure suspension (Fig. 17e) changes the microstructure barely. The supersaturated suspension (Fig. 17f) is inhomogeneous and exhibits spherical agglomerates, which were even visible macroscopically.

SEM images of slightly sintered suspensions enables to visualize the arrangement of single particles in suspensions of plate-shaped and needle-shaped PCC particles at a higher resolution compared to CLSM. The gentle processing route for preparing the sintered parts [16] conserves the wet suspensions without major changes in microstructure. Fig. 18 shows the orientation of plate-shaped and needle-shaped particles in pure suspensions and corresponding three-phase suspensions. In pure suspensions the plate-like particles are well dispersed and only small aggregates consisting of randomly oriented flakes are observable (Fig. 18a). In the three-phase suspension the flakes are strongly aggregated to large clusters (Fig. 18b). Aggregates of prevalently parallel orientated flakes are predominant and this is attributed to the capillary forces acting between the particles. The microstructure of suspensions with needle-shaped PCC particles barely changes upon adding secondary fluid. Aggregates of spherical character are predominant in sintered parts of the two- and three-phase suspensions (Fig. 18c, d).

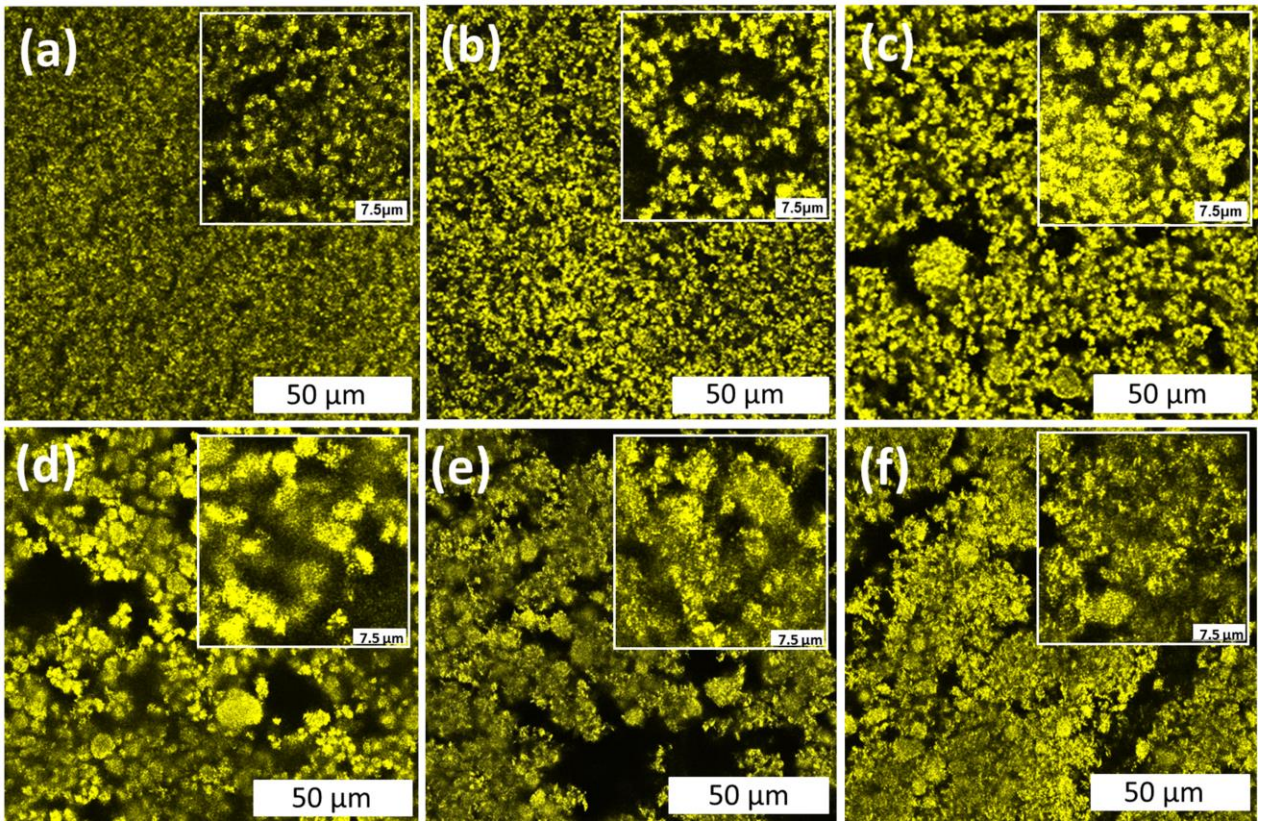

Fig. 17: CLSM images of two- and three-phase capillary suspensions consisting of PCC particles with different particle shapes (ϕ_{solid} = 10 vol%). Plate-shaped particles: (a) ϕ_{sec} = 0 vol%, (b) ϕ_{sec} = 4 vol%, (c) ϕ_{sec} = 10 vol%. Needle-shaped particles: (d) ϕ_{sec} = 0 vol%, (e) ϕ_{sec} = 1 vol%, (f) ϕ_{sec} = 4 vol%. *Reproduced with permission from Elsevier.*

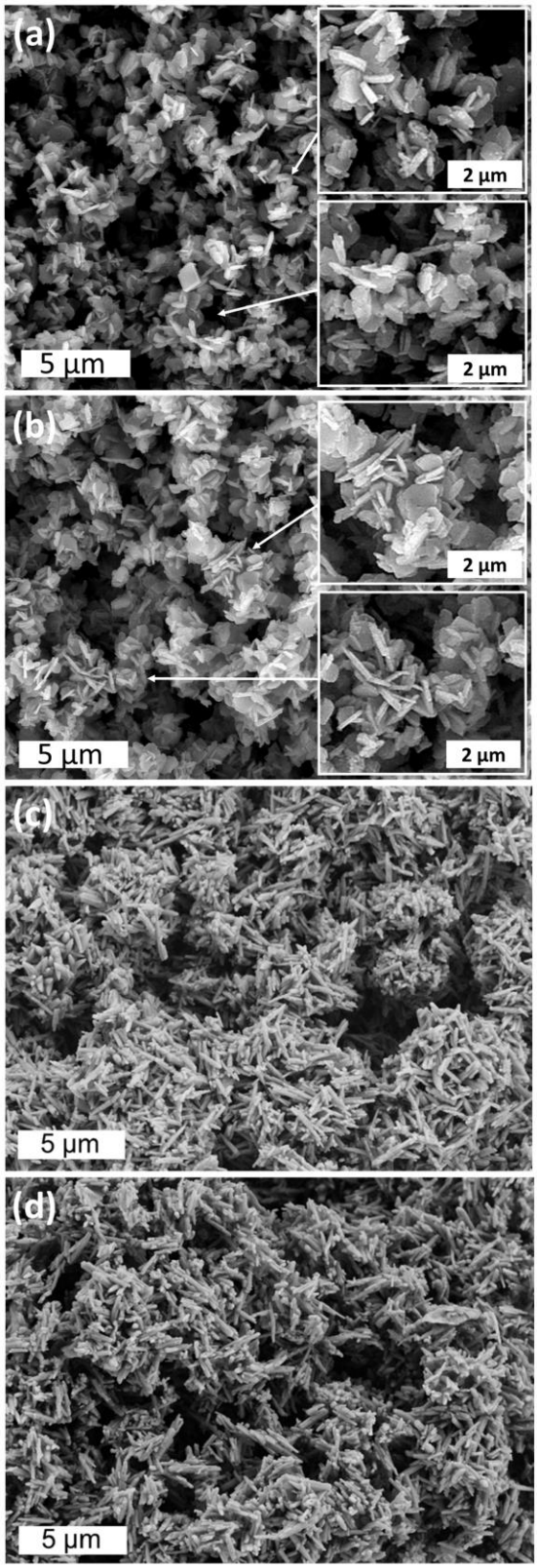

Fig. 18: SEM-images of slightly sintered suspensions, consisting of PCC particles. ϕ_{solid} = 10 vol%. Plate-shaped particles: (a) ϕ_{sec} = 0 vol%, (b) ϕ_{sec} = 4 vol%. Needle-shaped particles: (c) ϕ_{sec} = 0 vol%, (d) ϕ_{sec} = 1 vol%. *Reproduced with permission from Elsevier.*

The structural features observed in wet and solid state can be well correlated to the rheological behavior discussed in chapters 3.1 – 3.3. Choosing three-phase suspensions with a σ_y and G' value in the plateau area, the plate-like particles show the typical structure formation in a capillary suspension, visible as small flocs in CLSM images. Supersaturating the capillary bridges leads to the formation of dense aggregates, resulting in the before observed decrease of σ_y and G'. The feature of plate-shaped particles to orient parallel in three-phase suspensions (schematically shown in Fig. 19a) favors the ability to incorporate large amounts of secondary liquid phase without change in microstructure and rheological properties. In contrast, the needle-shaped particles do not show a distinct structure formation in three-phase suspensions, agreeing with the results of rheological measurements. Spherical agglomerates (Fig. 19b) dominate the suspensions already at low secondary fluid content.

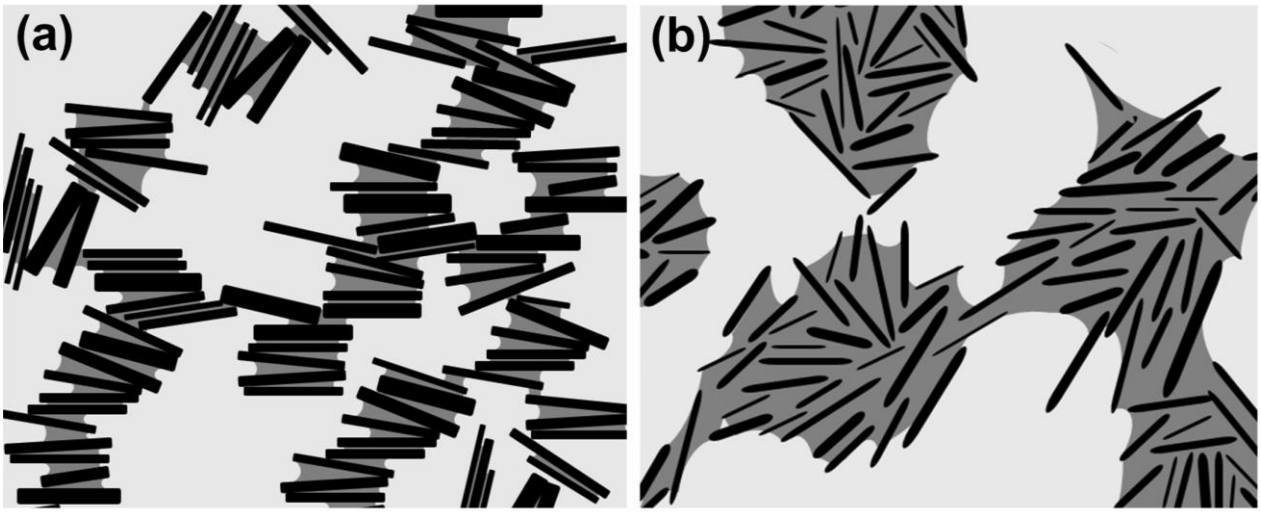

Fig. 19: Schematic images of three-phase suspensions with different particle shapes: (a) plate-shaped, (b) needle-shaped. Black: particles; dark grey: secondary fluid; light grey: bulk fluid. *Reproduced with permission from Elsevier.*

2.3.5 Three-phase Suspensions for Printed Electronics

2.3.5.1 Graphite Suspensions

Carbon based suspension systems are applied in various processes and fields of application, e.g. in the fabrication for Li-ion battery electrodes [83], supercapacitors [84] or gas-diffusion electrodes for Li-metal batteries and fuel cells [85–87]. Previously aqueous capillary suspensions containing spherical shaped graphite particles have been used to provide Li-ion battery anode pastes with tailor-made flow properties and superior coating behavior [15].

Here we employ spherical and plate-shaped graphite particles to create three-phase suspensions, using glycerol as bulk phase and 1-octanol as secondary liquid phase. Fig. 20 shows the yield stress σ_y as a function of $\phi_{sec} / \phi_{solid}$ for three-phase suspensions of plate-shaped and spherical graphite particles. Without added secondary fluid the graphite suspensions do not show a yield stress. However, upon addition of secondary fluid a yield stress σ_y occurs and increases rapidly with increasing amount of secondary fluid for both systems. A maximum in σ_y is reached around $\phi_{sec} / \phi_{solid}$ = 0.2 – 0.3 for the suspensions of spherical particles but σ_y decreases at higher amounts of secondary fluid due to spherical agglomeration. In contrast, the yield stress exhibits a broad plateau ranging from $\phi_{sec} / \phi_{solid}$ = 0.25 – 1 for the three-phase suspensions of plate-shaped particles with no indication of spherical agglomeration. Qualitatively this is similar to what is found for PCC particles.

For both systems we assume the formation of a sample spanning network induced by capillary forces acting among suspended particles, i.e. formation of capillary suspensions.

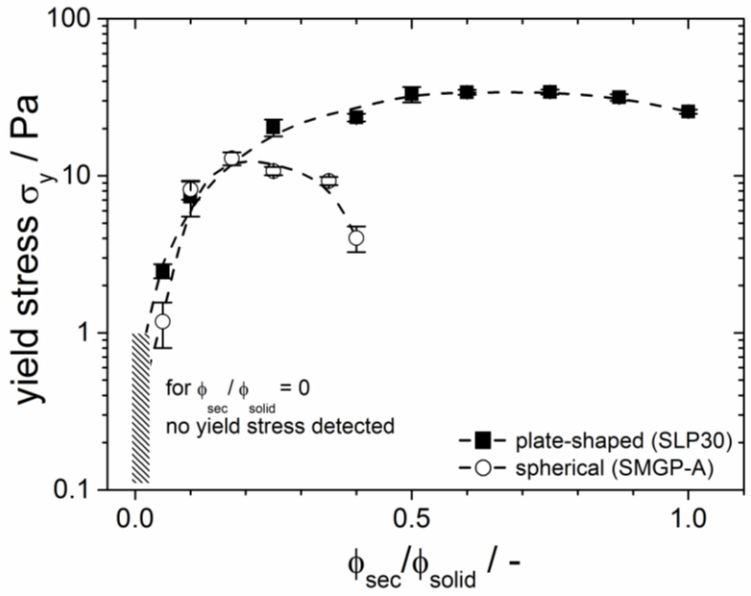

Fig. 20: Yield stress σ_y as function of $\phi_{sec} / \phi_{solid}$ for graphite based three-phase suspensions using spherical and plate-shaped particles (ϕ_{solid} = 20 vol%). Bulk fluid: glycerol, secondary fluid: 1-octanol. The shaded area indicates that no reliable yield stress values can be determined at stresses below 1 Pa for the two phase graphite suspensions investigated here. The dashed lines are to guide the eye. *Reproduced with permission from Elsevier.*

2.3.5.2 Aluminum Particles

Flake shaped Aluminum pigments are widely used in metallic automotive coatings to provide the desired gloss [88]. But they may also be used to print conductive fine lines or thin uniform layers

in electronic applications. In both cases the particle aspect ratio has a strong impact of the final product properties.

Fig. 21 shows the yield stress vs. ϕ_{sec} / ϕ_{solid} for three-phase suspensions of oblate aluminum particles with two different aspect ratios (pigment 1: r = 0.013, pigment 2: r = 0.020). The solids content of both two-phase suspensions was chosen such that their respective yield stress values approximately match (ϕ_{solid} = 10 vol% for pigment 1 and ϕ_{solid} = 18 vol% for pigment 2).

In both cases the yield stress increases monotonically with increasing ratio of secondary fluid to solids volume fraction and an almost tenfold increase in σ_y is achieved. This is considered as a clear indication for the formation of a strong capillary force controlled particle network, i.e. capillary suspensions are created. The yield stress increases monotonically until a critical ratio ϕ_{sec} / ϕ_{solid} of 0.7 and 1.6, respectively, is reached. No macroscopically visible spherical agglomeration was observed up to this ϕ_{sec} / ϕ_{solid} ratio. But at higher ϕ_{sec} / ϕ_{solid} values no homogeneous three-phase suspensions could be formed and the added secondary fluid could not be completely dispersed anymore. The capillary suspensions made from pigment 1 with the lower aspect ratio can accommodate more secondary fluid relative to the particle volume as revealed by the different critical ϕ_{sec} / ϕ_{solid} ratios. The increase in σ_y is more pronounced for the suspension made from pigment 2 with the higher aspect ratio. This might be due to the higher particle volume fraction leading to a different network structure [48].

No further interpretation can be provided on the basis of the currently available data a more quantitative investigation of the capillary suspension phenomenon for systems including anisotropic particles warrants further research work.

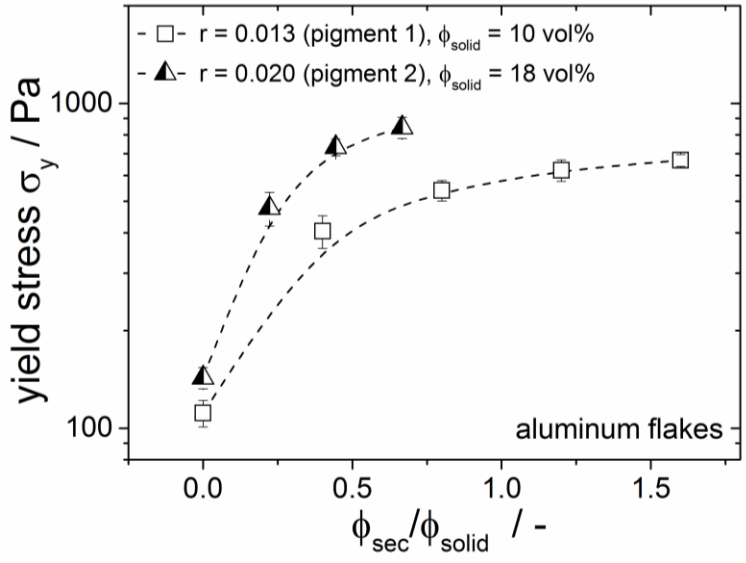

Fig. 21: Yield stress σ_y vs. ϕ_{sec} / ϕ_{solid} for suspensions consisting of aluminum flakes with varying aspect ratio. Bulk fluid: mixture of paraffin oil and mineral spirit. Secondary fluid: pure water. *Reproduced with permission from Elsevier.*

2.4 Conclusions

We investigated the rheological behavior and the microstructure of two- and three-phase suspensions consisting of precipitated calcium carbonate (PCC) particles with different shape (spherical, scalenohedral, needle-shaped, plate-shaped) as model systems in order to address the question how particle shape affects the formation of capillary force controlled sample-spanning networks upon addition of a secondary, immiscible fluid. Furthermore, we determined the rheological behavior of three-phase suspensions of graphite particles with different shapes and flake-shaped aluminum pigments with different aspect ratio, recognizing the particular technical importance of these particle systems.

At the investigated particle loading of 7 vol% and 10 vol% two-phase suspensions consisting of PCC particles show a strong gel-like behavior and yield stress strongly depends on specific surface and aspect ratio of the particles. Three-phase suspensions consisting of plate-like and spherical PCC particles show a drastic increase in σ_y and G' upon addition of the secondary fluid characteristic for capillary suspensions. For suspensions of spherical particles the rheological quantities strongly increase with increasing ϕ_{sec} to reach a maximum at $\phi_{sec} / \phi_{solid} \approx 0.1 – 0.2$ but they drastically drop at higher $\phi_{sec} / \phi_{solid}$ and spherical agglomeration sets in. Suspensions of plate-like particles show a broad plateau in σ_y and G' at secondary fluid contents between $\phi_{sec} / \phi_{solid} = 0.2 – 1$ and only a weak decrease in σ_y at $\phi_{sec} / \phi_{solid} > 1$, presumably due to the formation of dense aggregates. The differences in rheological behavior of these differently shaped particles are assumed to be related to the shape of capillary bridges formed in the suspensions. Spherical particles show "point-like" bridges, which can be oversaturated already at low ϕ_{sec}. Capillary bridges between plate-like particles absorb large liquid volumes without supersaturating and collapsing.

Suspensions of elongated (scalenohedral, needle-shaped) PCC particles do not show a significant increase in σ_y and G' upon addition of secondary fluid, but these quantities strongly decrease for $\phi_{sec} / \phi_{solid} > 0.1$ due to the onset of spherical agglomeration.

CLSM and SEM imaging were utilized to investigate the microstructure of wet and slightly sintered PCC suspensions, respectively. For plate-shaped PCC particles formation of aggregates typical for three-phase so-called capillary suspensions and a preferential parallel orientation of the flakes was observed in the presence of the secondary, immiscible fluid. Suspensions of needle-shaped particles did not show significant differences in microstructure comparing two-phase with three-phase suspensions.

Finally, we investigated the effect of secondary fluid content on yield stress for graphite suspensions consisting of spherical and plate-shaped particles, and we observed similar

behavior as for corresponding PCC suspensions, i.e. the plate shaped particles can accommodate much higher fractions of secondary fluid without spherical agglomeration than spherical particles. Investigating suspensions of flake-shaped aluminum particles we observed a monotonic increase in σ_y with increasing $\phi_{sec} / \phi_{solid}$ ratio up to a critical value of this ratio beyond which homogeneous suspensions could not be prepared anymore. This increase in σ_y is more pronounced for the suspensions of particles with the higher aspect ratio but due to this higher aspect ratio the maximum relative amount of secondary fluid which can be accommodated inside the capillary bridges is lower in this case.

A deeper quantitative evaluation and investigation of capillary suspensions requires a broader data base including a series of particle systems with well-defined size, shape and surface properties varying in a broad parameter range. This has to be addressed in future work aiming at a prediction of important rheological quantities like yield stress and shear modulus as a function of particle volume fraction, size, shape and surface properties as well as type and amount of secondary fluid. In particular it will be important to determine the shape and volume of liquid bridges between plate-like particles and to evaluate how this affects structure and flow of the corresponding three-phase suspensions.

2.5 Acknowledgement

We would like to thank the SCHAEFFER KALK GmbH & Co. KG and the Schlenk Metallic Pigments GmbH for the donation of PCC particles and aluminum pigments as well as the smooth collaboration. The authors acknowledge the Competence-E project (KIT) for donation of graphite particles. Further thanks are given to Thomas Lebe for the work at the SEM-microscope and Klaus Hirsch for the particle size analysis. Frank Bossler is thanked for providing confocal laser microscope images and fruitful discussions. We acknowledge experimental support by Katrin Dyhr and Torsten Schick.

3 Fabrication of highly porous glass filters using capillary suspension processing

Full title: Fabrication of highly porous glass filters using capillary suspension processing

Authors: Johannes Maurath, Jens Dittmann, Niko Schultz, Norbert Willenbacher

Status: published

Bibliographic data: Separation and Purification Technology 149 (2015) 470-478
10.1016/j.seppur.2015.06.022

Abstract

We present a novel, capillary suspension based processing route for sintered glass filters with porosities ≥ 50 % at average pore sizes between 1 – 50 µm. This new kind of glass filters exhibits narrow pore size distribution and uniform pore structure. Pores are exceptionally smooth and round. Accordingly, permeability and mechanical strength of these filters excel that of similarly processed ceramic and commercial glass filters significantly.

Mechanical strength at a given porosity is much higher than that of commercial glass filters and reaches values similar to that of ceramic filters with distinctly higher matrix strength. Absolute values are well predicted by the Gibson & Ashby model $\sigma_c/\sigma_{f,0} = B_0 (1-\varepsilon)^z$ with $B_0 = 0.8$. Liquid permeability varies with pore size according to Darcy's law but absolute values are clearly higher than that for ceramic filters at given pore size as expected from the smoother pore structure. Gas permeability is especially high at pore sizes < 10 µm and exceeds that of ceramic and commercial glass filters significantly. Moreover, this results in a weaker than quadratic pore size dependence. This is presumably due to slip effects occurring especially in small pores and narrow necks of the novel glass filters.

4.1 Introduction

In the field of microfiltration the increasing number of applications at high temperatures, covering greater pH ranges and including chemically more aggressive media results in a need of

inorganic filter media [89,90]. Inorganic filters become increasingly popular for large volume solid-liquid separation processes such as in waste water recycling or drinking water treatment [1,2]. Furthermore, inorganic filters or membranes find their applications in industrial hot gas cleaning processes [3] or for the purification of liquid metals [4]. As polymeric materials cannot withstand the extreme conditions regarding temperature, chemical and mechanical resistance occurring in the exemplified applications, there is a strong trend to ceramic and glass filter media for industrial purposes. Their outstanding chemical resistance is a key advantage of glass filters. Since the chemical resistance is dependent of the composition of the glass itself, it is obvious to choose an appropriate glass for the respective scope of application. Borosilicate glasses are examples for high resistant glasses which are applied for nearly all kinds of laboratory glassware. Their hydrolytic, acidic and basic resistance is high even at elevated temperatures. Furthermore, these properties are for some kinds of glasses combined with a high thermal shock resistance. Therefore, potential fields of application of the glass filters presented here range from beverage industries [1,91], over gas filtration purposes to applications in laboratory equipment. The smooth pore structure and the narrow pore size distribution are promising indicators for a good fouling resistance, good back flushing behavior and a narrow cut-off range. As the manufacturing of fine granulated and fractured glass powders can be expensive, but the sintering process is performed at temperatures well below sintering temperatures of ceramic materials, the specific costs of these glass filters range in between polymer and ceramic filters.

Typical established filters made of glass are either fiber filters, leached glass membranes, porous silica glass prepared via the sol-gel process or sintered glasses. Nearly all subsequently summarized manufacturing methods not only apply to glass but also for manufacturing metallic [92,93] or ceramic filters [22,94], while sol-gel processes are exclusively for non-metallic materials and leaching is a typical manufacturing method for microporous glass membranes. For fiber filters in pad or blanket form the thin glass fibers are bound together by their intrinsic properties or by impregnation of the sheets with suitable resins or adhesives. Typical pore sizes are in the range of 1 up to 50 µm [95,96]. Via phase separation and leaching of alkali glasses porous membranes with pore sizes in the range of 1 - 1000 nm are achieved. After forming the glass part a heat treatment in the temperature range between 500 - 700 °C initiates a phase separation. Two different phases arise from the homogeneous glass, while an alkali-rich phase can be leached out by mineral acids, alcohols or water at moderate temperature (RT up to 100 °C). Since the other phase is almost pure silica, a porous glass with silica content of about 96 % is achieved [97]. Glasses with pore sizes below 1 µm also result from the sol gel-process. Here a silicate suspension gets gelled in a chemical reaction, dried and sintered in a following heat treatment [98]. The processes introduced above are most common but porous glass filters can

also be produced via sintering processes. This provides better control of pore size, porosity, pore shape and uniformity. Sintered filters own a higher mechanical strength and a higher heat resistance than the cheaper glass fiber filters, where organic binders often limit the operating temperature [99]. The sintering of glass powder via the sacrificial templating method where additional fillers (e.g. salts, organic materials) are added as pore forming agents is limited to pore sizes between 20 – 200 µm [97]. A further technique for manufacturing porous sintering materials is the replica technique. Natural or synthetic organic templates are filled with a suspension of glass particles. After drying of the infiltrated templates all organic components get pyrolized in a debinding step, the following sintering step consolidates the replicated structure [97,100], and typically pore sizes > 10 µm are achieved [22]. Enke et al. [97,100] reported about the combination of these two methods with the leaching technique. Glass monoliths with a hierarchical porosity and a bimodal pore size distribution can be manufactured. Furthermore, the partial sintering is a common manufacturing method for porous sintering materials. The final products exhibit a wide size range of open pores [22,101]. Various companies (e.g. DURAN Group GmbH, Heraeus Quarzglas GmbH & Co. KG) produce porous glass frits and filters in the pore size range between 1 – 300 µm, while in products with pore sizes < 60 µm porosities are well below 40%.

The processing route based on capillary suspensions as presented here allows for manufacturing sintered filters with a porosity > 50% and average pore sizes in a range of 1 - 50 µm. Porosity and pore sizes are the result of the controlled heterogenization of suspensions using capillary forces. The particle network structure of these so-called capillary suspensions can be preserved even in the sintered part. Ceramic capillary suspensions were already successfully applied as precursors for manufacturing porous ceramics [10,16].

Capillary suspensions, disperse systems consisting of a solid and two immiscible fluid phases, represent a distinct class of materials. Particles are essentially suspended in the major or so-called bulk fluid phase. The secondary fluid phase occupies only a small fraction of the liquid volume (< 5 vol%), which is trapped in the capillary bridges formed at the particle contact points [11].

Adding an appropriate secondary liquid phase to a suspension changes the rheological behavior from fluid or weakly elastic to gel-like. In the pure suspension the particles are either well dispersed or they form already a sample-spanning fractal network due to dominating van-der-Waals attraction. Upon addition of the secondary fluid capillary bridges between particles are formed.

Since capillary suspensions based on glass and ceramic particles show such a strong and easy to control structure formation they can be used as precursor for highly porous sintering

materials. The homogeneous sample spanning network can be preserved even during debinding and completely open-porous sintered parts are accessible. The manufacturing of macroporous ceramic sintered parts based on capillary suspensions [10] and their microstructure and mechanical strength in dependence of secondary phase content [16] have been described earlier. Now we discuss the processing of sintered glass filters manufactured with this new processing route. We demonstrate that the filters based on capillary suspensions and glass powder show significant advantages regarding permeability compared to ceramic and commercial glass filters. Moreover, the mechanical strength reaches similar values as ceramic filters at a given porosity.

4.2 Experimental

The experiments were carried out using a capillary suspension system based on glass with a composition similar to borosilicate glass in three different particle sizes as solid phase, paraffin oil as bulk fluid phase and an aqueous sucrose solution as the secondary fluid phase. With this material system we fabricated sintered parts for microstructural characterization, mechanical strength measurements and filtration tests.

4.2.1 Raw Materials

Glass powders with compositions similar to borosilicate glasses (Technical Glass G018-361; SCHOTT AG, Mainz, Germany) with three different particle sizes and density ρ = 2.75 g/cm³ were used. The particle size distribution as determined through Fraunhofer diffraction (Helos H0309; Sympatec GmbH, Clausthal-Zellerfeld, Germany) using in water dispersed particles in an ultrasonic wet dispersing unit (Quixel and Cuvette, Sympatec GmbH) for all three glass species is shown in Fig. 22. Obviously, Glass 2 exhibits a monomodal fairly narrow particle size distribution, whereas the other two powders show a broad slightly bimodal size distribution. The average volume based diameters are $x_{50,3}$ = 11.0 µm (glass 1), $x_{50,3}$ = 1.1 µm (glass 2) and $x_{50,3}$ = 0.6 µm (glass 3). Scanning-electron-microscopy (SEM) micrographs (S-4500; Hitachi High-Technologies Europe GmbH, Krefeld, Germany) helped to get information about the particle morphology (Fig. 22). The bulk phase was paraffin oil (Carl Roth, Karlsruhe, Germany) with a Newtonian flow behavior and a dynamic viscosity η(20 °C) = 0.03 Pa·s. To prevent unwanted agglomeration in the pure suspensions of glass 3 the nonionic wetting agent Polysorbat 20 (Tween20; Carl Roth, Karlsruhe, Germany) with HLB = 16.7 was used. The secondary phase was a 1.853 M aqueous sucrose solution. The D(+)-sucrose (Carl Roth, Karlsruhe, Germany)

was dissolved in distilled water at 20 °C. The solution shows a dynamic viscosity of η(20 °C) = 0.08 Pa·s.

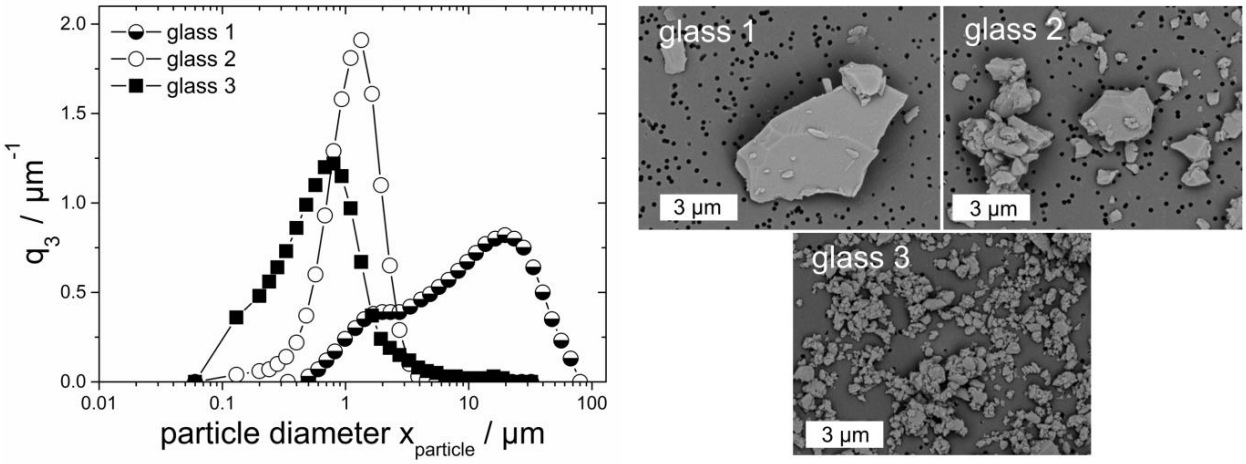

Fig. 22: Particle size analysis and SEM images of the used raw glass powders. Differential particle size distribution q_3 was determined through Fraunhofer diffraction. *Reproduced with permission from Elsevier.*

4.2.2 Processing Route

The main processing steps for manufacturing porous glasses based on capillary suspensions are summarized in the following flow sheet (Fig. 23). Pure suspensions were prepared by mixing the solid powder into the bulk phase with a high shear dissolver at a speed of 1200 rpm for 10 min. For a better homogenization the pure suspensions were then treated in a self-constructed ball mill for 24 h. Adding a small amount of surfactant (0.7 vol% of the bulk fluid phase) to suspensions consisting of glass 3 prevents unwanted agglomeration. The capillary network formation is induced by adding the secondary fluid phase to the pure suspension again using a high shear dissolver at a speed of 800 rpm for 5 min, followed by a period of 2 min with reduced stirring speed at 500 rpm. A final homogenization step in a ball mill with a rotation speed of 18 rpm and 25 mm balls for 24 – 48 h (depending on particle size) allows for the formation of homogeneous capillary suspensions without agglomerates. The solid content of the prepared capillary suspensions was between ϕ = 10 – 20 vol%. Next to capillary suspensions consisting of one powder fraction, also mixtures consisting of glass 1 and glass 2 as well as glass 2 and glass 3 were used. Sintered parts with pore sizes in between those obtained from suspensions including a single powder were thus available.

After the preparation of homogeneous, agglomerate-free capillary suspensions the pastes were molded by hand into sample forms and the top face was smoothed using a doctor blade. For mechanical strength tests we used rectangular forms with the size 50 mm x 12 mm x 5 mm and

for filters we used circular forms with a diameter of 42 mm and a height of 5 mm. Placing the sample forms on an absorbing pad allowed debinding of the samples immediately after forming. Samples were bedded on an absorbing pad for 10 days at room temperature to debind the bulk phase by capillary extraction. The binder dissolved in the secondary phase crystallizes in the capillary bridges as the secondary phase is removed by evaporation and helps to create stable and portable green parts. The following thermal debinding step in a debinding oven at 200 °C (30 min) and 500 °C (60 min) on a porous ceramic plate ensured a complete and gentle debinding of the residual bulk fluid and the sucrose. The debinded samples were sintered at temperatures depending on the particle size of the solid powder such that an open porosity ε = 50 % was reached for the sintered parts. Samples of glass 1 were sintered at 820 °C for 15 min, samples of glass 2 were sintered at 785 °C for 15 min and samples of glass 3 were sintered at 760 °C for 15 min. Sintering temperatures for the powder mixtures were in between the temperatures selected for the respective pure powders.

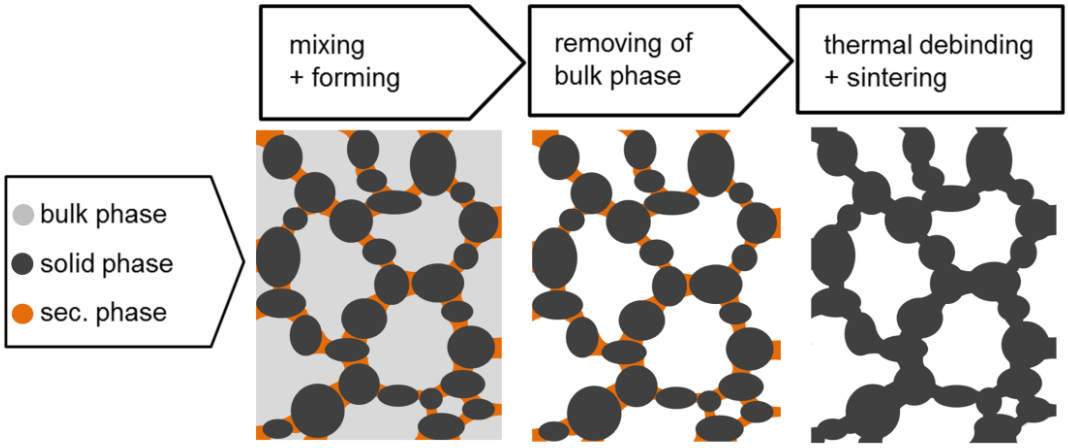

Fig. 23: Main steps of the processing route for manufacturing macroporous glass filters based on capillary suspensions. *Reproduced with permission from Elsevier.*

4.2.3 Characterization

Rheological characterization of the suspensions was done using a rotational rheometer (Haake Mars II; Thermo Scientific, Karlsruhe, Germany). A plate/plate geometry (diameter: 35 µm) was employed for viscosity measurements and a vane geometry (Z20 according to DIN 53019-1) for yield stress measurements [78]. Viscosity were obtained from shear rate ramp tests (shear rate range $\dot{\gamma}$ = 10 –1000 1/s), yield stress measurements were carried out using shear stress ramps (shear stress range σ = 0.1 – 1000 Pa). Yield stress values were calculated from deformation vs. stress curves according to the tangential method [102].

Surface and interfacial tension of the fluids were determined with a tensiometer (DCAT 11; DataPhysics Instruments GmbH, Filderstadt, Germany) equipped with a Wilhelmy-plate. For contact angle measurements we used an uncoated borosilicate glass cover slip (Carl Roth, Karlsruhe, Germany). The contact angles of the fluids to the used glass against air (θ_{Ba}, θ_{Sa}) were determined with the sessile-drop method (OCA 15; Dataphysics) by a numerical fit of the Young-Laplace equation to the imaged drop shape [36].

The porosity ε of the sintered parts was calculated from the Archimedes density according to DIN EN 993-1.

Image analysis of electron micrographs (Line Intercept Count Method [36]) was used to determine the pore size distribution of the sintered parts. Therefore, the sintered parts were infiltrated with epoxy resin and after grinding and polishing steps SEM crosscut images (backscattering-mode, S-4500; Hitachi) were used for image analysis. Pore size distribution $q_3(x_{pore})$ and average pore size $x_{pore,av}$ were calculated from at least three SEM images. SEM imaging was chosen here for pore size characterization since it provides additional information about the pore shape in contrast to other methods like Hg-porosimetry.

For mechanical strength measurements the flexural strength σ_f (4-point bending test following DIN EN 843-1) and the compressive strength σ_c (following DIN 51104) were determined.

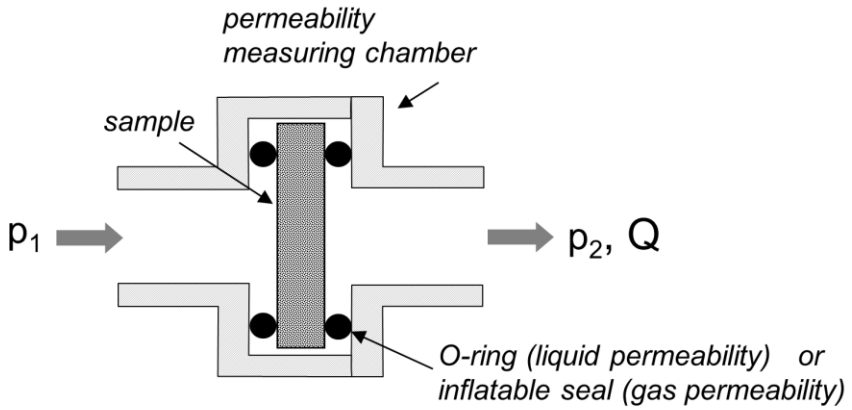

Fig. 24: Schematic model of equipment for gas and liquid permeametry. *Reproduced with permission from Elsevier.*

Permeability tests were performed to characterize filtration properties of the filter disks. The gas permeability was determined following DIN EN 993-4 and the liquid permeability (water as liquid) was measured with a pressure strainer (DrM, Maennedorf, Switzerland). Volumetric flow rate was measured with a rotameter (for gas permeability) and an electronic balance (for liquid

permeability), respectively. Gas and liquid permeability k_g and k_l of the porous glass disks was evaluated using eq. (7):

$$k_{g/l} = \frac{L}{A}\eta\frac{Q}{\Delta p} \quad (7)$$

where $\Delta p = p_1 - p_2$ is the pressure drop between entrance and exit of the sample, k_g and k_l are Darcy's permeability coefficients, η the dynamic viscosity of the test fluid. L and A are the thickness and the cross sectional area of the sample, Q the volumetric flow rate of the fluid. Fig. 24 shows a schematic of the used measuring chamber. As-fired circular disks were grinded to an average diameter of 26 ± 1 mm and a height of 2 ± 0.1 mm for the filtration tests. We converted the gas flow Q at ambient pressure with the ideal gas law to the gas flow Q at the pressure predominant in the mid of the filter $p_M = (p_1 - p_2) / 2$ to consider the compressibility. For each sample we chose up to 5 pairs of Δp and Q values to get a good average of the permeability k.

4.3 Results and Discussion

With the extended Young-Dupré equation [11] the three-phase contact angle θ_{SB} of the material system was calculated from the surface tensions of the surrounding bulk phase Γ_{Ba} = 29.8 ± 0.2 mN/m and the secondary phase Γ_{Sa} = 76.1 ± 0.6 mN/m, the interfacial tension of the two fluids Γ_{SB} = 41.7 ± 0.2 mN/m and the contact angles of the fluids against air θ_{Sa} = 64.1 ± 3.2 °, θ_{Ba} = 0 °:

$$\cos\theta_{SB} = \frac{\Gamma_{Sa}cos\theta_{Sa} - \Gamma_{Ba}cos\theta_{Ba}}{\Gamma_{SB}} \quad (8)$$

The three-phase contact angle was calculated as θ_{SB} = 85.4 ± 5 °, so the particles in this material system are connected via pendular shaped bridges [100].

4.3.1 Rheological Characterization

Fig. 25 shows the yield stress σ_y and dynamic viscosity η for suspensions of glass particles with various secondary phase contents ϕ_{sec} up to 4 vol% of the total sample volume. At constant solids content ϕ and particle size $x_{50,3}$ we see a strong increase of yield stress and viscosity resulting from the structure formation in the capillary suspension. Increasing the secondary phase content to values ϕ_{sec} > 1 vol% results in a plateau of σ_y, since most of the capillary

bridges are saturated. In this regime homogeneous capillary suspensions exist, which suit well as precursors for sintering materials [10,16].

Particle size also has a strong influence on the rheological behavior. Despite of the lower solids content in glass 2 suspensions ($x_{50,3}$ = 1.1 µm) compared to suspensions of glass 1 ($x_{50,3}$ = 11.0 µm), glass 2 suspensions have a higher yield stress. This results from the higher number of capillary bridges per volume in suspensions including smaller particles.

Our rheological data prove that we can create two fluid suspensions based on the glass particles used here. We get stable capillary suspensions with a characteristic structure formation similar to that already observed for other material systems [10,11,16] as will be discussed in the next section.

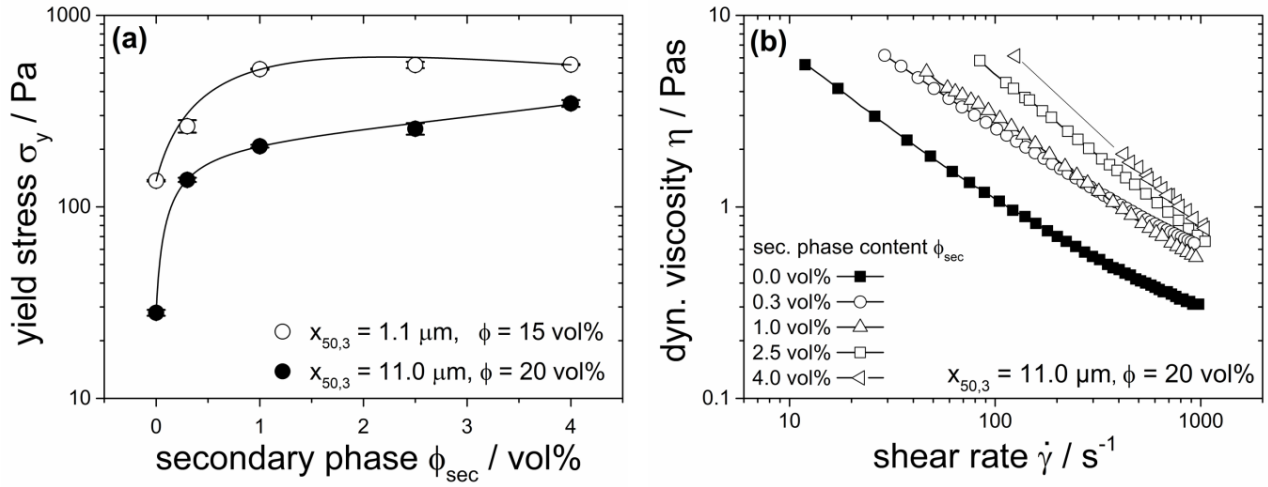

Fig. 25: (a) Yield stress σ_y vs secondary phase content ϕ_{sec} for capillary suspensions with two different average particle sizes $x_{50,3}$ and solids content ϕ, (b) dynamic viscosity η as a function of the shear rate for varying secondary phase content at constant solids content and constant particle size. *Reproduced with permission from Elsevier.*

4.3.2 Structure Formation: Porosity and Pore Size

Porosity ε and average pore size $x_{pore,av}$ are the key parameters quantifying the structure of the sintered parts. In order to quantify the influence of the added secondary phase on structure formation constant sintering conditions (temperature profile, time) have been chosen for a given particle size.

SEM crosscut images of sintered parts consisting of glass 2 shown in Fig. 26 disclose the structural difference between sintered parts made from a regular and a capillary suspension. Both SEM images show a smooth pore shape but it is clearly visible that the pore structure changes drastically after addition of the secondary fluid. The open porosity ε increases from ~34 % to ~50 %, while the pore size increases nearly by a factor of 2, from $x_{pore,av}$ = 2.6 ± 0.2 µm

to $x_{pore,av}$ = 4.0 ± 1.1 µm, comparing sintered parts from pure suspension to those from capillary suspensions. Similar behavior was found for suspensions of glass 1 and glass 3 and sintered parts made thereof, cf. Table 3. The strong increase of the yield stress in the wet state directly correlates to the increase in porosity and pore size in the solid state.

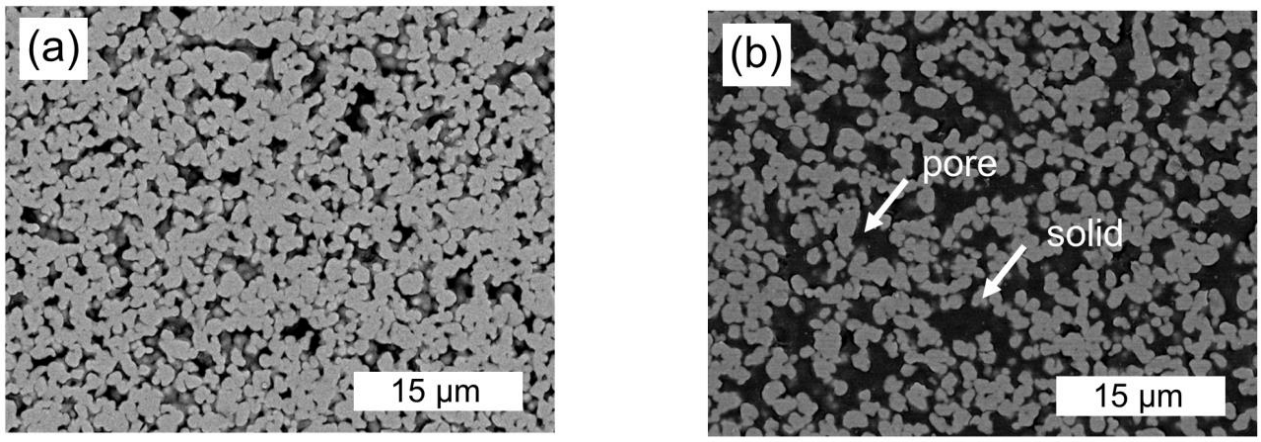

Fig. 26: SEM crosscut images of sintered parts of a pure suspension and a capillary suspension consisting of glass 2 as initial powder. (a) ϕ_{sec} = 0 %, ε = 34%, $x_{pore,av}$ = 2.6 ± 0.2 µm, (b) ϕ_{sec} = 2.5 %, ε = 51%, $x_{pore,av}$ = 4.0 ± 1.1 µm. Sintering conditions constant: T_{sinter} = 785 °C, t_{sinter} = 15 min. Solid particles appear light gray and pores as black. *Reproduced with permission from Elsevier.*

Table 3: Yield stress data σ_y of suspensions and appropriate capillary suspensions, porosity ε and av. pore size $x_{pore,av}$ of sintered parts consisting of glass 1, glass 2 and glass 3 as initial powder. The given failures are the standard deviation of at least three measurements.

	glass 1		**glass 2**		**glass 3**	
sec. liquid ϕ_{sec} / vol%	0.0	2.5	0.0	2.5	0.0	2.5
yield stress σ_y / Pa	28 ± 1	257 ± 18	137 ± 2	551 ± 21	139 ± 7	688 ± 72
porosity ε / %	18 ± 4	50 ± 1	34 ± 7	50 ± 2	39 ± 1	50 ± 2
pore size $x_{pore,av}$ / µm	-	49.6 ± 4.2	2.6 ± 0.2	4.0 ± 1.1	-	1.5 ± 0.1

Changing the initial particle size allows for a variation of the average pore size in the sintered parts at constant porosity. This is shown in Fig. 27 displaying pore size distributions for sintered parts made from capillary suspensions based on the three glass powders shown in Fig. 22. Solids fraction in the wet suspensions and sintering conditions were adjusted that a constant porosity ε = 50 % was achieved in all cases. The normalized differential pore size distributions q_3/q_3(modal) are mainly monomodal with a sharp cut to bigger pores. Obviously the pore size in the sintered part can be controlled directly by the initial particle size in the capillary suspension.

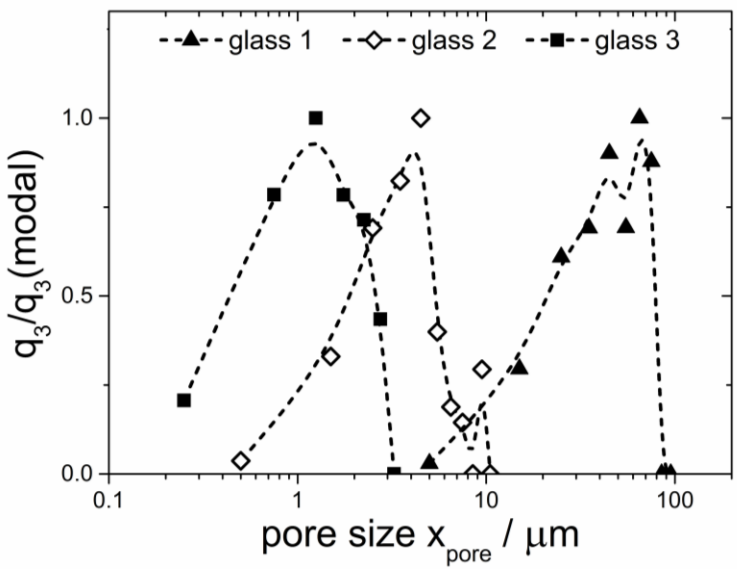

Fig. 27: Normalized differential pore size distribution q_3/q_3(modal) for sintered parts based on capillary suspensions, consisting of glass 1 (ϕ = 20 vol%, ϕ_{sec} = 2.5 vol%, T_{sinter} = 820 °C, t_{sinter} = 15 min), glass 2 (ϕ = 15 vol%, ϕ_{sec} = 2.5 vol%, T_{sinter} = 785 °C, t_{sinter} = 15 min) and glass 3 (ϕ = 20 vol%, ϕ_{sec} = 2.5 vol%, T_{sinter} = 760 °C, t_{sinter} = 15 min) as initial powder. Porosity ε = const. = 50 ± 3%. Pore size distributions determined via image analysis. *Reproduced with permission from Elsevier.*

4.3.3 Mechanical Strength

We determined the compressive and flexural strength of sintered parts made from capillary suspensions of the three different glass powders at a constant porosity $\varepsilon = 50 \pm 3$ %. Data shown in Fig. 28 are average values and standard deviations obtained from at least 10 specimen of each sample for compressive strength and 5 specimen of each sample for flexural strength. Average values of the compressive strength are between σ_c = 14.7 – 21.4 MPa and the flexural strength σ_f ranges between 4.6 and 10.3 MPa. Obviously, the average compressive strength is about a factor of two bigger than the flexural strength. As expected [16], the mechanical strength is essentially independent of the glass powder used and hence independent of the pore size of the sintered parts. Significantly lower values are found for the flexural strength of porous filters made from glass 3 and this is presumably due to inhomogeneities / cracks in the prepared specimen.

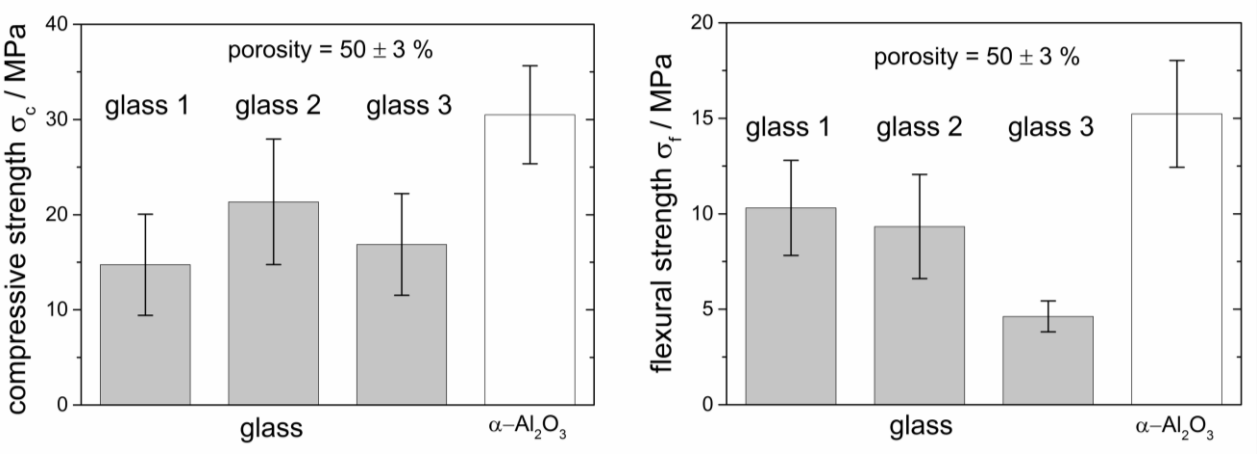

Fig. 28: Compressive strength σ_c and flexural strength σ_f of porous glass samples, compared with porous ceramic samples. All manufactured via capillary suspension processing. *Reproduced with permission from Elsevier.*

The mechanical strength of our porous glass samples is close to that of ceramic Al_2O_3 parts, manufactured via the same processing route and with similar porosity. It should be noted, that the mechanical strength of the dense ceramic matrix material is nearly an order of magnitude higher than that of glass. Dense α-Al_2O_3 has a compressive strength of about 4300 MPa and a flexural strength of 400 MPa [103], while the values of dense glass are only 800 MPa [104] and about 45 - 105 MPa (heavily dependent on surface quality). Flexural strength data for the used glass is provided from manufacturer (SCHOTT AG, Mainz, Germany).

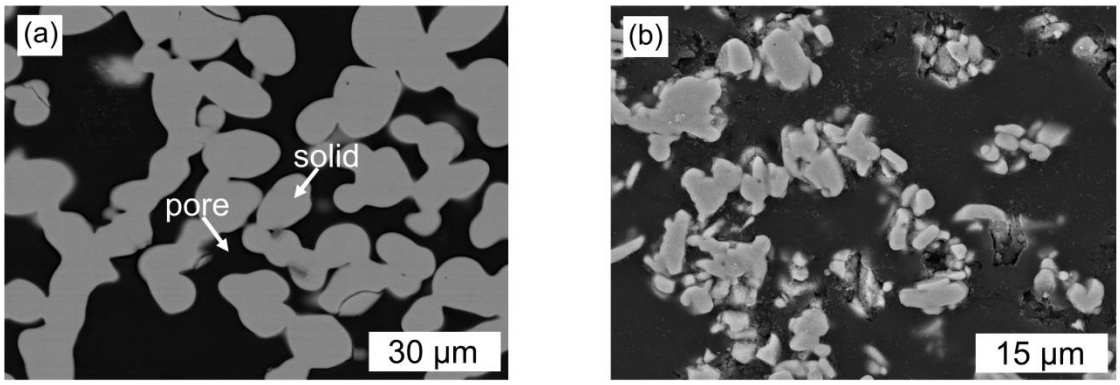

Fig. 29: SEM crosscut images of (a) a sintered glass sample (glass 1) and (b) a sintered ceramic sample, consisting of α-Al_2O_3. Solid particles appear light gray and pores as black. *Reproduced with permission from Elsevier.*

SEM images of porous parts made from glass and ceramics are shown in Fig. 29. These images reveal a strong difference in pore circularity and pore roughness. While the glass sample shows

smooth sinter necks with a high pore circularity, the ceramic Al_2O_3 sample has a rough and edged pore structure. This structure leads to a higher notch effect under load and results in a reduced mechanical strength. Thus despite the huge difference in the mechanical strength of the pure matrix material the corresponding values for the sintered porous parts from glass and ceramics are quite similar.

Gibson & Ashby [29] have developed a model describing the effect of open porosity on the mechanical strength and failure of cellular materials. The relative compressive strength of brittle porous materials, i.e. the compressive strength of the porous part σ_c normalized with the flexural strength of the dense material $\sigma_{f,0}$, is related to their open porosity ε as follows:

$$\frac{\sigma_c}{\sigma_{f,0}} = B_o\,(1-\varepsilon)^z \qquad (9)$$

The parameter z depends on the mode of failure. The exponent z = 3/2 was found to capture the behavior of brittle fracturing ceramic materials. B_0 is an empirical prefactor and the mechanical strength of a large variety of brittle cellular materials is described by Eq. (9) using B_0 = 0.2 [29]. Gauckler and coworkers [10] proved the Gibson & Ashby model to fit the experimental results for a large set of data on ceramic filters covering a wide porosity range selecting B_0 = 0.2 as prefactor in Eq. (9). Dittmann et al. showed that the mechanical strength of porous ceramic parts made from capillary suspensions is fairly well described by Eq. (9) with a prefactor B_0 = 0.2 but the dependence of mechanical strength on ε is somewhat stronger than derived by Gibson & Ashby [20].

Fig. 30 displays the relative compressive strength of glass and ceramic parts made from capillary suspensions for a broad range of relative density 1-ε. The relative compressive strength of the glass samples at a given porosity is significantly higher than that of the sintered ceramic parts. Fitting our glass data with the Gibson & Ashby model results in an empirical prefactor B_0 = 0.8 significantly higher than the value found for ceramic materials as mentioned above [22]. We attribute this improved strength to the rounder sinter necks in the glass samples which lead to a reduction of stress peaks in the porous material. Consequently the relative compressive strength increases drastically as already suggested based on SEM images shown in Fig. 29. Similar as previously reported by Dittmann et al. [16] we also find a slightly stronger dependence of relative compressive strength on porosity than suggested by Gibson & Ashby [19].

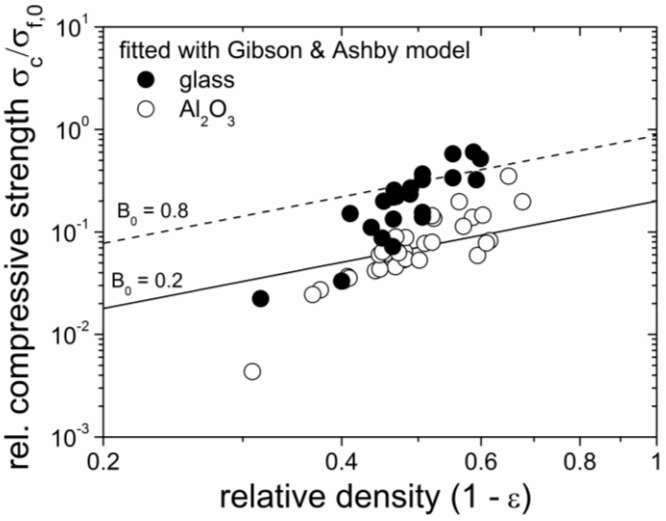

Fig. 30: Relative compressive strength of sintered samples of glass and α-Al_2O_3 as a function of the relative density 1-ε. The Gibson & Ashby model shows good agreement with the sintered capillary suspensions. Empirical prefactors: glass: B_0 = 0.8, Al_2O_3: B_0 = 0.2. Assumptions for the matrix flexural strength $\sigma_{f,0}$: Al_2O_3: 400 MPa, glass: 75 MPa [16]. *Reproduced with permission from Elsevier.*

4.3.4 Permeability

The permeability of a filter medium characterizes the mobility of a fluid in a porous structure. It is a function of the pore structure (porosity, pore size distribution, pore shape, turtuosity, etc.) and is generally independent of the test medium [105]. According to Darcy's law the permeability of a porous medium can be related to its porosity and pore size as follows [44,45]:

$$k_{g/l} = \varepsilon \frac{{x_{pore,av}}^2}{32\,T} \qquad (10)$$

Where T > 1 is the tortuosity factor describing the crookedness of a given pore structure; for straight cylindrical tubes T = 1. Fig. 31 shows the dependence of the liquid permeability k_l and the gas permeability k_g on the average pore size $x_{pore,av}$ of the tested filters from glass and Al_2O_3, at a constant open porosity ε = 50 ± 3 %. As expected, the permeability increases strongly with increasing pore size. Fitting Eq. (10) to the experimental liquid permeability data results in T = 34 for the filters made from glass capillary suspensions and T = 50 for the corresponding Al_2O_3 filters. Since the manufacturing process is the same for both types of filters we assume that the structure and its geometric tortuosity are similar but within the framework of this model the higher smoothness and circularity of the glass corresponds to a lower apparent tortuosity.

Liquid and gas permeability values are found to be similar for filters with pore diameter $x_{pore,av}$ > 10 µm. For lower pore sizes liquid permeability is significantly lower than the gas

permeability, at the lowest investigated pore size k_g is about an order of magnitude higher than k_l. For glass filters this effect is even more pronounced than for the ceramic filters and results in a weaker dependence of gas permeability on pore size than predicted by Darcy's law. Fig. 31b clearly confirms that gas permeability k_g for ceramic filters is well described by Eq. (10), whereas k_g scales with $x_{pore,av}^{1.3}$ for the glass filters. These differences between liquid and gas permeability might be attributed to the slip effect that can occur for gas flow through porous media with pore sizes on the length scale of the mean free path of the test gas. In particular at the necks between the pores additional Knudsen diffusion can get relevant and the so called Klinkenberg effect may occur finally leading to an increase of gas permeability k_g [105–107].

Finally, for pore diameters $x_{pore,av}$ < 10 µm the gas permeability is significantly higher for the glass filters than for the ceramic samples, e.g. for $x_{pore,av}$ = 4 µm the extrapolated gas permeability value for Al_2O_3 filters is four times lower than for the corresponding glass samples, for the liquid permeability the filters of the two materials differ about a factor of two. The higher circularity and smoothness of the pores in the glass samples obviously is especially relevant at low average pore size.

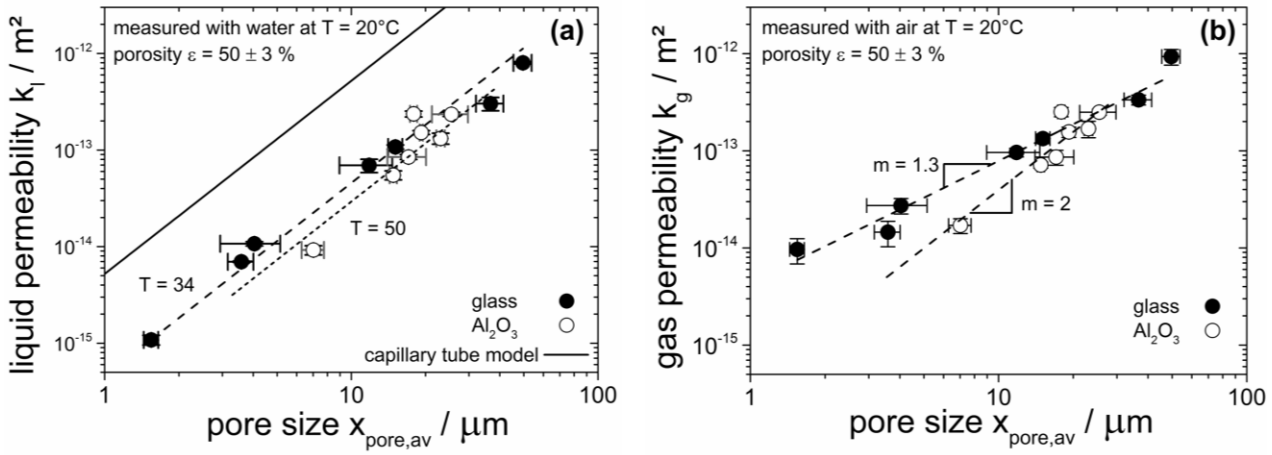

Fig. 31: (a) Liquid permeability k_l and (b) gas permeability k_g as a function of average pore size $x_{pore,av}$ of the filters. The solid line in (a) corresponds to the permeability of a filter consisting of straight circular tubes (T=1) with the same porosity. *Reproduced with permission from Elsevier.*

4.3.5 Comparison with Commercial Products

We see strong differences comparing the microstructure, mechanical strength and permeability of capillary suspension based filters with readily available commercial filtration products, both consisting of glass with nominal pore sizes in the same range (Table 4). Fig. 32 shows SEM crosscut images of the pore structure of two samples we will survey more intensively. The porosity of the commercial product DURAN P5 is ε = 29 ± 1 % whereas the corresponding value

for the capillary suspension based product is almost twice as high (ε = 50 ± 2 %). The commercial product shows an edged pore structure with strong inhomogeneities including some very large pores. In contrast the capillary suspension based product exhibits a very uniform pore structure. The inhomogeneous pore structure of the commercial product results in a broad pore size distribution (Fig. 33) and the average pore size is about 6 times higher than the nominal value provided by the manufacturer. The average pore size of the commercial product is $x_{pore,av}$ = 9.0 ± 0.3 µm, for the capillary suspension based product $x_{pore,av}$ = 1.5 ± 0.1 µm is found.

Table 4: Pore size data of commercial and capillary suspension product.

product	**maximum pore size / µm (acc. to manufacturer)**	**average pore size $x_{pore,av}$ / µm (from image analysis)**
commercial (DURAN, P5)	1.0 – 1.6	9.0 ± 0.3
capillary suspension	-	1.5 ± 0.1

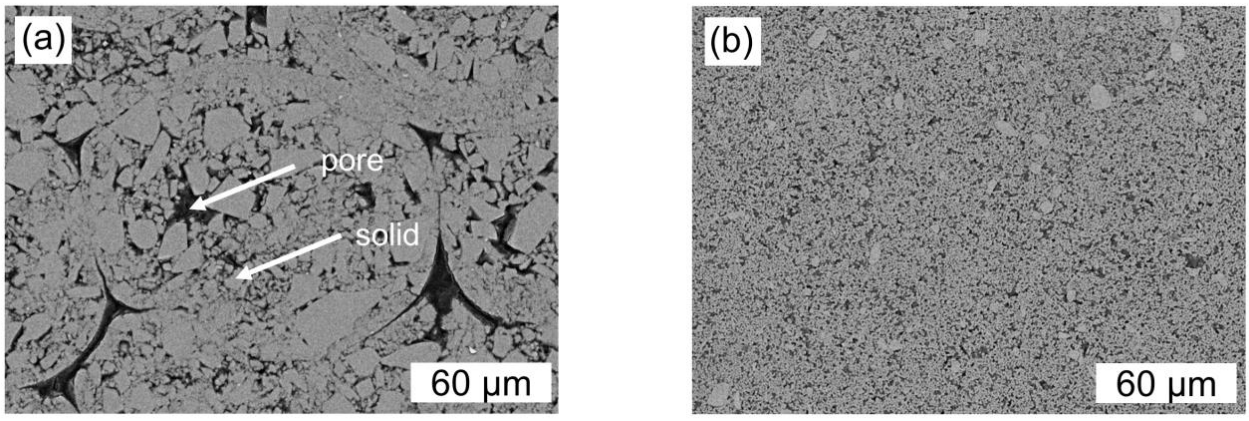

Fig. 32: SEM crosscut images of (a) commercial product (DURAN, P5): porosity ε = ~29 %, average pore size: $x_{pore,av}$ = 9.0 ± 0.3 µm; (b) capillary suspension product: ε = ~50 %, average pore size: $x_{pore,av}$ = 1.5 ± 0.1 µm. Solid particles appear light gray and pores as black. *Reproduced with permission from Elsevier.*

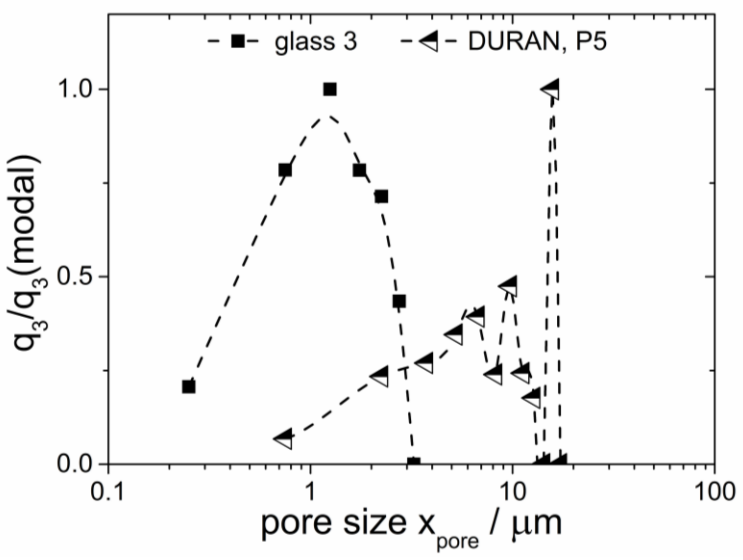

Fig. 33: Normalized differential pore size distribution q_3/q_3(modal) for sintered parts based on capillary suspensions, consisting of glass 3 (ε = ~50 %) and the commercial product (DURAN P5, ε = ~29 %). Pore size distributions determined from image analysis. *Reproduced with permission from Elsevier.*

Fig. 34a shows the striking result that both samples exhibit essentially the same compressive strength despite of the much higher porosity of the capillary suspension based product. The large pores and sharp edges present in the commercial product are supposed to result in a strong notch effect and local stress peaks responsible for the failure of the commercial product.

We also investigated the liquid permeability of commercial and capillary suspension based products. Corresponding results for a series of capillary suspension based filters and two different commercial products are shown in Fig. 34b. Dividing liquid permeability k_l by the porosity ε accounts for the influence of the different product porosities. Especially the commercial product with $x_{pore,av}$ = 9.0 ± 0.3 µm exhibits a much lower reduced liquid permeability than corresponding capillary suspension based filters. This is particularly surprising since this material includes a fraction of very large pores (s. Fig. 32a) supposed to act as by-pass for the small pores (streaming pores). Presumably the higher circularity and smoothness of the pores as well as the high structural homogeneity of the capillary suspension based filters are decisive for their higher permeability.

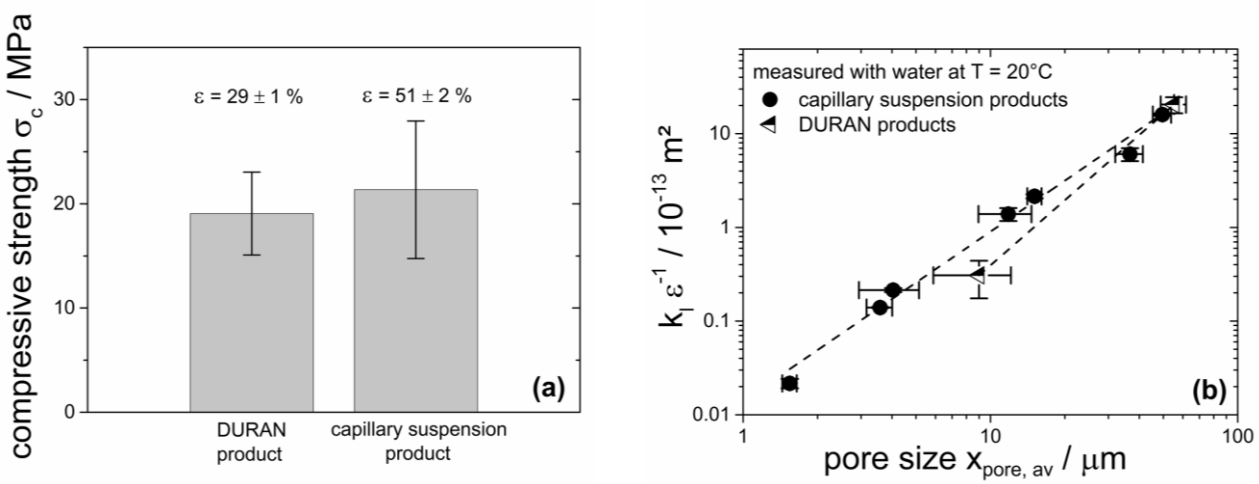

Fig. 34: (a) Comparison of compressive strength of a commercial product (DURAN) and a capillary suspension glass product. (b) Liquid permeability k_l normalized with porosity ε of capillary suspension glass products (ε = 50 ± 3 %) compared with commercial products (DURAN) (ε = 29 ± 1 %). Both consisting of glass. *Reproduced with permission from Elsevier.*

4.4 Conclusions

The capillary suspension concept enables us to manufacture porous sintered glass filters with an open porosity of about 50% and average pore sizes $x_{pore,av}$ between 1 – 50 µm. The microstructure of the sintered glass parts is homogeneous with narrow, almost monomodal pore size distributions. Pores are much smoother and exhibit higher circularity than that of similarly processed ceramic filters.

The mechanical strength of the sintered glass parts is almost as high as that of Al_2O_3 parts with similar porosity, despite of the much lower strength of the dense matrix material. In other words the relative compressive strength $\sigma_c/\sigma_{f,0}$ of the glass parts is much higher than that of the ceramic filters. We trace this back to the differences in pore shape: The edged pore structure of the ceramic material leads to a higher notch effect and accordingly to a lower relative mechanical strength of the porous ceramic parts. Absolute values of the compressive strength agree well with the Gibson & Ashby model for brittle materials but the prefactor B_0 is higher for the glass filters than for porous ceramic materials. Moreover, the variation of the mechanical strength with porosity is slightly more pronounced than predicted by the exponent z = 3/2 theoretically deduced by Gibson and Ashby and experimentally confirmed for a broad variety of ceramic materials.

Glass filters based on capillary suspensions exhibit a higher gas and liquid permeability than corresponding ceramic filters. This is attributed to a higher pore smoothness and circularity in the glass parts. In accordance with Darcy's law liquid permeability varies as $x^2_{pore,av}$ for both types of filters, but apparent tortuosity is higher for the ceramic than for the glass filters. The high

gas permeability found for the glass filters at low pores sizes is presumably due to slip in the necks between the pores with characteristic dimensions close to the mean free path of the gas and eventually results in a weaker dependence of k_g on pore size.

Finally, we compared glass filters manufactured according to our new processing route and commercial glass filters with respect to pore structure, mechanical strength and permeability. The commercial products have a broad pore size distribution with an inhomogeneous pore structure including a fraction of large holes and sharp edged pores. Although the capillary suspension based products exhibit porosities nearly twice as high as the commercial products, their mechanical strength is essentially equal. The high strength of capillary suspension based products is attributed to their uniform structure with smooth and highly circular pore shape contrasted by the investigated commercial product. This unique structural features are also decisive for the high permeability especially at low $x_{pore,av}$ found for the capillary suspension based filters.

4.5 Acknowledgements

This study was financially supported by the Bundesministerium für Wirtschaft und Energie (project no. 03SHWB011) and Schott AG. Further thanks are given to Thomas Lebe for the work at the SEM-microscope as well as Daniel Müller and Monika Wolf for contributing to the permeability measurements.

4 Highly porous materials with unique mechanical properties

Full title: Highly porous materials with unique mechanical properties from smart capillary suspensions

Authors: Jens Dittmann, Johannes Maurath, Boris Bitsch, Norbert Willenbacher

Status: published

Bibliographic data: Advanced Materials 28 (2016) 1689-1696
10.1002/adma.201504910

Abstract

Smart capillary suspensions are used to fabricate macroporous solids with unique features regarding porosity and mechanical strength from a wide range of materials, including carbon layers and polyethylene membranes, even if sintering or high-temperature treatment is not feasible. High-strength porous ceramics are obtained, tailoring neck and pore shape via controlled deposition of fine particles at the sintering necks.

4.1 Article

Capillary suspensions are three-phase fluids comprising a solid and two immiscible liquid phases. Addition of a small fraction of the secondary liquid phase to a suspension of particles dispersed in the so-called primary or bulk phase leads to the formation of a strong sample spanning particle network, even at low particle loadings. This particle network gains its strength from the capillary forces inferred from the added secondary liquid no matter whether it wets the particles better or worse than the primary liquid [11,29]. This attractive force is typically orders of magnitude stronger than the ubiquitous van der Waals attraction. Accordingly, capillary suspensions exhibit a paste-like texture and a strongly shear thinning flow behavior. They are highly resistant to sedimentation and flow properties can be tuned in a wide range according to different processing or application demands. Even the flow behavior of methane hydrates turned out to be strongly affected by capillary bridging [53]. A broad range of innovative products

including novel food formulations, such as heat stable and low calorie chocolate spreads [13], capillary suspension based foams [54,55] or pastes for printed electronics, e.g. lithium-ion battery electrodes or front side metallization of solar cells with unique shape accuracy and surface uniformity have been developed [15]. The capillary suspension concept has also been used to control structure formation in particle-laden polymer blends [56] and to assemble metals and nanoparticles into novel nanocomposite superstructures [57].

Beyond that capillary suspensions can be utilized as precursors for highly porous sintering materials to be used as light weight construction materials, filters or membranes [10,16,40]. The easiest and most straight forward route to produce porous materials is the partial sintering of a powder compact but the resulting porosities ε are below 50%. Various other methods like sacrificial templating, replica techniques or using particle stabilized foams [108] and Pickering emulsions have been developed to produce macroporous sintering materials [17,22,109]. But especially, the parameter range $\varepsilon > 50\%$ and $d_p < 10$ µm, with d_p is the pore diameter, is hardly accessible using these conventional techniques. The strong particle network in capillary suspensions does not collapse and largely retains its structure even upon removal of the bulk fluid phase ("debinding"). Resulting highly porous green bodies can be sintered and this versatile processing route based on well-established unit operations yields strong solid materials with open porosities ε up to 80% at pore sizes d_p between 0.5 - 50 µm as has been demonstrated for α-Al_2O_3 ceramics [10,16]. Recently, glass filters with highly uniform pore structure resulting in a mechanical strength similar to ceramic filters (at given ε and d_p) and gas permeability exceeding that of ceramic or commercial glass filters have been manufactured [40]. Essentially every vitrifiable powder can be easily turned into a highly porous solid using the capillary suspension concept. Examples using metal, polymer, glass and ceramic powders are shown in the supporting information demonstrating the broad applicability of this versatile, low-cost processing route (Fig. S1, Supporting Information). Using this approach, porosity and pore size are controlled by the particle size, solid content, amount of secondary liquid phase and sintering conditions. Lower particle loading typically results in an increased porosity and lower particle size corresponds to a lower pore size. For a constant particle loading at a constant particle size, increasing the amount of secondary liquid phase leads to a coarsening of the structure, i.e. an increase of pore size. Sintering conditions have to be chosen such that neck growth is sufficient to provide the desired mechanical strength and porosity [10,110].

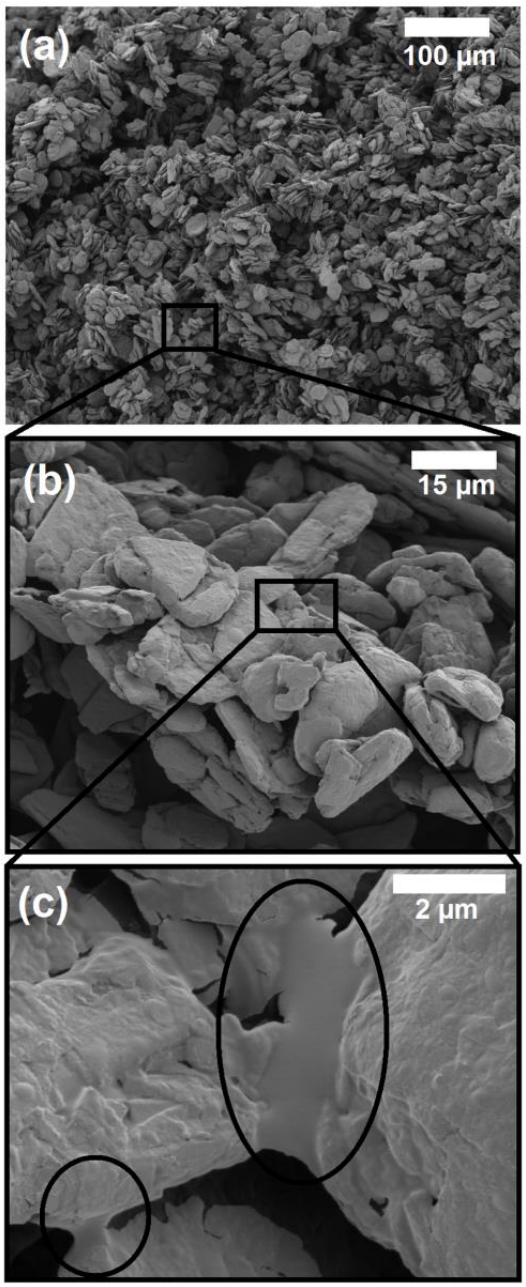

Fig. 35: SEM images of the fracture surface of capillary suspension based, porous graphite samples with different magnification (as indicated by the scale bars). Reactive resin added as secondary fluid forms polymer bridges between particles providing mechanical strength to the sample. These bridges are highlighted by black circles (c). *Reproduced with permission from Wiley-VCH Verlag GmbH & Co. KGaA.*

Here we focus on advanced capillary suspension based concepts for manufacturing highly porous materials with unique structural and mechanical features. A targeted choice of the secondary fluid allows for a specific shaping of the particle contact regions resulting in exceptional mechanical strength. We use graphite, polymer and ceramic model systems to demonstrate the versatility and broad applicability of this concept. Resilient, highly porous solids

from graphite which cannot be sintered are obtained from capillary suspensions using reactive resins as secondary fluid. Sintering activity during manufacturing of porous polymeric materials can be drastically increased compared to conventional partial sintering of powders using capillary suspensions with an appropriate solvent or swelling agent / plasticizer as secondary fluid. Finally, the mechanical strength of porous ceramics can be strongly improved using the secondary fluid as carrier transporting appropriate active ingredients to the particle contact zones. Thus sintering of the neck regions and pore shape can be specifically controlled and the mechanical strength of the resulting porous sintered parts can be distinctly increased.

Micrometer-sized, flaky graphite particles have been suspended in glycerol at a particle volume fraction of 20 vol% and different amounts of reactive epoxy resin were added as secondary fluid. The observed tenfold increase in low shear viscosity upon resin addition indicates the formation of a strong particle network within the liquid suspension. The resin was cured at ambient conditions while still surrounded by the bulk fluid. After removing the latter by solvent extraction a durable, load bearing porous solid was obtained for samples including 8 vol% and 12 vol% of resin (corresponding to 24 vol% and 37 vol% resin in the dry membrane) without any sintering. Porosities were in the range $60\% < \varepsilon < 75\%$, pore size about 15 µm (cf. pore size distribution in Fig. S2a, Supporting Information) and the compressive strength of these membranes was on the order of 0.1 – 1 MPa. Fig. 35 indicates that this is achieved since the resin is located at the particle contacts resulting in a “point-welding” of the network structure created in the wet state.

Numerous different approaches to fabricate porous carbon membranes with a broad range of different porosity and/or pore size have been described in the literature [111,112]. Here, we restrict ourselves to open, macroporous foams or membranes. In [111,112] several examples of macroporous carbon foams including commercial products are listed with porosities around 75% and compressive strength of about 1 MPa but in all these cases the pore size is above 100 µm, i.e. they are similar in mechanical strength but different in microstructure. Pekala and Hopper [113] report about highly porous carbon foams with porosities between 80% and 95% and average pore size of 8 µm. However, the mechanical strength is extremely low (≈ 100 Pa) due to structural defects and heterogeneities making mechanical test almost impossible. Recently, carbon foams were prepared with pore sizes between 1 µm and 10 µm but porosity was low and pores were mostly closed as indicated by the provided micrographs [114]. In conclusion, our new approach enables fabrication of previously not accessible self-supporting graphite membranes with open porosities in the range of 70% and median pore size ≈ 15 µm exhibiting mechanical strength close to what has been observed only for samples with much larger pores. Such self-supporting carbon layers may find application as light-weight construction material, in super capacitors or as gas diffusion electrodes in fuel cells or Li-air batteries [84–87]. But more

importantly this concept is not restricted to graphite, it may also be applied to various other materials which cannot be sintered at all or in cases where high sintering temperatures have to be avoided. Reactive resins with very different reaction temperature and final crosslink density are readily available. Moreover, appropriate monomers might be used as secondary fluid to be polymerized at the contact areas between particles in order to provide thermoplastic links between solid particles. Further research is warranted to verify whether this concept provides a versatile processing route to tune flexibility and toughness of such highly porous materials.

Often, so-called sintering aids are used to increase the strength and density of sintered parts at reduced sintering temperature. Usually, such active ingredients are introduced as specific coatings or additives facilitating the diffusion processes between particles, thus accelerating the sintering process of the bulk material [115–117]. Here we use the secondary fluid of a capillary suspension as a sintering aid. Macroporous polymer membranes have been made suspending micrometer-sized ultrahigh molecular weight polyethylene (UHMWPE) particles in glycerol and using m-xylene or paraffin oil as secondary fluid. Addition of these secondary fluids results in a strong increase in yield stress (Fig. S3a, Supporting Information) indicating the formation of a capillary suspension with a strong particle network. For the sample with paraffin oil as secondary fluid the capillary bridges could be directly visualized using fluorescence microscopy (Fig. S3b, Supporting Information). However, at temperatures above 110° C these organic solvents act as swelling agents/solvents [118]. Samples with different amount of secondary fluid were sintered at similar conditions (135°C, 2 hours) in the presence of glycerol thus preventing m-xylene from evaporation during this processing step and all liquid ingredients were removed subsequently via solvent extraction. The open porosity of the resulting dry membranes decreased from $\varepsilon = 77 \pm 3\%$ without secondary fluid to $\varepsilon = 62 \pm 3$ % when 4% m-xylene was added (Fig. 36a). Median Pore diameter slightly decreased from 30 μm for the membrane made from the pure suspension to 25 μm for the membrane made from the capillary suspension including 4 vol% m-xylene. The narrow, monomodal pore size distribution is shown in Fig. S2b (Supporting Information). When the sintering temperature is reached, the added secondary fluid starts to penetrate into the particles, this increases the mobility/diffusivity of the polymer chains in particular at the particle contact zones where swelling commences and thus locally increases the sintering activity of the polyethylene without temperature increase. Dissolution of capillary bridges and diffusion of secondary liquid into the polymer particles takes place simultaneously with sintering, i.e. the inter-diffusion of polymer chains in the particle contact zones. The increased sintering activity also shows up in the faster decrease in porosity over sintering time when capillary suspensions with m-xylene as secondary fluid are compared to a pure suspension of UHMWPE (Fig. 36b). Sintering without secondary fluid is still incomplete under

these conditions (Fig. 36c), whereas the swelling agent at the particle contacts induces in a smooth pore structure with well-developed sintering bridges (Fig. 36d). Evaporation of m-xylene at elevated temperature seems not to be an issue, the difference between membranes made with and without secondary fluid is striking and the membranes made with m-xylene and the non-evaporating paraffin oil exhibit similar properties.

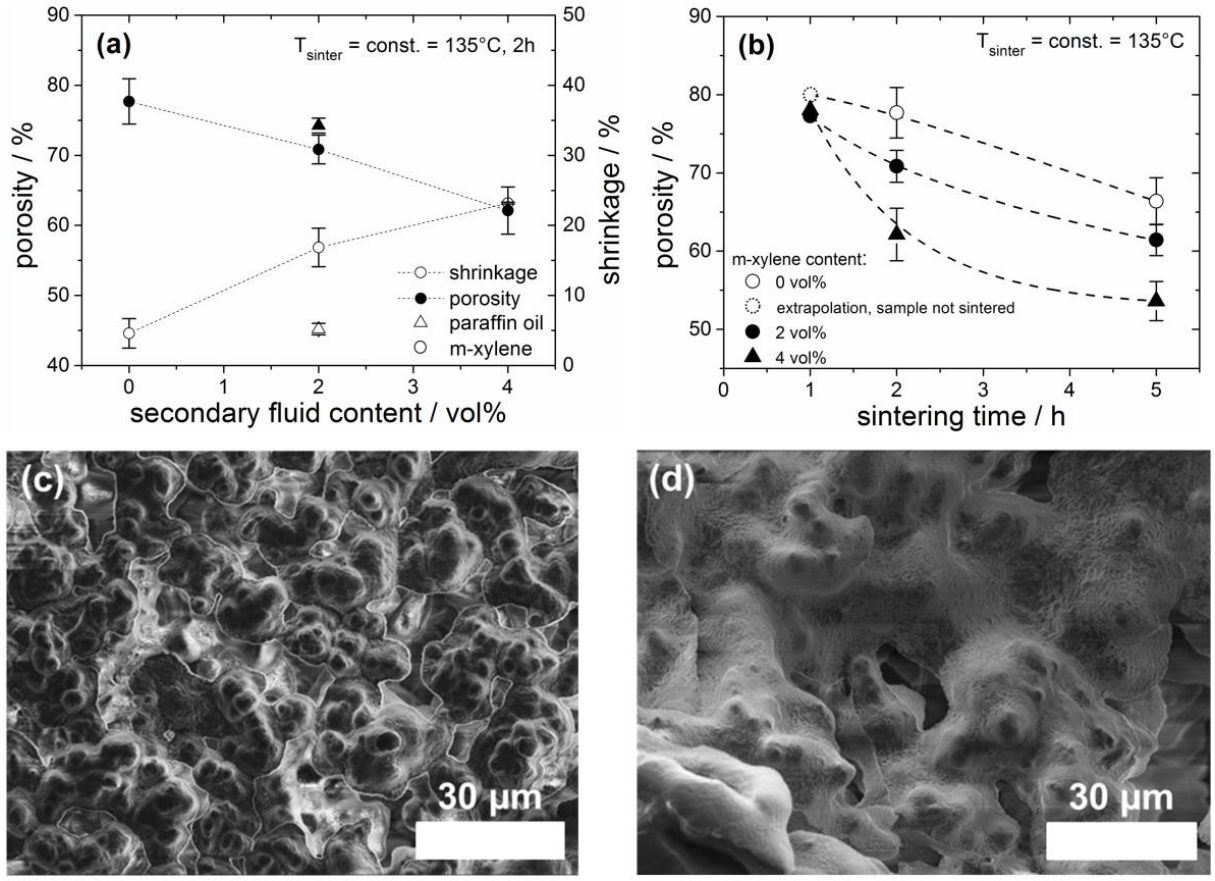

Fig. 36: (a) Porosity and shrinkage of sintered parts made from UHMWPE suspensions as a function of secondary fluid content. (b) Porosity of sintered UHMWPE suspensions vs. sintering time at different m-xylene content. In (a) and (b) glycerol was used as bulk and m-xylene or paraffin oil as secondary liquid phase. SEM images of the internal structure of sintered parts made from the (c) pure suspension, (d) capillary suspension (secondary fluid phase: m-xylene ϕ_{sec} = 2 vol%). Cross sections were obtained cleaving the membranes with a sharp scalpel. Sintering conditions: T_{sinter} = 135°C, 2h. *Reproduced with permission from Wiley-VCH Verlag GmbH & Co. KGaA.*

The sample made from the pure suspension is not self-supporting whereas the samples sintered in the presence of a swelling agent provide durable, flexible membranes with Young's moduli between 2 MPa and 6 MPa. Commercial UHMWPE membranes are obtained from sintering compacted powder at temperatures above 180° C resulting in porosities typically well below 50% [119,120]. High porosity foams were made from UHMWPE gels exposed to extensional flow but the samples did not appear in bulk form and mechanical strength could not be

determined [121]. So the smart capillary suspension concept not only provides a new processing route but also gives access to UHMWPE membranes with unique properties in terms of porosity and mechanical strength. UHMWPE is a nontoxic material with a high chemical stability and a high abrasion resistance and such highly porous membranes may be used as separators in Lithium-Ion batteries [122]. Further applications for highly porous UHMWPE may be for medical implants allowing for a good tissue ingrowth [123]. Beyond that, the proposed concept may be applied to other polymeric systems as well.

Utilizing the secondary fluid of a capillary suspension to deposit small particles specifically at the contact regions of the larger particles is another means to increases the sintering activity. But more importantly this approach can be used to increase the mechanical strength of highly porous materials substantially. For a given chemical composition of the solid material the mechanical strength of macroporous sintered parts is mainly controlled by the porosity and strongly decreases with increasing pore volume fraction [19,124]. At given porosity parts made from capillary suspensions exhibit similar properties as those from other processing routes [16]. Increasing the mechanical strength especially at high porosities is still a challenge and would open up new fields of application. Based on the MSA-model (Minimum Solid Area) of Rice and Knudsen it has been suggested to use a bimodal particle size distribution in combination with the partial sintering method to improve mechanical strength of porous sintering materials [125,126]. The idea is to place the fine powder fraction at the contact areas of the coarse particles thus achieving a better neck growth and hence better mechanical stability. The fine powder fraction may either be conspecific to the coarse powder fraction or may work as a doping agent [127,128]. In conventional processing (limited to $\varepsilon < 50$ %) the mechanical strength could not be improved so far, since the fine powder fraction could not be preferentially deposited at the contact areas between large particles. Instead, it was distributed uniformly resulting in an increased densification of the powder compact during the sintering procedure or even partially agglomerated because of insufficient processing [127]. However, if the fraction of fine particles or another active ingredient is dispersed in the secondary liquid phase of a capillary suspension, it will be deposited in the contact regions of the large particles which create the sample-spanning network. The corresponding processing scheme is shown in Fig. 37a focusing on the case where the secondary liquid phase preferentially wets both powder fractions, i.e. the three phase contact angle is below 90° for both particle species. In step (I) a pure and homogeneous suspension of the coarse powder is prepared. Then in step (II) the secondary liquid phase including the fine particles (or other additives) is added to the pure suspension, drops of this liquid phase are formed and deposited at the contact regions between the particles creating a strong uniform particle network. Subsequent shaping, e.g. extrusion, injection molding or screen

printing (step III) followed by careful debinding and sintering of the precursor leads to a sintered part with a homogeneous pore size distribution and a high open porosity (step IV). Alternatively, a pure suspension of a bimodal powder can be prepared in step (I), then in step (II), when the small secondary liquid droplets are formed, only the small particles will be selectively captured in the droplets and then again be deposited at the interfacial regions between the large particles. The result of such a self-assembling process, with the secondary liquid phase working as a specific carrier for small particles, is shown in Fig. 37b. A bimodal mixture of polyvinylchloride (PVC) particles was suspended in water and upon addition of diisononylphtalate (DINP) the small particle fraction is preferentially deposited at the interfacial regions between the large particles. This does not happen in a pure suspension of a bimodal PVC powder, neither in water nor in DINP. This concept leads to a strong increase of the particle coordination number and sintering can then be done at reduced energy or processing cost. But even more importantly, the circularity of the pores and the MSA of the sintering necks is increased finally resulting in an improved mechanical strength. Moreover, the chemical composition of the fine particle fraction can be selected appropriately such that a composite material is created in the sintering regions further increasing mechanical strength. The potential of this new concept are demonstrated for ceramic materials using α-Al_2O_3 as model system. The coarse powder fraction has a median particle size of 5.76 µm, paraffin oil was used as bulk phase and an aqueous sucrose solution as secondary liquid phase [10,16]. Two different fine powder fractions were used, both about one order of magnitude smaller than the coarse particles: α-Al_2O_3 with a median particle diameter of 0.67 µm was used as conspecific fine powder fraction, tetragonal stabilized (3 mol% Y_2O_3) t-ZrO_2 with a median particle diameter of 0.7 µm was used to modify the sintering necks. Both fine particle fractions are preferentially wetted by the aqueous phase and the corresponding three-phase wetting angles are 66° and 83°, respectively. ZrO_2 was chosen as fine particle fraction since in dense systems doping Al_2O_3 with t-ZrO_2 results in a composite material called zirconium toughened alumina (ZTA-ceramic), characterized by improved mechanical properties like increased strength, fracture resistance and toughness [129,130].

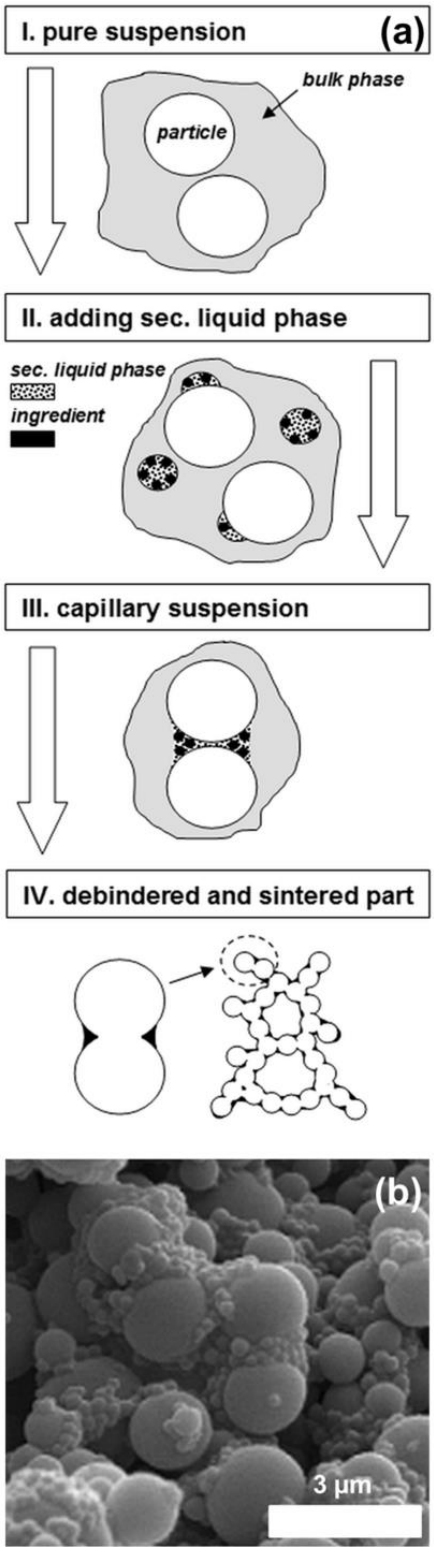

Fig. 37: (a) Principle processing scheme: using capillary suspensions and bimodal particle mixtures for tailoring the mechanical strength of highly porous sintered parts. The secondary liquid phase works as a specific carrier for the active ingredient added as fine powder fraction. (b) Dried and slightly sintered capillary suspension of PVC powder with bimodal particle size distribution with water as bulk phase and diisononylphthalate (DINP) as secondary liquid phase. Preparation: tempering for three hours at 90°C. *Reproduced with permission from Wiley-VCH Verlag GmbH & Co. KGaA.*

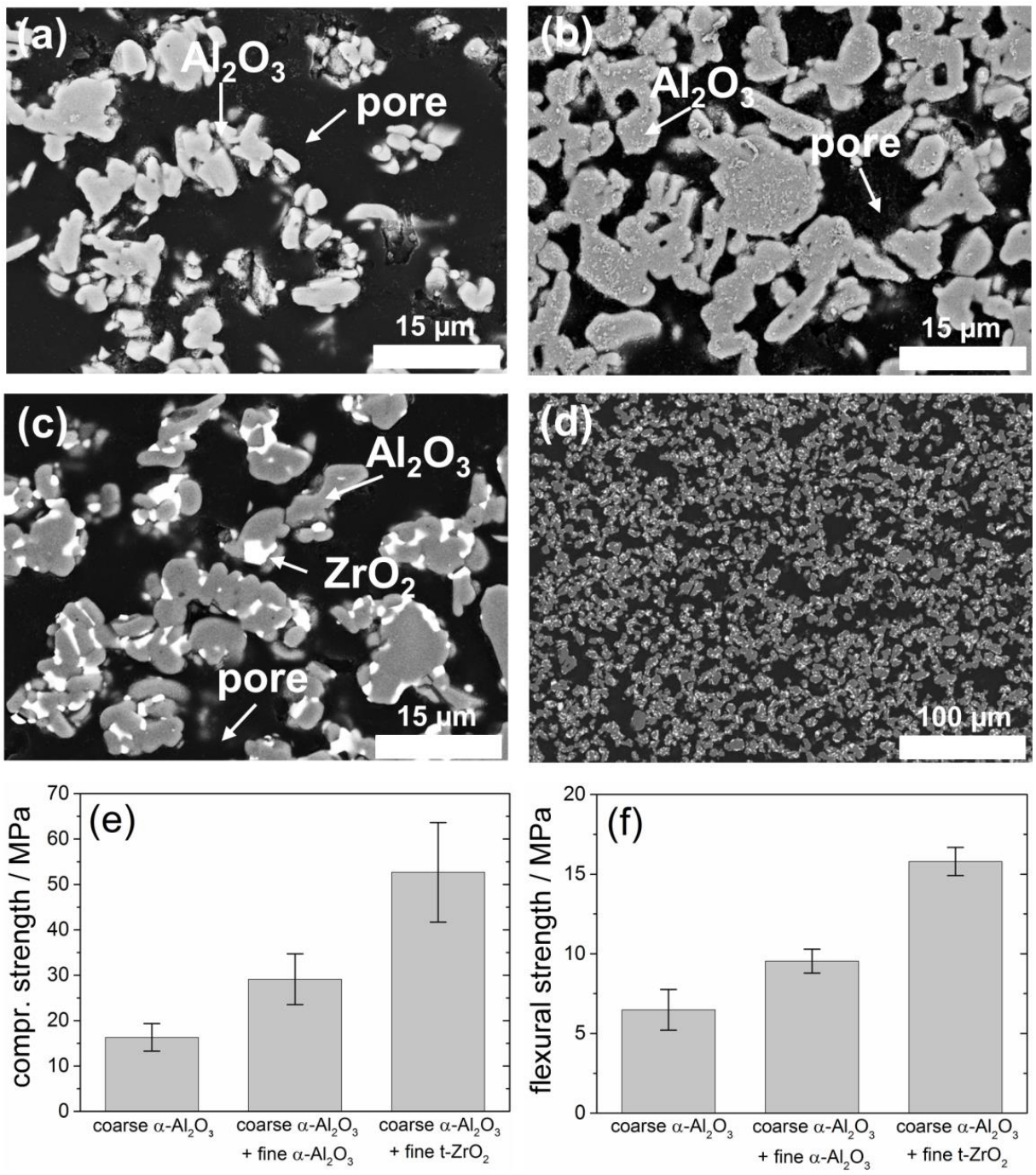

Fig. 38: SEM-BSE cross-cut images and mechanical properties of sintered capillary suspensions made from different powder compositions at a constant amount of secondary liquid phase (2.5 vol%). (a) coarse monomodal α-Al_2O_3 powder, total solids 25 vol.%, sintered at 1650°C for 2h, (b) powder mixture of coarse and fine α-Al_2O_3, total solids fraction 20 vol%, fine particle fraction 20% relative to total solids, sintered at 1550°C for 2h, (c) powder mixture of α-Al_2O_3 (coarse) and t-ZrO_2 (fine), total solids fraction 15 vol%, fine particle fraction 10% relative to total solids, sintered at 1650°C for 2h, due to the difference in electron density t-ZrO_2 appears white and α-Al_2O_3 appears grey in these electron micrographs, (d) overview image of the same α-Al_2O_3 / t-ZrO_2 sample, e) compressive strength and (f) flexural strength of corresponding samples with $\varepsilon \approx 55\%$. Error bars are the standard deviation calculated from at least three measurements. Note, in the case of the con-specific α-Al_2O_3 mixture with 20% fine particle fraction and 2.5% added secondary fluid the loading of fine particles in the secondary liquid droplets is close to maximum packing. *Reproduced with permission from Wiley-VCH Verlag GmbH & Co. KGaA.*

Fig. 38 shows SEM-BSE cross-cut images of sintered parts made from capillary suspensions constant with constant amount of secondary liquid phase but different amount and composition of powder mixtures (see figure caption) chosen to result in a constant porosity of ε = 55%. The monomodal coarse powder preparation sintered for 2 h at 1650 °C shows sharp and rough-edged pores with a small MSA (Fig. 38). The conspecific α-Al_2O_3 powder mixture with 25 vol% fine particle fraction sintered for 2 h at 1550 °C results in a structure with an increased MSA (Fig. 38b). Obviously, this also results in a higher circularity of the pores and finally in a smoother pore geometry. This is attributed to the targeted deposition of fine particles at the contact regions between coarse particles. This hypothesis is directly confirmed by the SEM-BSE images obtained for the system where t-ZrO_2 was used as fine powder fraction (Fig. 38c). Due to the material contrast between t-ZrO_2 and α-Al_2O_3 it is directly visible that the fine particles are selectively deposited at the contact areas between the large particles and that this leads to an improved circularity of the pores. The overview image in Fig. 38d shows, that the t-ZrO_2 is uniformly distributed throughout the sample. In conclusion, the capillary suspension is a stable precursor prohibiting phase separation between different materials and allowing for a targeted design of the sintering necks in macro porous materials.

Formation of these distinct structural features is enabled by the network in the capillary suspension and already shows up in the wet state as can be seen from Fig. S4a (Supporting Information). A capillary suspension with a monomodal particle size distribution exhibits an increase in yield stress of at least one order of magnitude, compared to the corresponding pure suspension. This is different for powder mixtures as shown here for the α-Al_2O_3 with added t-ZrO_2. In the pure suspension both particle species are homogenously distributed and contribute to the strength of the van der Waals (vdW) network but with increasing fine powder fraction the number of particle-particle contacts increases drastically and this results in the strong increase in yield stress [131,132] as shown in Fig. S4a (Supporting Information) for a fixed total volume fraction of solids. The situation changes when the capillary suspension system is considered. In this case the fine particles are deposited at the particle contact regions of the coarse powder fraction forming the network stabilized by capillary bridges. The number of particle contacts contributing to that network is given by the number of large particles which decreases as the fine powder fraction increases (at constant total solids), since the latter do not create own, new network nodes. Accordingly the yield stress also decreases and at a fine powder fraction of 20% it is only slightly higher than for the corresponding pure suspension with its large number of particle contacts controlled by vdW attraction. However, the microstructure is distinctly different and this as a strong impact on structure and mechanical strength of the corresponding sintered parts. At constant sintering conditions, an increasing amount of fine powder always leads to a

decrease in porosity of the sintered parts (Fig. S4b, Supporting Information). But this reduction in porosity is only weak, when a capillary suspension is used as precursor. In contrast, the porosity of sintered parts made from pure suspensions with a high fraction of fine particles is very low because the weak van der Waals network collapses and the bimodal particle distribution allows for a much denser packing compared to the monomodal system. Although yield stress of the pure and the capillary suspension with a fine particle fraction of 20 vol% (relative to the total solids volume) exhibit almost the same value, the porosities of the corresponding sintered parts differ strongly and only the capillary suspensions can provide high porosities $\varepsilon > 50$ %. Although the sinter activity rises when the fraction of fine powder is increased, densification of the capillary suspension system is prohibited by the self-assembled structure with the fine powder fraction located at the contact regions of the coarse particle network.

The dedicated structural features of sintering materials made from capillary suspensions with bimodal particle size distribution have a direct impact on the mechanical bulk properties of sintered parts (Fig. 38e,f). Compressive and flexural strength of such parts made from a monomodal coarse powder preparation of α-Al_2O_3 are compared to corresponding values for samples made from bimodal powder preparations with t-ZrO_2 and conspecific α-Al_2O_3 as fine powder fraction at a total open porosity of 55 %, sintering conditions were adjusted accordingly. The addition of a conspecific α-Al_2O_3 fine powder fraction leads to a rise of the mechanical strength compared to sintering the monomodal α-Al_2O_3 coarse powder, even though the sintering temperature was reduced from 1650°C to 1550°C. The flexural strength increases by a factor of about 1.5 from 6.5±1.3 MPa to 9.5±0.7 MPa and the compressive strength by about a factor of 2 from 16.3±3 MPa to 29.1±5.6 MPa. According to theory of brittle materials this is attributed to the improved MSA and the smoother sintering structure resulting from the addition of the fine powder fraction [19,124]. Moreover, using t-ZrO_2 as fine powder fraction results in an increase of flexural strength by a factor of 2.5 from 6.5±1.3 MPa to 15.8±0.9 MPa and compressive strength by a factor of almost 3.5 from 16.3±3 MPa to 52.7±11 MPa compared to the monomodal α-Al_2O_3 coarse powder preparation. This drastic increase in mechanical strength may be due to the formation of a strong ZTA composite like in dense systems, Fig. 38c indicates that most of the t-ZrO_2 is encased by α-Al_2O_3 in the sintered part. The presented examples demonstrate that the targeted deposition of a fine powder fraction on the micro-scale enabled by the capillary suspension concept is a targeted strategy for tailoring mechanical features on the macro-scale and the mechanical strength of highly porous materials can be increased in an inimitable manner. Our concept is a priori not restricted to the particular choice of fine particles investigated so far. Active ingredients forming solid solutions with α-Al_2O_3 may be suited for a further increase of mechanical strength. This warrants continuing research efforts.

In summary, we have presented an advanced capillary suspension based concept for manufacturing porous materials with exceptional mechanical strength taking advantage of a demand-oriented choice of secondary fluid. Resilient self-supporting highly porous carbon layers have been prepared using a reactive resin as secondary fluid. Polymer membranes have been made using a swelling agent as secondary fluid thus acting as sintering aid enabling membrane manufacturing at drastically lower temperature additionally resulting in membranes with unique properties in terms of porosity and mechanical strength. Highly porous ceramics with threefold mechanical strength compared to the pure reference system have been made using the secondary fluid as a carrier depositing small particles at the contact zones of the large particles in the wet state of processing. Thus sintering of the neck regions was promoted, and moreover their chemical composition and the pore shape could be specifically tailored in order to control the mechanical properties of the final porous parts.

Our new approach is ideally suited to fabricate highly porous solids from a wide range of materials, even if they cannot be sintered or treatment of elevated temperatures is not feasible. The proofs of concept demonstrated here should stimulate further research and technical developments. Besides reactive resins appropriate monomers to be polymerized in situ maybe used to tailor the strength and elasticity of porous solids. The composition of the neck regions in porous ceramics may be designed by deposition of appropriate small particles forming solid solutions with the major constituent of the ceramic scaffold thus further improving mechanical strength. Such macroporous materials with their unique mechanical strength offer distinctly advanced specifications in classical fields of application like membranes or filters, lightweight construction materials, thermal insulators or catalyst carriers but are also suited to enable innovative applications e.g. as membranes in fuel cells, electrode layers in Li-air batteries or medical implants.

4.2 Experimental Section

4.2.1 Materials and preparation of capillary suspensions

Graphite:

Flaky shaped graphite powder SLP30 ($x_{50,3}$ = 15.8 µm) was obtained from Imerys Graphite and Carbon Ltd. (Bodio, Switzerland). Glycerol was used as bulk phase. The commercial two component epoxy resin SK Resin 152 (S u. K Hock GmbH, Regen, Germany) was employed as secondary fluid. The three-phase contact angle of this resin mixture on graphite was determined to be 130° indicating that this system is in the so-called capillary state [11].

Suspensions of 20 vol% graphite particles in glycerol were prepared using a high shear dissolver at 1200 rpm for 10 min. The two component resin was premixed manually and then added to the pure suspension while stirring at 1000 rpm for 5 min. Three-phase suspensions with resin fractions of 0, 1.6, 4, 8 and 12 vol% relative to the total suspension volume were prepared, filled into aluminum molds (diameter: 39 mm, height: 5 mm), and subsequently cured at room temperature for 120 hours. Samples were removed from the mold before glycerol was extracted in an ethanol bath for 2 hours and then dried at 65°C for several hours.
Note, that capillary suspensions are obtained here even at resin contents of 8 vol% and 12 vol% corresponding to secondary fluid to solid ratios of 0.4 and 0.6. This is due to the plate-like shape of the graphite particles enabling to accommodate more secondary fluid in capillary bridges without inducing spherical agglomeration than in the case of isometric particles [39].

Ultrahigh molecular weight polyethylene (UHMWPE):

UHMWPE powder ($x_{50,3}$ = 34.3 µm) was received from Ticona GmbH (GUR 2126, Sulzbach, Germany). Glycerol (ROTIPURAN ≥ 99.5%, Carl Roth, Karlsruhe, Germany) was used as bulk phase (η = 1.48 Pas) and m-xylene (η = 0.58 Pas) and paraffin oil (η = 0.03 Pas) both supplied by Carl Roth, Karlsruhe, Germany were added as secondary phase. The three phase contact angles of the paraffin oil on UHMWPE is 43° and of m-xylene on UHMWPE is 29°, indicating that the corresponding capillary suspensions are in the pendular state [11].
Pure suspensions of 20 vol% UHMWPE (M_w = 4.5 10^6 g/mol) in glycerol were prepared using a high shear dissolver at 1200 rpm for 10 min. Then m-xylene or paraffin oil was added as secondary liquid phase at 2 vol% and 4 vol% relative to the total suspension volume. This corresponds to the concentration range in which the yield stress exhibits a maximum for isometric particles, at higher secondary fluid content spherical agglomeration sets and leads to a pronounced decrease in yield stress [16,39]. Samples were stirred for 2 min at 2000 rpm (droplet formation) and 2 min at 800 rpm (structure formation). The prepared samples were filled in aluminum molds (diameter: 39 mm, height: 5 mm). Sintering was done in a laboratory furnace at 135 °C for 2 h and subsequently liquid components were extracted in an ethanol bath. Samples with paraffin oil as secondary fluid phase were additionally washed with diethyl ether.

Polyvinylchlorid (PVC):

Bimodal PVC powder ($x_{50,3}$ = 1.88 µm, particle size distribution provided in Fig. S5) was obtained from Vinnolit GmbH & Co. KG. Water was used as bulk liquid phase and diisononylphthalate (η = 75 mPas) as secondary liquid phase (DINP, Roth, Karlsruhe, Germany).

Pure suspensions (20 vol% PVC particles in water) were prepared using a high shear dissolver at 1200 rpm for 10 min. Then 2.5 vol% DINP was added as secondary liquid phase and stirred for 2 min at 2000 rpm (droplet formation) and 2 min at 800 rpm (structure formation). The three phase contact angle determined for this system is 70.3° and thus it is considered to be in the pendular state [11]. Prepared pastes were molded into a sample form (sample size 50x10x10 mm) and the top face was smoothed using a doctor blade. So molded samples were dried, debindered and sintered at 90 °C for 3 h.

Ceramics:

α-Al_2O_3 as coarse ($x_{50,3}$ = 5.76 µm) and fine ($x_{50,3}$ = 0.67 µm) powder fraction was obtained from Almatis (CT19FG, CT3000SG, Ludwigshafen, Germany), t-ZrO_2 as fine powder fraction ($x_{50,3}$ = 0.7 µm) was used from Tosoh (TZ-3YS-E, Minato, Japan). The density of α-Al_2O_3 and t-ZrO_2 is 3.94 kg/m^3 and 6.05 kg/m^3, respectively. Paraffin oil with η = 0.03 Pas was used as bulk phase (paraffin oil thin, Carl Roth, Karlsruhe, Germany). Aqueous 1.853 M sucrose solution (η = 0.08 Pas) was used as secondary liquid phase (α-D-sucrose (D(+)), Carl Roth, Karlsruhe, Germany).

Pure suspensions were prepared using a high shear dissolver at 1200 rpm for 20 min followed by a de-agglomeration step using a ball mill with 25 mm balls for 24 h at 20 °C. Corresponding capillary suspensions were obtained by adding the sucrose solution while stirring with a high shear dissolver at 1000 rpm for 1 min (droplet formation) followed by a second stirring step with a reduced stirring speed of 500 rpm for 1 min (structure formation). Samples with different total volume fractions of ceramic powder between 15 vol% and 25 vol% were prepared, fraction of fine powder relative to total solids volume was varied between 0 vol% and 20 vol%. The amount of secondary liquid phase was held constant at 2.5 vol% relative to the total sample volume corresponding to a maximum yield stress indicating formation of a strong capillary force controlled particle network without spherical agglomeration [16]. The three phase contact angle of the sucrose solution on α-Al_2O_3 is 66° indicating that the capillary suspension is in the pendular state [11]. After structure formation capillary suspensions were homogenized again using a ball mill with 25 mm balls for 24 h at 20 °C. Pastes were molded into a sample form (size 50x10x10 mm) and the top face was smoothed using a doctor blade. The sample form was placed on an absorbent pad and directly demolded after spreading. Debinding the bulk phase was done by capillary extraction for 5 days at room temperature on the absorbent pad followed by a thermal debinding procedure at 200 °C (30 min), 500 °C (1 h) and 800 °C (15 min) for all samples to ensure a complete and gentle debinding of the sucrose and residuals of the bulk phase. Monomodal coarse α-Al_2O_3 powder preparations and the bimodal composite

preparations α-Al_2O_3 + t-ZrO_2 were sintered at 1650 °C for 2 h, bimodal α-Al_2O_3 + α-Al_2O_3 powder compositions were sintered at 1550 °C for 2 h.

4.2.2 Characterization

Particle size distributions for all investigated particle systems were determined using a commercial Fraunhofer diffraction device Helos H0309 equipped with an ultrasonic wet dispersing unit Quixel (Sympatec, Clausthal-Zellerfeld, Germany) according to DIN EN ISO 8130-13. Corresponding results are provided as Fig. S5 (Supporting Information). For the flaky or plate-shaped graphite powder image analysis of scanning electron micrographs was performed to characterize the shape anisotropy and an aspect ratio r = 0.14 of shortest to longest plate dimension was determined in addition to the equivalent sphere diameter $x_{50,3}$ provided in Fig. S5 (Supporting Information).

Three phase contact angles were calculated using the expanded Young-Dupré-equation [11]. The required interfacial tensions were determined using a weight-based tensiometer (Dataphysics, DCAT 11, Filderstadt, Germany) employing a Wilhelmy plate [133]. Contact angles against air on compact substrates made from the investigated powders were measured using the sessile-drop-method (Dataphysics, OCA15, Filderstadt, Germany), evaluated by a numerical Young-Laplace-fit [102]. In case of graphite a low porosity plate (Graphite Coava GmbH, Röthenbach, Germany) with composition similar to the used powder was employed for contact angle determination. Rheological characterization was done with a stress-controlled shear rheometer (Thermo Scientific, Mars II, Karlsruhe, Germany) using a vane geometry (Z20 according to DIN 53019-1). Yield stress values were determined from shear stress ramps, according to the tangent method [134]. An increase of the yield stress upon addition of the secondary liquid phase by about a factor of 5 or more was consider as indication for the formation of a capillary suspension with a strong particle network, corresponding data are included as the Supplementary Information. The porosity of the graphite membranes as well as the sintered ceramic and UHMWPE parts was determined from the Archimedes density according to DIN EN 993-1. Pore size of UHMWPE and graphite parts was measured by mercury intrusion porosimetry (AutoPore III, Micromeritics).Young's modulus of the UHMWPE membranes was determined via compressive strength tests according to DIN EN ISO 604. Compressive strength tests of graphite samples were performed according to DIN 51104 using rectangular shaped parts. Mechanical properties of ceramic parts were measured following DIN EN 843-1 (flexural strength) and DIN 51104 (compressive strength) using reshaped parts with a rectangular cross-section. All ceramic samples for mechanical testing had a porosity of 55%.

Sintered ceramic parts were vacuum infused with epoxy resin, mounted on SiC paper and polished with a diamond suspension (Buehler, Düsseldorf, Germany) to obtain cross-cut scanning-electron-microscopy images in backscattering-mode (SEM-BSE) (Hitachi, S-4500, Krefeld, Germany). Graphite membranes were fractured and sintered UHMWPE samples we cleaved with a sharp scalpel for SEM images (SEM-SE) of the cross-section.

4.3 Acknowledgements

We would like to thank the Almatis GmbH, Schott AG and ThyssenKrupp AG for the donation of the alumina, the glass as well as the stainless steel powder and the smooth collaboration. Ticona GmbH is acknowledged for providing the UHMWPE sample and Imerys Graphite and Carbon Ltd. for donating the graphite particles. Further thanks are given to Thomas Lebe for the work at the SEM-microscope. Katharina Hauf is thanked for providing fluorescence images and rheological data of UHMWPE capillary suspensions including paraffin oil as well as data for corresponding membranes. Ulrich Handge is thanked for drawing our attention to UHMWPE membrane fabrication and fruitful discussions about ceramic material processing with Michael Hoffmann and his co-workers at the Institute for Applied Materials at KIT are also greatly acknowledged.

4.4 Supporting Information

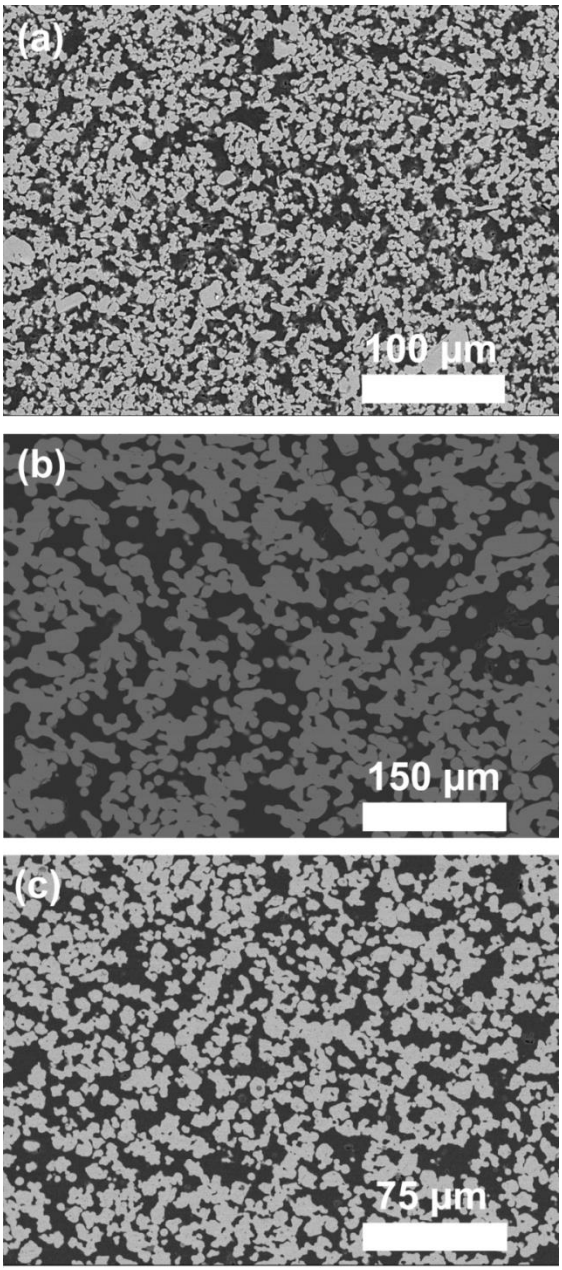

Fig. S1: Porous parts from capillary suspensions for different materials after debinding and sintering with porosities of 55 %: (a) α-Al_2O_3 ceramic sintered at 1650°C for 2h, (b) technical glass ($x_{50,3}$ = 10.0µm, Schott AG, Germany) sintered at 800°C for 0.25h, (c) 316L stainless steel ($x_{50,3}$ = 4.0µm, ThyssenKrupp Metallurgical Products GmbH, Germany) sintered at 955°C for 1h under H_2. Dark areas represent pores, bright regions stand for material. *Reproduced with permission from Wiley-VCH Verlag GmbH & Co. KGaA.*

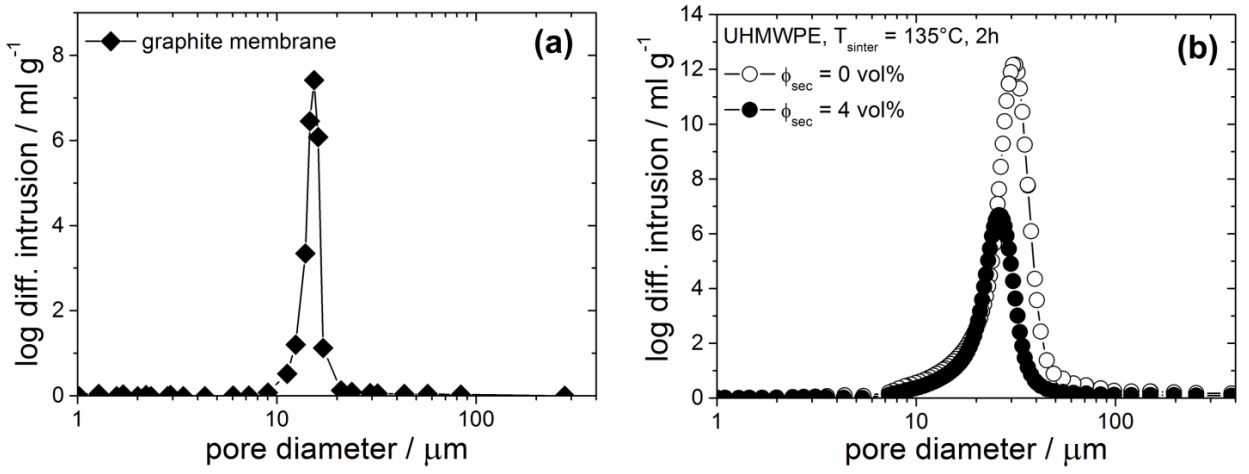

Fig. S2: Pore size distribution as obtained by mercury intrusion porosimetry: (a) graphite membrane (porosity ε = 66%) with a median pore diameter ≈ 15 µm and (b) sintered UHMWPE samples. Median pore diameter slightly decreased from 30 µm for the membrane made from the pure suspension (porosity ε = 77%) to 25 µm for the membrane made from the capillary suspension including 4 vol% m-xylene (porosity ε = 64%). *Reproduced with permission from Wiley-VCH Verlag GmbH & Co. KGaA.*

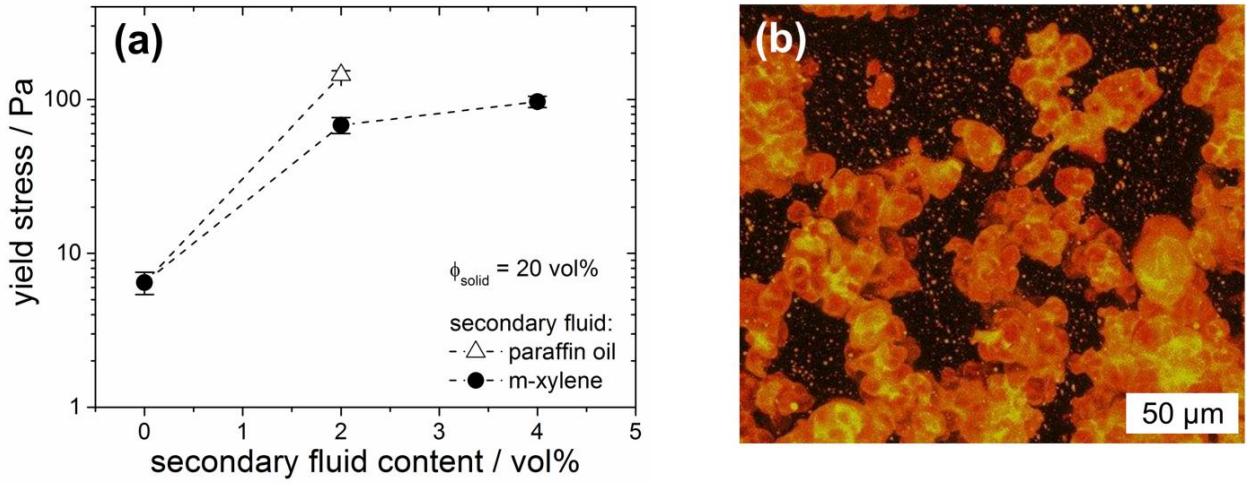

Fig. S3: (a) Yield stress of 20 vol% UHMWPE particles suspended in glycerol with different amount of added secondary fluid and (b) fluorescence microscopy image of a suspension including 4 vol% paraffin oil at a solids content of 20 vol%. The yellow regions represent the paraffin oil (colored with the fluorescent dye nile red), dark regions are glycerol and particles show up in red, because they are coated with a thin layer of secondary liquid including the fluorescent dye. The shown image is a stack of 36 images in a height of 70 µm and was obtained with a confocal microscope (TCS SP8; Leica Microsystems). *Reproduced with permission from Wiley-VCH Verlag GmbH & Co. KGaA.*

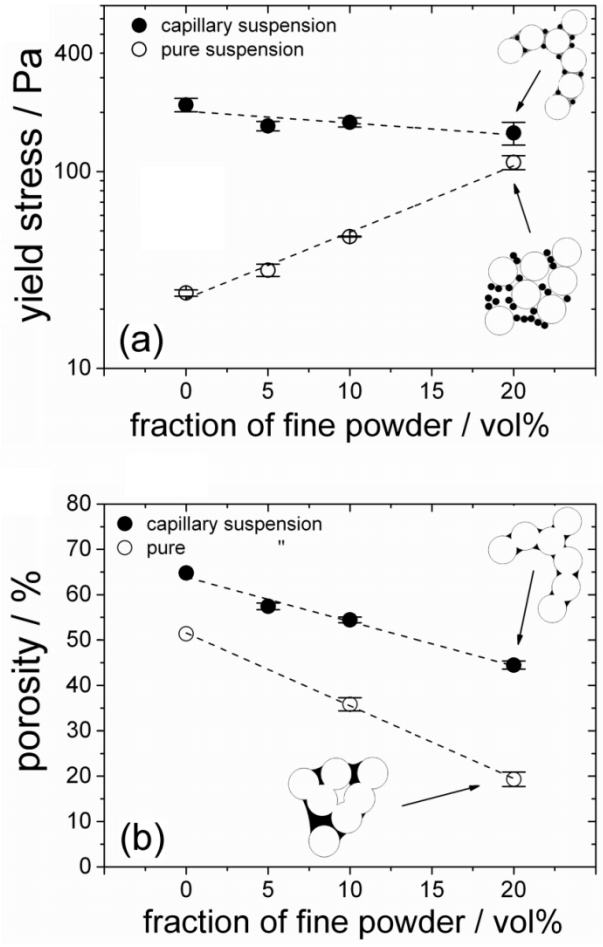

Fig. S4: Yield stress of the suspension (a) and porosity (b) of the corresponding sintered part from pure (open symbols) and capillary suspensions (closed symbols) as a function of fine powder (t-ZrO_2) fraction. Sintering conditions were constant for all samples at 1650 °C for 2 h. The total volume fraction is 15 vol%, the coarse powder fraction is α-Al_2O_3 and the amount of secondary liquid phase is 2.5 vol%. Error bars are the standard deviation calculated from at least three measurements and dashed lines are linear fits to the experimental data. *Reproduced with permission from Wiley-VCH Verlag GmbH & Co. KGaA.*

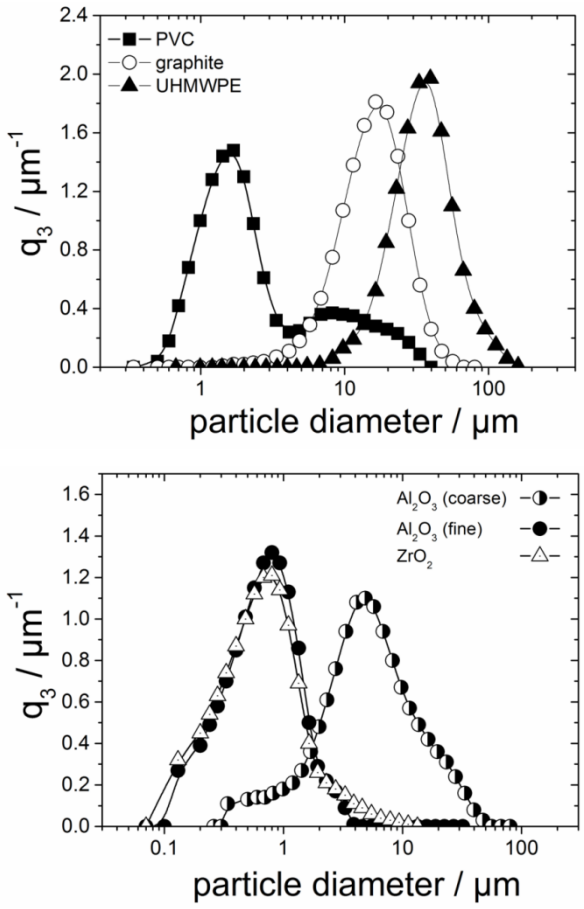

material	$x_{50,3}$ / µm
PVC	1.88
graphite	15.80
UHMWPE	34.30
Al_2O_3 (coarse)	5.76
Al_2O_3 (fine)	0.70
ZrO_2	0.67

Fig. S5: Particle size distribution of the powders used in this study as obtained from Fraunhofer diffraction: bimodal PVC mixture (closed square), graphite (open circle), UHMWPE (closed triangles) coarse α-Al_2O_3 powder (half-closed circles), fine α-Al_2O_3 powder (closed circles) and fine t-ZrO_2 powder (open triangles). The average volume based particle diameter $x_{50,3}$ for each powder is given in the table beneath. *Reproduced with permission from Wiley-VCH Verlag GmbH & Co. KGaA.*

5 Suppressing crack formation in particulate systems by utilizing capillary forces

Full title: Suppressing crack formation in particulate systems by utilizing capillary forces

Authors: Monica Schneider, Johannes Maurath, Steffen B. Fischer, Moritz Weiß, Norbert Willenbacher, Erin Koos

Status: published

Bibliographic data: ACS Applied Materials and Interfaces 9(12) (2017) 11095-11105
10.1021/acsami.6b13624 (https://doi.org/10.1021/acsami.6b13624)

Abstract

Cracks, formed during the drying of particulate films, can reduce the effectiveness or even render products useless. We present a novel, generic approach to suppress crack formation in thin films made from hard particle suspensions, which are otherwise highly susceptible to cracking, using the capillary force between particles present when a trace amount of an immiscible liquid is added to a suspension. This secondary liquid preserves the particle cohesion, modifying the structure and increasing the drying rate. Crack-free films can be produced at thicknesses much greater than the critical cracking thickness for a suspension without capillary interactions, and even persists after sintering. This capillary suspension strategy is applicable to a broad range of materials including suspensions of metals, semi-conductive and ceramic oxides or glassy polymeric particles and can be easily implemented in many industrial processes since it is based on well-established unit operations. Promising fields of application include ceramic foils and printed electronic devices.

5.1 Introduction

Crack formation during drying is a ubiquitous phenomenon important in soil science as well as industrial material and processing development. Understanding crack formation in particle films and developing strategies to suppress crack formation is an important field of research, as desired product properties generally decline with the occurrence of cracks [135,136]. Dried mud, paint coatings, ceramics and many other materials can show cracking during and after solvent evaporation. However, cracking is of utmost importance in hard particle coatings, such as those used in, e.g., printed electronic devices such as battery electrodes[137], photonic crystals or antireflective coatings [138,139], filtration operations, as well as the processing of catalysts and ceramic materials[2], all of which are plagued by this phenomenon.

During the drying process, evaporation leads to solvent retention into the particle network. Menisci form between the particles at the liquid-gas-solid interface, inducing capillary forces and a capillary pressure. The capillary pressure p_c can be expressed by

$$p_{\mathrm{c}} = \frac{2\gamma \cos\theta}{r_{\mathrm{p}}} \qquad (11)$$

assuming a cylindrical pore with radius r_{p} is wetted by a solvent with wetting angle θ and surface tension γ [140]. Hence, a decreasing pore size results in a higher capillary pressure, which acts on the particles and pulls them together. In real systems, pore sizes vary and broad distributions lead to a more pronounced inhomogeneity in the resulting drying stress [141–144]. This capillary pressure also changes during drying as the distance between particles becomes smaller. As this capillary pressure overcomes other forces, such as the compressive stress, cracks form in the film.

There have been many strategies that have been put forth in recent years to reduce cracking. Variations in particle size, shear modulus, inter-particle forces, thermodynamic properties like temperature, humidity or gas flow rate have all been shown to affect the shape and appearance of cracks [145]. Rheological properties, such as the yield stress of the suspension, and vibrational preconditioning of the paste have also been shown to correlate with crack development [146]. For biological and biomimetic materials, a spatial variation of the elastic moduli on the microscopic scale has shown to affect and hinder crack propagation [147].

Due to the generally high shear modulus of inorganic particles, corresponding suspensions are more prone to exhibit cracking during processing. These crack morphologies are dependent on the particle shape as well as any microstructure formed by a percolated network as these

particles dry [148]. Common solutions proposed to achieve fracture-free layers from suspensions include the use of soft particles with a sufficiently low glass transition temperature to allow for a relaxation of the drying induced inter-particle tensile stress by deformation, the addition of a plasticizer, polymer, or a blend of soft and hard particles to provide the required deformability of the particles [149–151]. The use of a soft substrate, or changing other substrate properties such as the wetting and roughness, can also reduce crack formation [152]. Another approach is to coat a colloidal precursor. The evaporation of the solvent leads to an in-situ growth of the particles, which replaces the arising void volume and thus avoids crack formation while drying [153,154]. Sometimes, however, the specific material composition is restricted. In these cases, multi-step coating procedures, increased drying time, or a method of inducing colloidal crystallization during coating can be used to reduce cracking [151,155,156]. Using a multi-step approach or long drying times can be time consuming and costly, however.

The particles can also be incorporated into an existing gel matrix or cracks can be reduced through attractive interactions causing the formation of a percolating particle network [157–159]. In certain applications, however, residual components, e.g. a polymeric binder, can be undesirable [160]. Jin et al. also showed that the incorporation of emulsion drops can be used to decrease the amount of cracking [161]. In this case, increased fractions of the dispersed fluid slowed the rate of air invasion, which may have accounted for the observed change in the cracking pattern. Since the emulsion fluid can be completely removed (though some residue from the surfactant will still be present), the method of Jin et al. is a versatile method to control cracking. A method that combines the use of a secondary fluid (without surfactants) and an induced particle network, should be an even more powerful approach, particularly when the final material composition is strictly limited.

Various relations have been proposed to describe the critical cracking thickness (CCT, h_{max}) [157,162–164]. These relations focus on capillary pressure, particle shear modulus and size, as well as particle coordination number and packing properties of the film. However, other important aspects like drying conditions, substrate properties or the effect of additives are not considered. Moreover, such models are restricted to specific boundary conditions, such as stress- or strain-limited drying regimes. Therefore, such relations are of limited use for quantitative predictions of CCT and it is often better to directly measure the maximum film height for each system at the specified conditions.

Here, we present a generic novel strategy to suppress crack formation during drying of particle suspensions by taking advantage of capillary forces inferred via the addition of a small amount of a second liquid that is immiscible with the main or bulk fluid of the suspensions. Such ternary particle-liquid-liquid systems are termed capillary suspensions [11,35]. Capillary forces can lead

to the formation of a particulate gel comprising a sample-spanning particle network, regardless of whether the secondary liquid wets the particles better or worse than the bulk phase [11]. Two types of capillary suspensions are distinguished depending on the two-liquid wetting angle θ_{2l} that the secondary liquid forms against the solid surface in the bulk phase environment. In the pendular state ($\theta_{2l} < 90°$), the secondary liquid wets the solid phase better than the continuous phase and forms pendular shaped bridges between the particles. In the case where $\theta_{2l} > 90°$, termed the capillary state, the particles form clusters around small volumes of the second liquid [48]. Reported technical applications of capillary suspensions cover a broad range of materials and products including novel food products, such as heat stable or low calorie chocolate spreads [12,13], pastes for printed electronics like e.g. slot-die-coated lithium-ion battery electrodes [15] or front contacts of solar cells with high shape accuracy [160], capillary suspension based foams [54] as well as precursor for highly porous ceramic and glass membranes [10].

In this article, we focus on pendular state capillary suspensions and demonstrate how crack formation is suppressed and drying is accelerated in these systems. A pendular shaped liquid bridge exerts a capillary force F_C between two adjacent particles of same radius R is given by

$$F_c = 2\pi R \gamma_{2l} \cos\theta_{2l} \qquad (12)$$

with the assumptions that the particle separation is zero and the liquid bridge, with the interfacial tension γ_{2l}, is smaller than the particle size [30,49]. More generally, the force will depend on the volume of the liquid bridge as well as the filling angle and the shape of the droplet [165,166]. Further corrections can be included for particles that are not in contact and for rough particles [33,167]. Generally, the capillary attraction is significantly higher and acts over larger distances than the omnipresent van der Waals force [11]. The influence of charge occurs at a very short range and can slow or even prevent particles from approaching. When a bridge does form, the affinity of the interface to the solid surface (e.g. from van der Waals and electrostatic forces) can modify the profile of the drop within a range up to 100 nm [168,169]. The macroscopic contact angle and macroscopic attraction is not affected by this core region, however. The influence of the charge in combination with a capillary interaction depends on the wettability of the surface. Yamamoto et al. showed that the interaction between micron-sized polymer spheres and a silicon wafer with water adsorbed to the surfaces depended on the wafer surface treatment [170]. Hydrophobic surfaces showed an electrostatic interaction at all distances, while the interaction for hydrophilic surfaces changed from electrostatic at long distances to capillary at short distances.

Suspended particles connected by pendular bridges can assemble into sample-spanning networks even at low particle volume fractions ϕ. Such particulate gels then exhibit a yield stress σ_y, which for equally sized particles is given by

$$\sigma_y = f(\phi) g(S, \tilde{s}) \frac{\gamma_{2l} \cos \theta_{2l}}{R} \quad (13)$$

where the number of contacts per particle is captured by the function f(ϕ) [28,52]. The normalized particle separation $\tilde{s} = s/R$ is considered in the term $g(S, \tilde{s})$ along with the amount of secondary liquid added to the suspension, described by the saturation S [11,171],

$$S = \frac{V_{\text{wetting fluid}}}{V_{\text{total fluid}}} \quad (14)$$

The thermodynamics of drying capillary suspensions are very complex. Mass transfer is influenced by numerous parameters such as the diffusivity of the secondary liquid in the bulk fluid, the low solubility of the secondary liquid in the bulk phase, the Laplace pressure in the liquid bridges or the equilibrium partial pressure of both liquid components in the ambient gas phase [172]. The drying process of binary liquid mixtures in porous media has been investigated before, but research is essentially limited to miscible liquid combinations [173,174]. This complexity can be used to tune the drying process allowing the morphology and drying rate to be controlled.

5.2 Experimental section

5.2.1 Sample production

To create the capillary suspensions, TiO_2 particles (Evonik, Aeroxid P25, Essen, Germany, average aggregate radius $R_{50,3}$ = 0.39 µm, polydispersity ($R_{90,3}$ – $R_{10,3}$)/ $R_{50,3}$ = 2.62, ZnO particles (Evonik, VP ADnano ZnO, Essen, Germany, mean aggregate size according to supplier < 0.18 µm), and hydrophobically modified $CaCO_3$ (Solvay, Socal U1S1, Salin de Giraud, France, $R_{50,3}$ = 0.9 µm, polydispersity of 1.54) were dispersed in n-octanol (Merck, Emplura, Darmstadt, Germany) and various volumes of distilled water were added as secondary liquid. For the infrared spectroscopy measurements, the distilled water was replaced by deuterium oxide D_2O (Carl Roth, Karlsruhe Deutschland). During sample preparation, the particles were slowly added to the bulk fluid while stirring at low speed with a turbulent beater blade (200 rpm), the mixture

was then stirred at high speed (30 min, 1000 rpm) to ensure a homogeneous distribution. Finally, the capillary network formation was induced by adding varying amounts of the secondary liquid and maintaining the high stirrer speed for another 5 minutes. The solid volume fraction ϕ of the capillary suspensions were ϕ_{TiO2} =0.04, ϕ_{ZnO} = 0.05 and ϕ_{CaCO3} =0.10. The TiO_2 samples containing surfactant were prepared with 10 vol% aqueous surfactant solution (Evonik, Tego Dispers 752W, Essen, Germany) as secondary liquid.

The suspensions were coated on hydrophilic polyester foils with a doctor blade made of brass. The doctor blade gap height was 100 µm and accurate shapes were achieved by confining the pattern with a 60 µm thick adhesive tape to a square with 1 cm sides and making multiple passes. The blade was drawn over the polyester foil (Folex Coating GmbH, X-500, Cologne, Germany) with a constant velocity of 50 mm/s. This caused a shear rate of 300 s^{-1}, a value typical for screen printing. Additionally, this speed was chosen so that a smooth, homogeneous and continuous wet film was generated. The viscosity of the suspensions at the coating speed varied between 135 ± 4 mPa·s for the sample without added water to a maximum of 550 ± 20 mPa·s for the S = 0.05 samples (the viscosity for the higher saturation samples is lower than for the 5 % sample). Furthermore, multiple passes ensured that the wet films all had the same 160 µm thickness. The films were then left in the fume hood to dry at room temperature. Films with varying saturations were prepared and dried simultaneously. Humidity during drying varied slightly around 75 %. After a drying time of 48 hours, the sample surfaces were analyzed in a scanning electron microscope (Hitachi, S-4500, Krefeld, Germany). The height profiles were examined with a 3D laser microscope (Keyence, VK-X100 Laser Microscope).

The ceramic discs were prepared with α-Al_2O_3 (Almatis, CT3000SG, Ludwighafen, Germany, $R_{50,3}$ = 0.34 µm, polydispersity of 2.40), paraffin oil as the bulk phase (Carl Roth, Karlsruhe, Germany) and a water-sucrose solution as secondary phase (Carl Roth, D(+)-Sucrose, Karlsruhe, Germany, 1.835 M). Additionally, the suspension contained 0.5 vol% of the surfactant polysorbat 20 (Carl Roth, Tween 20, Karlsruhe, Germany) to avoid agglomeration. The solid volume fraction of the suspension was ϕ_{Al2O3} = 0.15. The suspensions were stirred for 10 minutes at 1200 rpm with a turbulent beater blade, another 5 minutes after adding the surfactant, and again for 10 minutes at 800 rpm after adding the secondary phase. The final homogenization step was a 24 hour ball mill treatment. The suspensions were coated on a porous Al_2O_3 substrate, followed by a thermal debinding procedure (30 min at 200 °C, 1 h at 500 °C and 15 min at 800 °C) and then sintered (2 h at 1550 °C). The magnified images were made with the 3D laser microscope.

Nickel films were used for conductivity measurements. The nickel powder (abcr GmbH, 100–150 nm Nickel Nano Powder, AB 254802, Karlsruhe Germany) was dispersed in 1-octanol with

using a turbulent beater blade at 1000 rpm for 15 min. The suspensions were stirred again at 1000 rpm for 5 min after adding distilled water. The films were coated onto a glass substrate using a Universal Applicator (Zehntner, ZUA2000, Sissach, Switzerland) and dried overnight at 220 °C.

5.2.2 Characterization

The static three phase contact angle θ_{2l} was measured to characterize the solid-liquid-liquid systems. The particles were pressed to a dense tablet under a pressure of 19 MPa and sintered at 1000 °C for five hours in order to achieve a densely packed structure. The sintered tablet was polished, placed in a glass container and covered with n-octanol. A droplet of distilled H_2O or D_2O was placed on the surface of the tablet using a syringe and the resulting three phase contact angle θ_{2l} evaluated via an image analysis program (Krüss, Drop Shape Analysis, Hamburg, Germany). The root mean squared surface roughness of the TiO_2 tablet was 0.33 ± 0.05 µm with an average distance between peak and valley of 0.8 ± 0.1 µm. Since the drops we used to measure the contact angles were much larger (mm), we ignored the effect of surface roughness. It should be stated that the difference in roughness of the particles compared to this substrate would change the effective contact angle. Additionally, the oxide surface may change with time or after it was heated during the sintering procedure. It is not our intention that this contact angle be used to directly calculate the interaction force, but rather this measured contact angle be used as an indication that the prepared suspensions were in the pendular state.

Infrared spectroscopy (Bruker, Tensor FT-IR 27) was performed using a diamond attenuated total reflection (ATR) crystal in order to determine the chemical composition of the capillary suspension film during drying. The suspensions were coated onto the ATR crystal with a defined shape of 5×5 mm² using a 100 µm doctor blade and an adhesive tape mask with the desired cut-out area. The infrared absorbance spectra of the pure substances were also measured as can be seen in Fig. 39.

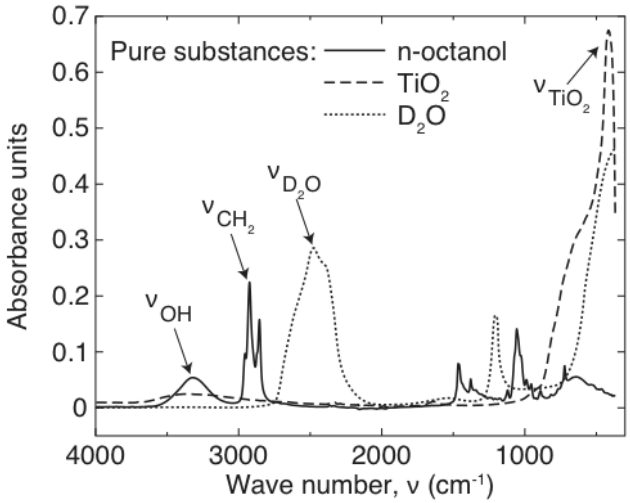

Fig. 39 Infrared absorbance spectra of the pure substances of the capillary suspension annotated with characteristic peaks for tracing the different substances. *Reproduced with permission from ACS Applied Materials and Interfaces.*

The yield stress of each suspension was determined with a rotational rheometer (Thermo Scientific, Mars II, Karlsruhe, Germany) and sandblasted plate/plate (35 mm diameter) geometry. By applying successively increasing stress values and measuring the resulting equilibrium deformation, two distinct linear regimes can be found in a double-logarithmic plot. The yield stress is then defined as the intersection of the two linear curve fits representing the onset of irreversible deformation. The measurement error was estimated to be 10% and includes the reproducibility of sample preparation and measurement.

Finally, the influence of cracking on the functionality of different films was characterized using permeability, filtration, and resistivity measurements. Permeability of ceramic membranes was measured using a pressure strainer (DrM, Maennedorf, Switzerland) where the volumetric flow rate was measured using an electronic balance. The experiment was conducted at room temperature using water with a pressure difference of 1.5 bar. The filtration tests used monomodal polystyrene particles with diameters of 1 µm and 5 µm (Micromer 01-00-103 and 01-00-503, Micromod Partikeltechnologie GmbH). The filtration was carried out at room temperature using 40 ml samples with a concentration of 1 x 10^{-4} g/ml. The filtration gauge pressure was 1.5 bar. Particle size distribution before and after filtration was obtained using dynamic light scattering (Zetasizer Nano ZS, Malvern). Bubble point tests were conducted following ISO 4793. The conductivity of nickel films was measured using a four-point probe with 3.96 mm diameter electrodes spaced inline at 10 mm. The voltage was supplied with a Voltcraft VLP-1303 Pro power supply and the current measured using a Benning MM9 multimeter. Conductivity was measured after films were coated onto a glass substrate and dried overnight at 220 °C.

5.3 Results and discussion

Capillary suspensions promise a new formulation route for manufacturing crack-free particulate films because the capillary network can suppress stress induced, crack-forming particle migration during the drying process. Titanium oxide TiO_2 capillary suspensions with n-octanol as bulk phase and water as secondary liquid form a pendular state network with a three-phase contact angle of 79°. Thus, the secondary liquid forms pendular bridges between the particles creating a sample-spanning network that avoids sedimentation and further particle aggregation after dispersing. The SEM images in Fig. 40a show the dry film surfaces of the pure TiO_2 suspension and the capillary suspensions with varying saturation S. The images clearly demonstrate that crack formation during drying is significantly suppressed upon addition of the secondary liquid. A difference in crack formation due to variations in the dry film thickness can be excluded here, as this quantity only varied between 15.6 and 17.4 µm for the sheets shown.

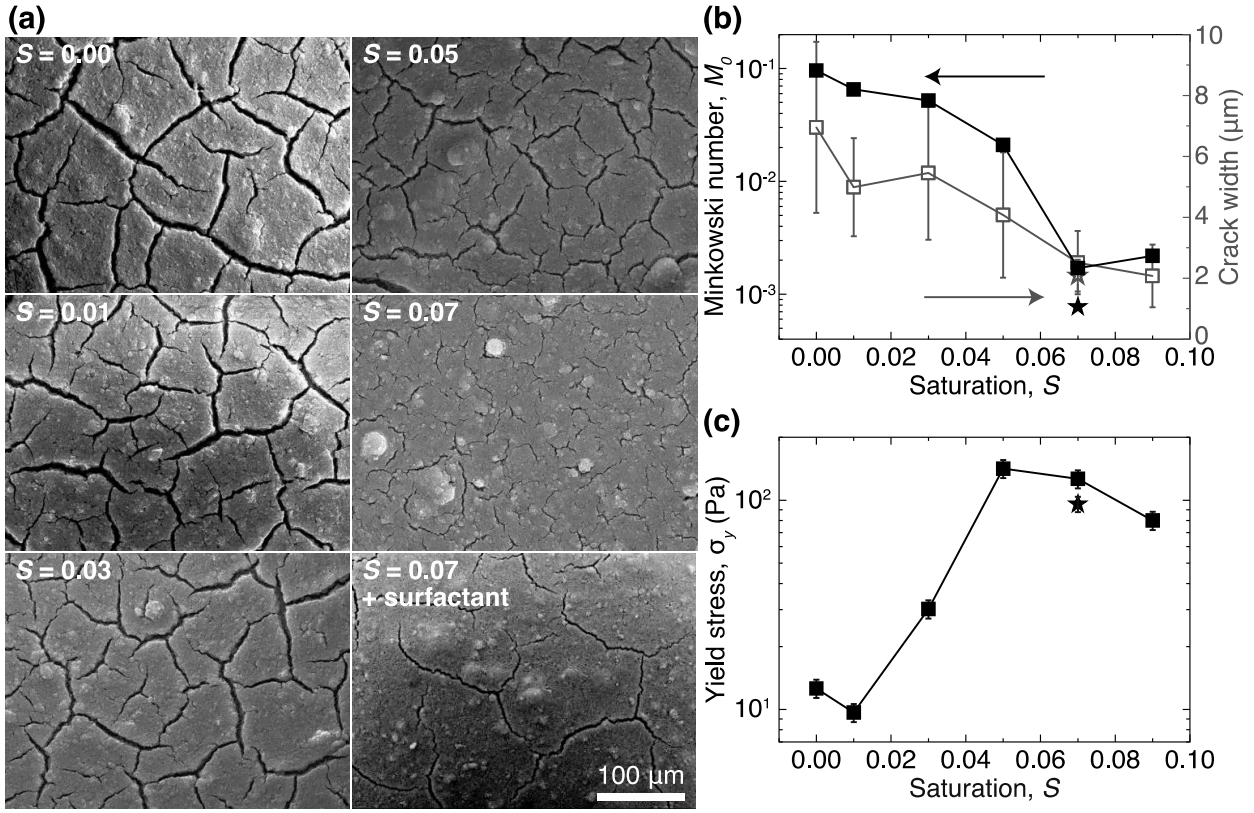

Fig. 40: (a) Surface morphology and (b) area density M_0 and average crack width after drying for TiO_2 particles dispersed in n-octanol with ϕ = 0.04 and increasing amounts of secondary liquid S. (c) Yield stress σ_y vs. saturation S for the TiO_2 suspensions prior to drying. The data point at S = 0.07 with 10 vol% Tego Dispers 752W in the secondary liquid is additionally shown in the lower right image and as a star in (b) and (c). *Reproduced with permission from ACS Applied Materials and Interfaces.*

A simple quantification of the crack development can be achieved by binarization of the SEM images. The Minkowski number M_0 describes the area density of the cracks (the crack area divided by the total image area) [175] and the resulting values are shown in Fig. 40b as a function of saturation, quantitatively characterizing the reduced cracking. For the sample without added secondary liquid (S = 0.00), the SEM image reveals a high number of long cracks in the dried film. These cracks connect multiple domains and have a tip-to-tip length spanning the image. The surface morphologies of the dry particulate films change when adding increasing amounts of water to the TiO_2 suspension. The visible number of cracks is reduced and the size also changes to narrower and shorter cracks that no longer interconnect to form closed domains. These average crack widths are also shown in Fig. 40b, where the error bars show the standard deviation for the crack widths. The average width decreases roughly linearly with saturation and the standard range of widths also decreases. The successful formation of the capillary network is evident from the increasing yield stress as a function of the saturation S (Fig. 40c). Without any added secondary liquid, the suspension yield stress is around 10 Pa and increases by an order of magnitude when adding up to 5 % of H_2O. With 7 % of secondary liquid in the capillary suspension, the cracks are hardly recognizable and M_0 reaches a minimum – decreasing by two orders of magnitude. However, spherical agglomeration occurs at saturations above the point of maximum network strength (as measured by the yield stress) indicated by the large, round aggregates, which are clearly visible for S = 0.07. This phenomenon has also been observed for other capillary suspension systems [16,31]. Here, a small amount of surfactant added to the secondary liquid helps to avoid these aggregates, as shown in the bottom right image in Fig. 40a without a significant decrease in the yield stress (star in Fig. 40c).

The decrease in cracking is not due to variations in the film height, which was kept constant. Any changes due to differences in packing can also be excluded as the sheets had the same 160 µm height before drying and nearly uniform heights, 15.6-17.4 µm, with no trend in saturation, after drying. For the suspension without added secondary fluid, a CCT as low as 3 µm was measured. The films shown in Fig. 40 are well above this critical value and the clear cracking observed in this film is consistent with this measurement. The CCT measured in the suspension without added liquid is lower than measured for other ceramic films [163,176], but those films had an aqueous bulk fluid, were dried under different conditions and contained polymeric binders. Since our film did not contain such additives, a lower CCT would be expected. Furthermore, the TiO_2 particles used here were agglomerates of smaller primary particles. This CCT can also be calculated for the pure suspension using various theories, but we would have to make assumptions about key parameters [157,163]. These theoretical calculations also cannot be used to predict the CCT for the pendular state material systems since they do not

include the contribution of capillary forces to the crack formation phenomenon. This contribution is clearly significant considering the dramatic increase in the critical cracking thickness for the capillary suspension over the suspension without added liquid.

The schematic in Fig. 41 compares a stabilizer-free suspension with a capillary suspension in the wet film at various times during drying and serves as a hypothesis for the significant difference in the critical cracking thickness in capillary suspensions. Initially, both suspensions are completely covered by the bulk solvent. As the film begins to dry at $t_1 > 0$, the solvent recedes into the pores. Most of the solvent has evaporated at a much later time $t_2 \gg t_1$. The non-stabilized particles agglomerate resulting in a broad pore size distribution between particles and the agglomerates. In the case of the capillary suspension, the secondary liquid maintains the homogeneous particle distribution during the initial drying process causing more uniform pore diameters. At a constant bulk solvent contact angle θ and surface tension γ, the capillary pressure p_c in the pores is inversely proportional to the pore radius r_p where smaller pores lead to a higher capillary compression of the surrounding solid while drying.

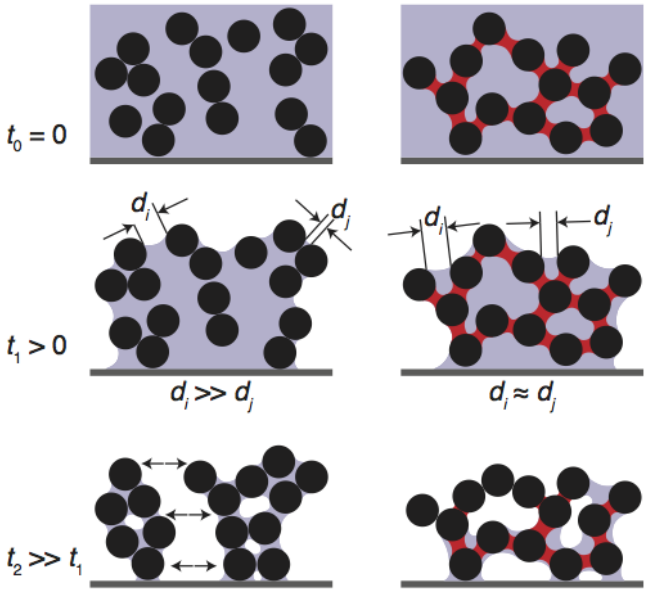

Fig. 41: Particle distribution in a non-stabilized particle suspension (left) and in a capillary suspension (right) at various times during drying where t_0 represents the initial time of coating, t_1 some later time as the film begins to dry, and t_2 the time when the film is nearly dry. *Reproduced with permission from ACS Applied Materials and Interfaces.*

Consequently, these variations in capillary pressure, which are caused by the broad pore size distribution across the sample volume, lead to huge anisotropic stress differences during the drying process that inevitably cause cracks [140,145]. For the capillary suspensions investigated here, the pendular bridges between the particles resist particle motion into compact domains

and therefore provide a balanced drying stress across the sample surface. Therefore, the capillary pressure across the particulate film is uniform causing the number and size of cracks to diminish. The typical time for motion of the particles from the capillary bridges ($t_{\mathrm{capillary}} \approx 96$ ns) is much shorter than the typical time for the bridge to evaporate (t_{drying} ≈500 µs) [142], so response of the network to changes in the drying front can be considered to be nearly instantaneous.

This change in the pore morphology as well as the existence of a sample-spanning particle network was shown in a previous microscopy study that used an index-matched model system [26]. In that work, the direct bridging of the particles by the secondary fluid in the pendular state as well as clustering of particles in the capillary state are visible. Neighboring particles tend to be in contact (as evidenced by the location of the primary peak in the pair distribution function) with adjacent particles separated by a distance slightly less than four particle radii. This particle separation is fairly uniform for each of the capillary suspensions imaged in that work. Furthermore, the existence of a multiply-connected sample-spanning particle network where two particles are connected through at least one pathway was shown in the 3D images [26]. This particle network would significantly reduce particle migration since any motion by a single particle would require movement of multiple other particles. Since the capillary bridges are much stronger than other types of interparticle forces [11,48], this movement is greatly hindered.

In the stress-limited regime, the critical crack thickness is given by a balance between the elastic energy and the increased surface energy [163]. Usually, this maximum stress is given by the maximum capillary pressure ($-P_{\mathrm{max}} \propto R^{-1}$) [177], but in this case, the capillary pressure is opposed by the bridging capillary interactions with a yield stress $\sigma_{\mathrm{y}} \propto R^{-1}$ [29,52]. This means that the capillary pressure and the yield stress both have the same dependence on the particle size. Therefore, we do not expect the capillary interactions to change the relationship between the CCT and particle size [163,164]. Air invasion also occurs via bursting rather than cracking for large particles [178]. The capillary network also resists such particle motion, so this bursting may be reduced as well. The capillary suspensions may also be affected by surface charge. Such a charge is expected to weaken the capillary interaction in the wet state [170] and decrease the final packing fraction when the film is dry [177]. The influence of particle surface charges, however, seems to be small for the systems investigated here. A strong increase in yield stress occurs when the secondary fluid is added, i.e. capillary bridges form and their force is quite strong despite of potentially counteracting surface charge effects. Electrostatic interactions will not have an effect on the suspension without added water.

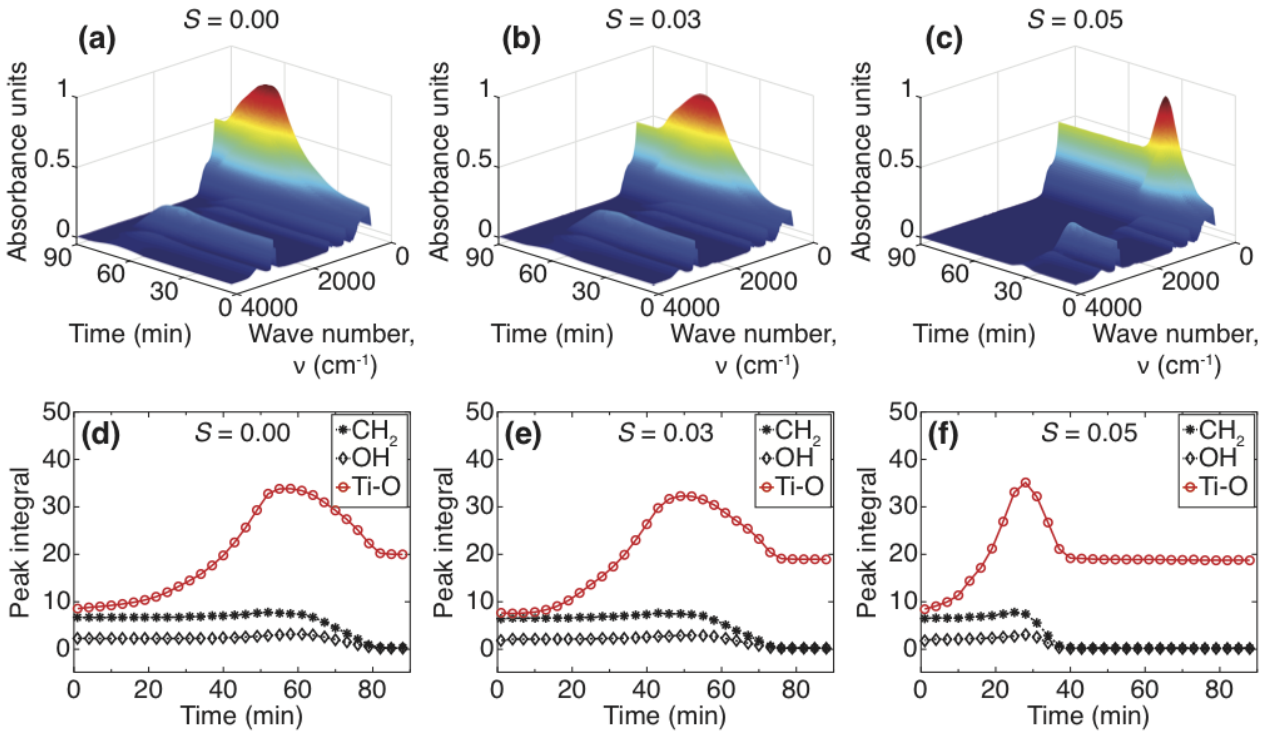

Fig. 42:(a-c) Infrared absorption spectra and (d-f) corresponding surface integrals (i.e. intensity) of characteristic n-octanol (CH_2 and OH) and Ti-O peaks for TiO_2 capillary suspensions with three different D_2O saturations as a function of drying time. *Reproduced with permission from ACS Applied Materials and Interfaces.*

In order to gain more insight into the change of sample composition while drying, infrared spectroscopy has been employed revealing a distinct change in drying velocity due to the presence of the secondary fluid in the samples. The films were coated onto an attenuated total reflection (ATR) crystal and the resulting absorption intensity of the infrared light as function of the wave number ν and time is depicted in Figure 4a-c. The absorbance spectra of the pure substances can be found in Fig. 39. The suspensions were prepared with deuterium oxide D_2O as secondary liquid with a clearly distinguishable peak at 2476 cm^{-1} not interfering with the n-octanol absorption peaks, e.g. the methylene stretching resonance frequency $\nu_{CH_2} = 2930$ cm^{-1} and the alcohol specific OH-band at $\nu_{OH} = 3330$ cm^{-1} [179]. TiO_2 shows resonance at a frequency of $\nu_{TiO_2} = 419$ cm^{-1} presumably corresponding to the Ti-O lattice vibration [180,181]. The area under each characteristic resonance peak was calculated for $\upsilon_i \pm 20$ cm^{-1} and plotted as a function of time in Fig. 42d-f. Significant differences can be found for the drying kinetics depending on saturation. The time-resolved absorption spectra for the sample with $S = 0$ are shown in Fig. 42a,d. After 81 minutes, the absorption at the characteristic frequencies ν_{OH} (3330 cm^{-1}) and ν_{CH_2} (2930 cm^{-1}), indicating the residual solvent, has disappeared. The dry film state is reached and the only remaining peak visible, at a wavelength of 419 cm^{-1}, is attributed to

the solid TiO_2. The maximum of the TiO_2 peak intensity at approximately 60 minutes is due to a superposition of contributions from all components in this frequency range and does not correspond to any changes in the Ti-O lattice. The time at which only the TiO_2 peak remains and the intensity of this peak is constant is assumed to correspond to the state where the thin film is completely dry. Adding D_2O to the suspension shows a decrease of the drying time, with $S = 0.03$, the dry state is reached after 75 minutes (Fig. 42b,e) and this is further reduced to 42 minutes for $S = 0.05$ (Fig. 42c,f).

To understand how the addition of a secondary fluid reduces the time to evaporate the bulk solvent, we assume that the bulk fluid evaporates first. The negative Laplace pressure due to the concave shape of the pendular bridges and the interfacial tension (8.52 mN/m) [182] between the two liquids prevents the rapid evaporation of the secondary liquid, keeping the water trapped in the pendular bridges until the bulk octanol surrounding the bridges is removed. These bridges remain during the initial drying steps holding the particles in their initial position corresponding to a homogeneous inter-particle pore size distribution during the drying process. This hypothesis is complicated by the lower vapor pressure at ambient conditions of the n-octanol ($p_{v,\,octanol,\,20°C} = 0.031$ mbar, $p_{v,\,H_2O,\,20°C} = 23.37$ mbar) and the low, but measurable solubility of water in octanol (48.67 ± 0.50 mg/g at 20 °C [183]. While this solubility corresponds to a saturation of $S = 0.039$, the actual amount of water dissolved in the octanol would be much lower given the slow dissolution rate and thermodynamic stability of concave bridges. As the bridges between particles are filled with the solvent (water) with a higher vapor pressure, the total drying time decreases with increasing amount of secondary fluid. This effect, however, is not as great as the large reduction in drying time seen in the IR absorbance spectra in Fig. 42. It should be noted, however that the dissolution will be affected by the bridge size both when these bridges are surrounded by the secondary liquid and when surrounded by air. The smaller droplets are thermodynamically more stable than the larger droplets, but difference in force for these drops is more sensitive to small changes in volume.

Generally, the initial mass transfer during drying is not influenced by the particle packing unless the solid volume concentration exceeds 60-75 %, below which the evaporation rate of the suspension is comparable to the evaporation rate of the pure bulk fluid [184,185]. This contradicts the obviously enhanced drying rate for capillary suspensions (Fig. 42). Drying of particulate systems underlies a capillary diffusion limited regime, when the solvent recedes into the pores. Thus, an increased solvent mass transfer for the capillary suspensions might be attributed to the improved wetting of the capillaries due to hydrogen bonds that can be formed between n-octanol and water [186,187][186,187][186,187]. Alternatively, the evaporation rate can also be reduced by skin formation on the film surface [188,189]. In the pure suspension, a

fraction of fine TiO_2 particles (primary particle size ~25 nm) might be able to diffuse within the solvent due to low interparticle forces and decrease evaporation rate when forming a packed layer at the evaporation front as in the formation of coffee rings [190,191]. In the capillary suspension, the particles are trapped by the secondary liquid and are unable to follow the evaporation front. This striking change in evaporation rate will be addressed in future research.

The formation of capillary suspensions is a generic phenomenon and has been observed for a large number of particle-liquid-liquid combinations [11,35]. The change in drying and crack formation has also been investigated using other materials besides the TiO_2 system discussed above. E.g. the surface of dry films made from zinc oxide capillary suspensions (ZnO in octanol, $\phi = 0.05$, with added water) exhibits a similar reduction in crack formation with increasing saturation (Fig. 43a). In this system, the cracking is almost completely prevented at $S = 0.05$ with very little spherical agglomeration. The example with ZnO was in the pendular state, but this reduction in cracking caused by the capillary force can also be observed in the capillary state, where the secondary liquid does not preferentially wet the particles. In the example shown in Fig. 43b, hydrophobically modified $CaCO_3$ is dispersed in octanol ($\phi = 0.10$) with added water. Since the preferentially wetting liquid is the majority liquid, the sample without added liquid has $S = 1.00$, and $S = 0.97$ with 3 vol% added water. This capillary state system shows large cracks without added water, but no cracks when water is added. Once again, the cracking was not due to differences in the film height since both films have a dry film thickness of 20 µm. The network formed in the capillary state can be a mixture of strong capillary and relatively weak van der Waals interactions [26]. Therefore, we still expect mixing conditions to be more critical in the capillary state [38]. The reduction in cracking in the capillary state may also be more sensitive to the drying conditions as the energy balance forcing the particle-liquid-liquid system to form a stable capillary suspension may not be valid anymore when the surrounding bulk fluid is totally evaporated due to the sensitivity of this state to the contact angle [48]. This can significantly weaken the attractive force during the later drying stages. Despite these shortcomings, a reduction in cracks in both pendular and capillary state systems can be demonstrated.

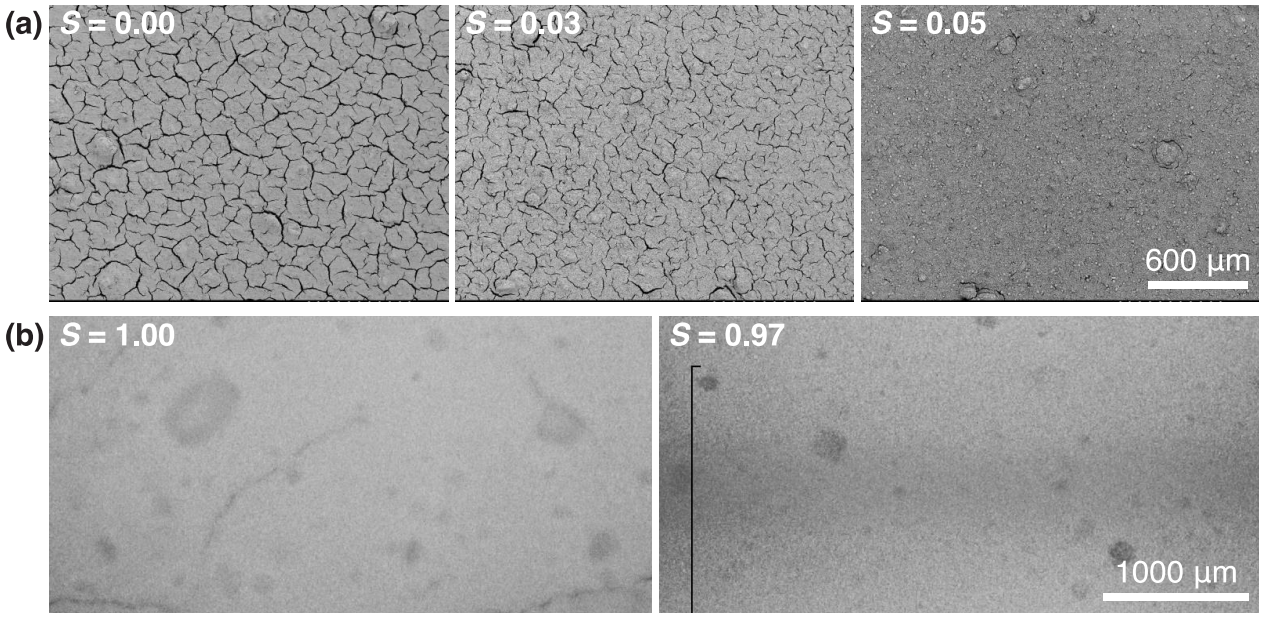

Fig. 43: Dry surface pattern of (a) the pendular state system using ZnO and (b) the capillary state system using $CaCO_3$ particles. ZnO was dispersed in n-octanol ($\phi = 0.05$) and stabilized as capillary suspension with H_2O at various saturations as specified in the images. Hydrophobically modified $CaCO_3$ was dispersed in n-octanol ($\phi = 0.10$) shown with and without added water. *Reproduced with permission from ACS Applied Materials and Interfaces.*

The particle volume fraction is also expected to influence the observed cracking. In the case where no secondary liquid is present, either a thinner region is observed in the center of the sample (e.g. in the TiO_2 suspension) as the particles flow towards the edge of the drop where they form a compact region, or the film shrinks and a denser layer is observed (e.g. in the Al_2O_3 suspension). The former case should result in the observed cracks becoming thicker and with a wider spacing at higher volume fractions [159]. In the latter case, the amount of shrinkage should change with the volume fraction, meaning that the final film may be above or below $h_{\max}$ depending on the geometric restrictions. In capillary suspensions, the shrinkage of the film is reduced (or nonexistent) and no particle mobility towards the edges is observed. This observation is consistent with the case that the initial (pinning) and intermediate (packing) drying being replaced by the final (percolation) stage in the capillary suspension samples where a percolating particle network is already present. Therefore, the presence of the capillary network is expected to have a more pronounced effect at low volume fractions. However, crack formation can be significantly reduced even in suspensions with particle loading as high as $\phi = 0.15$ as shown for the Al_2O_3 system below.

The reduction in crack formation was investigated in the previous examples using an n-octanol/H_2O system. This reduction can also be observed using paraffin oil as bulk phase and a water-sucrose solution as secondary phase for Al_2O_3 (Fig. 44). In this case, the solid volume

fraction ($\phi = 0.15$) was higher than the previous examples and even thicker (300 µm wet film) crack-free layers were obtained. These layers are coated onto a porous ceramic substrate, debinded to remove the liquids and then sintered. The bulk fluid is removed through suction into the porous substrate in addition to evaporation during debinding. This suction can be treated as an "accelerated drying" where capillary forces still play an important role as in conventional air drying processes (e.g. the evaporation of octanol in water in the systems discussed above). The film thickness after debinding was 193 µm for the pure suspension and 290 µm for the capillary suspension. The film from the pure suspension becomes even thinner and denser during sintering (175 µm, porosity $\epsilon \approx 35\,\%$) than for the capillary suspension (290 µm, $\epsilon = 55 \pm 2\,\%$). This density results from settling of particles in the weak particle network of pure suspensions during drying and debinding. Dittmann et al. already observed a lower porosity and consequently a stronger shrinkage of ceramics based on pure suspensions compared to ceramics made from capillary suspensions [10]. Such a change in the final porosity of the debinded film could also change the CCT [164], but this effect is minor compared to the influence of the capillary network itself. The crack-free capillary suspension film shown in Fig. 44 is more than 6 times greater than the CCT for the suspension without added liquid (46 µm in the debinded state). While a change in porosity should affect h_{max}, our measured values for the CCT clearly show that the bridges increase this value by much more than would be predicted for the change in porosity alone. Therefore, the bridges are clearly beneficial for reducing cracks.

The use of a capillary suspension prevented the formation of cracks on the surface after debinding and this crack-free surface even persisted after sintering. SEM images of the film cross section for ceramic films made from pure suspensions show that the cracks extend through the film thickness and there is even partial delamination of the film from the substrate near the crack. The particle migration was restricted in the capillary suspension following drying and during the initial stages of debinding by the presence of sucrose in the secondary fluid, which crystalized at the particle contacts. The persistence of this crack-free nature in capillary suspensions, even during sintering when all of the secondary fluid has been removed, is likely due to the sample-spanning particle network where particles are connected to multiple neighbors [26].

In the example shown in Fig. 44, the 300 µm films were coated onto a sintered Al_2O_3 substrate with height of 2 mm and porosity of 53 ± 2 %. Such layered, or asymmetric, membranes are used in particle filtration and gas separation where a thin filtration layer is used to maximize the flow rate while ensuring sufficient mechanical strength [192]. The difference in cracking has a significant impact on the performance of the filter. Permeability measurements show that the sample with cracks made without secondary liquid ($S = 0.000$) has the same permeability as the

substrate (39.1 ± 6.4 m^3/(m^2·h·bar) versus 38.2 ± 1.3 m^3/(m^2·h·bar) for the substrate). The sample with added liquid ($S = 0.015$) has a much lower permeability of 12.1 ± 3.9 m^3/(m^2·h·bar). The same trend in permeability was also confirmed for thinner (100 µm) layers. The film created from the pure suspension had clear cracks and a permeability of 38.9 ± 1.5 m^3/(m^2·h·bar) whereas the capillary suspension layer had no visible cracks and a permeability of 26.2 ± 1.3 m^3/(m^2·h·bar). In the capillary suspension samples, the much lower permeability shows that top layer is intact and can still be used for particle separation. The layers created without secondary fluid are nonfunctional as small particles would readily pass through the large cracks to the substrate.

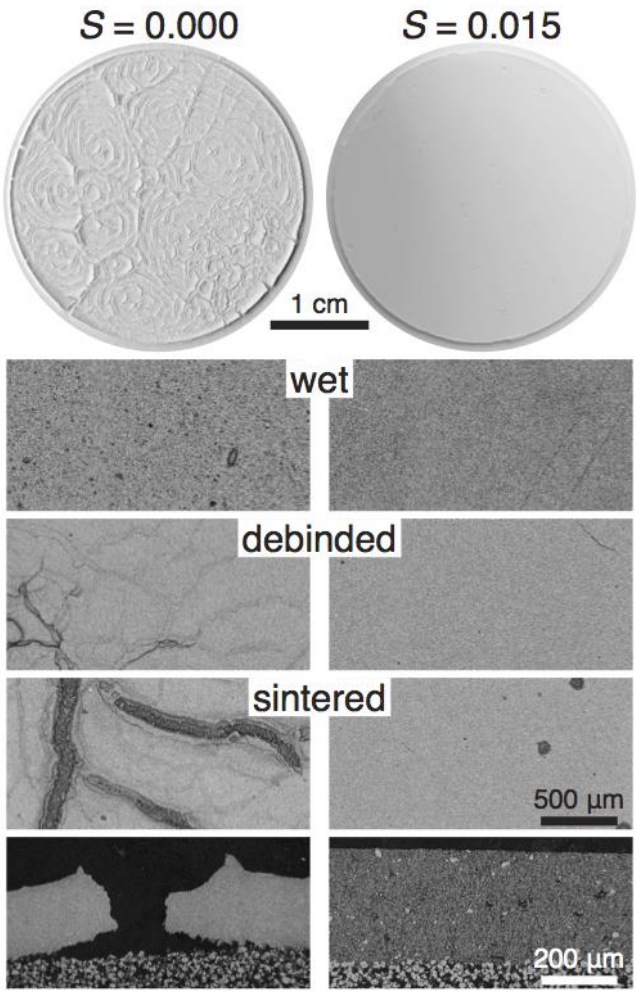

Fig. 44: Wet, debinded, and sintered Al_2O_3 ceramic layers with solid volume fraction $\phi = 0.15$ and with saturation (left) $S = 0.000$ and (right) $S = 0.015$. The bottom SEM images show a cut and polished portion of the sintered films. The diameter of the discs (shown after sintering) is 30 mm with a wet film thickness of 300 µm. The ceramic layers with $S = 0.000$ show strong crack formation after the debinding step and even partial delamination after sintering. *Reproduced with permission from ACS Applied Materials and Interfaces.*

This loss in functionality is clearly evident in the filtration tests shown in Fig. 45. Monomodal polystyrene particles with a diameter of 1 µm can be successfully separated by the 100 µm (wet film) capillary suspension based membrane whereas the membrane made from the pure suspension was not able to separate 5 µm particles due to the large macroscopic cracks. The pore diameter for the pure suspension sample is $d_{50,3} = 1.2 \pm 0.1$ µm and $d_{10,3} = 0.46 \pm 0.03$ µm. The membrane made from the capillary suspensions exhibits an average pore size of $d_{50,3} = 4.0 \pm 0.2$ µm and $d_{10,3} = 1.7 \pm 0.01$ µm. The pore sizes were measured through image analysis of crosscut SEM images, which can overestimate the pore size compared to other common methods (e.g. Hg-porosimetry) [10,16]. Consequently direct correlations between cut-off determined by filtration tests and pore size from image analysis are not possible. Nevertheless, it should be easier to separate 1 µm particles with the sample without added secondary phase than with the capillary suspension sample, since the $d_{10,3}$, which should roughly correspond the size of the neck between pores – the limiting length scale for particles to pass through the filter – is significantly smaller. The failure of this membrane is obviously due to the large cracks present. This is further confirmed using a bubble-point test, which measured a pore size of 6.7 ± 0.1 µm for the film sample. This pore size is close to that of the substrate itself (7.4 ± 0.3 µm), indicating that the cracks cause this film to have a negligible impact on particle filtration.

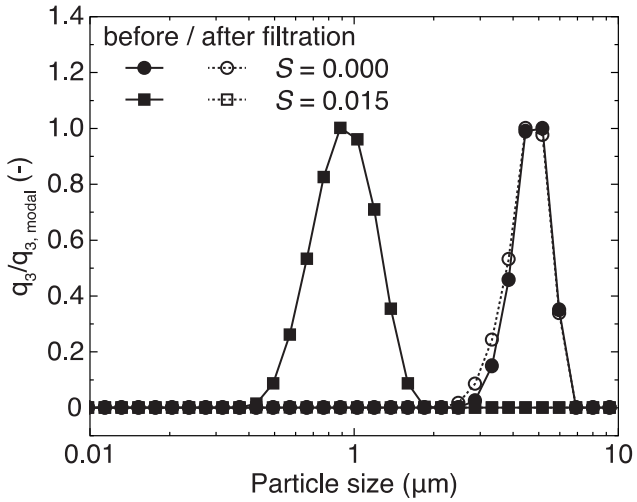

Fig. 45: Results of filtration tests for a crack-free capillary suspension membrane ($S = 0.015$) and a pure suspension membrane ($S = 0.000$) with large cracks. Both membranes had a wet thickness of 100 µm. Test suspensions were polystyrene particles in water. The particle size distributions shown here are normalized by the corresponding modal value of the size distribution. The crack free capillary suspension membrane successfully separates 1 µm polystyrene particles. The pure suspension membrane cannot even separate 5 µm particles. *Reproduced with permission from ACS Applied Materials and Interfaces.*

A similar loss of function with cracking can also be seen for conductive films like the Ni layers investigated here. Increased cracking can decrease the conductivity of a film by lengthening the effective distance between two points due to the creation of tortuous percolation pathways while reducing the number and effective cross-sectional area of these pathways [193]. The conductivity will decrease to zero when the domains become detached. Six nickel films prepared from pure as well as capillary suspensions were dried but not sintered to test the impact of cracking on the conductivity as shown in Fig. 46. Thinner films, both without cracks, with a thickness near 130 µm had similar conductivities ($\sigma_{S=0.00} = 8.9 \pm 0.1 \times 10^{-5}$ Sm-1 and $\sigma_{S=0.05} = 1.1 \pm 0.1 \times 10^{-4}$ Sm-1). As the film thickness increases, the conductivity should also increase due to the increasing effective conductive area. This increase is clearly shown in the films made from capillary suspensions where the conductivity increases linearly with the film thickness. The increase is also demonstrated for the intermediate thickness film made from the pure suspension ($h_{S=0.00} = 166 \pm 9$ µm, $\sigma_{S=0.00} = 1.2 \pm 0.1 \times 10^{-4}$ Sm^{-1}). However, the conductivity remains unchanged for the thicker film ($h_{S=0.00} = 227 \pm 14$ µm, $\sigma_{S=0.00} = 1.4 \pm 0.1 \times 10^{-4}$ Sm^{-1}). This is due to the development of cracks in the film without added liquid at a critical cracking thickness (CCT) between 160 and 200 µm. These cracks did not extend through the entire thickness of the film, but still increase the effective conductive pathway. As such, this thicker film did not show the same increase in the conductivity as the crack free films made from capillary suspensions.

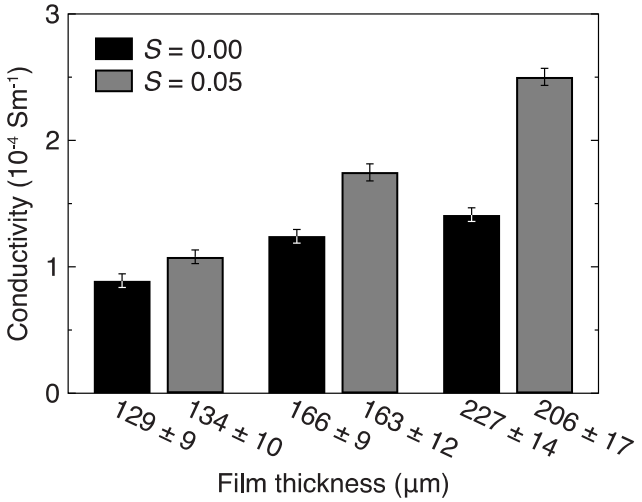

Fig. 46: Conductivity for unsintered nickel films at three thicknesses both without and with added liquid. The conductivity increases appreciably for the films produced from capillary suspensions as a function of the film height due to the increase in the area of the conductive pathway. This measured conductivity is lower for the films made from pure suspensions due to the partial cracking occurring in this case when the thickness exceeds 180 µm. *Reproduced with permission from ACS Applied Materials and Interfaces.*

5.3 Conclusions

We have demonstrated a route to create crack-free particulate films with minimal processing and material cost just by adding small amounts of a secondary liquid to a suspension thus introducing capillary bridges between particles. Microscopy images reveal a remarkable change in the crack pattern of dry films made from suspensions with varying amounts of secondary liquid for TiO_2, ZnO, $CaCO_3$ and Al_2O_3 systems with crack-free films produced at thicknesses at least five times greater than the critical cracking thickness measured for the suspension without added liquid. The reduction in cracking is caused by the bridges between particles causing a more homogeneous distribution of pore sizes, which prevents the strong anisotropic stress differences that cause cracking. Furthermore, the bridges between particles further reduce particle mobility and increase the drying rate of the bulk solvent next to the substrate. The observed reduction in cracking even persists after sintering as shown for the Al_2O_3 thick films. This ceramic sample is significant since the solvents and drying conditions are very different than the other samples. This implies that there is some resilience for the reduction in cracking depending on the drying conditions, but a more complete study should be undertaken.

This reduction in cracking improves the functionality of the films as demonstrated using membranes for filtration as well as conductive films. The filtration membranes with cracks demonstrated the same permeability as the porous substrate implying that liquid (and particles) can easily flow through the large cracks, which traversed the entire film thickness. This is further demonstrated with a filtration test. The membrane created from the capillary suspension, which did not exhibit cracking, was able to separate 1 µm particles easily, whereas the membrane made from the pure suspension could not even separate larger 5 µm particles. The formation of cracks also interferes with the conductivity of printed films. Cracks increase the percolation path length or can even prevent a direction connection between locations. This decrease in conductivity was shown for nickel films made form pure suspensions that in contrast to films made from capillary suspensions showed cracking at film thicknesses exceeding 180 µm. The experiments conducted with the TiO_2 capillary suspensions clearly showed that the maximum crack-free sheet thickness for capillary suspensions far exceeds the CCT measured without any capillary interactions.

While this research concentrated on systems without any chemical reactions, this research can also be applied to systems where reactions between the two fluids or between one of the fluids and particles take place. Experiments in systems where the secondary fluid is polymerized or crosslinked have also been conducted [41,194]. While the properties affecting the strength of the capillary interactions, i.e. interfacial tension and contact angle, are modified during this process,

a sample-spanning network of particles connected by the bridges is still present. In fact, this method can be combined with different chemical reactions, e.g. a reducing agent, which can be used to reduce the oxidation of conductive particles. The explicit effect of particle charge should also be investigated. Given the counteracting factors of charge on the capillary interaction and on the final particle packing, a thorough study of the charge on the strength of the capillary networks and on crack formation should be undertaken.

5.4 Author Contributions

M.S. designed and conducted the experiments with the TiO_2 and ZnO particles. J.M. designed the Al_2O_3 samples and conducted them with M.W. S.B.F. aided with the conductivity measurements. N.W. and E.K. supervised this project and helped interpret the results. All authors were involved in analysis of data and completion of this paper.

5.5 Funding Sources

No competing financial interests have been declared.
Financial support was provided from the German Research Foundation (Deutsche Forschungsgemeinschaft) grant agreement no. KO4805/2-1 and the European Research Council under the European Union's Seventh Framework Program (FP/2007--2013)/ERC Grant Agreement no. 335380.

5.6 Acknowledgement

We want to thank Dr. Sunyhung Kim for the fruitful discussions regarding the drying of suspensions and the stress development during drying. Special thanks also to Stefan Heissler for the support with the IR measurements. Financial support was provided from the German Research Foundation (Deutsche Forschungsgemeinschaft) grant agreement no. KO4805/2-1 and the European Research Council under the European Union's Seventh Framework Program (FP/2007--2013)/ERC Grant Agreement no. 335380.

6 3D printing of open-porous cellular ceramics with high specific strength

Full title: 3D printing of open-porous cellular ceramics with high specific strength

Authors: Johannes Maurath, Norbert Willenbacher

Status: published

Bibliographic data: Journal of the European Ceramic Society, 2017, in press
10.1016/j.jeurceramsoc.2017.06.001

Abstract

We present a novel processing route for manufacturing highly open porous, hierarchically structured ceramics via direct ink writing. We manufactured cellular samples with overall porosities up to 88 % that exhibit fully open-porous struts with porosities between 45-60 % and pore sizes $x_{50,3}$ < 6 µm using capillary suspension based inks. An innovative processing strategy enabled manufacturing crack-free, undeformed cellular ceramic samples.

We printed hexagonal honeycomb structures that showed exceptionally high specific strength under compression load and significantly enlarged the strength-density range that was covered by sintered capillary suspensions, so far. Without loss of mechanical strength the density of ceramic parts was decreased by about a factor of 2-3. Strength of in-plane and out-of-plane loaded hexagonal honeycomb structures varies according to common scaling laws for cellular structures. The honeycombs are mechanically more efficient than bulk specimens from capillary suspensions, since they show a distinctly lower sensitivity of strength on density.

6.1 Introduction

Highly porous ceramic materials with low density are extensively used in various technical applications, including filtration membranes for processes with hot or chemical reactive media, catalyst supports, energy storage systems, tissue-engineering scaffolds or lightweight

construction materials [6,195–197]. The structure of a porous material strongly determines its properties and this also defines the field of application. Generally, we can distinguish between open and closed porous structures, while open porous ceramics exhibit a high permeability with a high accessible surface area, and closed-porous structures show good thermal insulation properties [17,22]. Engineering materials with a tailored mechanical strength at low densities are often inspired by natural materials, like wood, weed or cancellous bone, that are hierarchically structured [19,198,199]. These materials consist of lattice-like architectures that define cells in the mm-range, while the struts may be porous as well with pores in the µm-range, or they are complex composite materials [18,198,200,201]. 3D printing is a common way for manufacturing ceramic structures with well-defined cell geometry in the mm-range, but controlling also the porosity in the struts is a great challenge up to now. This is especially valid for fully open-porous structures that are not only a high-strength structural ceramic, but also a functional material.

3D printing methods enable the fast and versatile manufacturing of prototypes, products at low number of units and tailor-made products. Next to ceramic parts [202,203], also polymers [204] and metals [202] and even food-products [205], are manufactured with 3D printing processes. However, 3D printing of ceramics is challenging due to complex process requirements. Typically, fabrication of dense ceramic components is addressed, but also porous ceramic materials are fabricated, especially for medical products like tailor-made implants or bone scaffolds [202,203,206,207], since these products cannot be manufactured economically via common processes like injection molding. A common 3D printing technique for porous ceramics is the so-called direct ink writing (DIW) where the desired body is assembled by specifically depositing small amounts of an ink or a paste [208]. This can be realized by a filamentary-based approach, like robocasting [202,209] and fused deposition modeling [203,209], or by a droplet-based approach, such as ink-jet printing [210,211].

Various processes are established for processing porous ceramic materials, including direct foaming, sacrificial templating, partial sintering, and using sacrificial fugitives [17,22]. Most of these techniques were originally developed for manufacturing macroporous bulk ceramics, but are partially combined with 3D printing techniques to achieve custom shaped, hierarchically structured ceramics. Porous calcium phosphate granules have been used in combination with a sugar solution as organic binder to fabricate scaffold structures suitable for bone tissue engineering with porous struts (microporosity 60%) via 3D printing. Quadratic grid structures with mesh sizes in the order of 150-750 µm were obtained. The overall porosity was about 75% and the mechanical compressive strength was below 1 MPa not suitable for carrying high loads [212]. Garcia et al. [213] have synthesized very complex scaffold materials with a hierarchical pore structure ranging from 4 nm to 400 µm. They combined a sol-gel process including a

surfactant providing the nm-sized pores, biopolymer sacrificial templating (methylcellulose) to achieve 30-80 µm pores, and direct ink writing of a suitable paste finally creating large 400 µm pores. In this case an overall porosity of about 40% was achieved. A printed structure including a regular arrangement of large pores with aligned microporous struts was obtained via 3D co-extrusion of a frozen alumina/camphene feed stock. The overall porosity of these scaffolds was 67-77% and the compressive strength varied between 10 and 30 MPa [214].

Direct ink writing processes also enable to create lightweight construction materials with distinct mechanical properties. Lewis et al. [200] reported about cellular structures made from fiber-filled epoxy resins with mechanical properties approaching the unique specific mechanical strength of balsa wood. This was accomplished due to the orientation of added silicon carbide and carbon fibers achieved during DIW and a distinct printed cellular structure. Another bio-inspired approach to obtain highly porous and high strength materials was presented by Fu et al. [215] Glass scaffolds with 60-80% porosity and a strength of 40-130 MPa under out-of-plane compression could be fabricated via DIW using a hydrogel based glass ink. However, in these latter approaches the printed struts did not include pores. Fabricating similar cellular structures with highly porous struts are an intriguing option to clearly enlarge the available specification range and to achieve lightweight materials with higher overall porosities and high specific strength. Recently, Muth et al. [201] as well as Minas et al. [18] published a concept for 3D printing hierarchically structured, lightweight ceramic solids with inks based on ceramic foams. Both authors used foams stabilized by surface modified Al_2O_3 particles. Muth et al. [201] presented cellular lightweight parts with closed-porous struts that exhibit a high specific stiffness [$> 10^7$ Pa/(kg/m³)] tailored by the printed geometry. In contrast, Minas et al. [18] printed struts with closed *and* open porosity but did not try to improve the mechanical efficiency due to tailored cellular structure. Specimens with an open-porosity between 83-94% and a compressive strength between 3-16 MPa were achieved.

Successful implementation of DIW processes for rapidly patterning complex 3D architectures crucially depends on the design of appropriate inks. According to the literature well printable inks should show a yield stress $\tau_y > 100$ Pa and storage modulus $G' > 10^4$ Pa [18,216]. Higher values of τ_y and G' are even better to achieve a high shape accuracy of the printed structures [200]. Paste like *capillary suspensions* with their high τ_y (> 200 Pa) [16,40], high G' (>10^5 Pa) [39] and strong shear thinning behavior [16] are a promising platform for designing DIW inks [18,200]. Recently Dittmann et al. [10,16] developed a versatile new processing route based on capillary suspensions as precursors for manufacturing highly porous and mechanically stable ceramics. Capillary suspensions are ternary fluid/fluid/solid systems with a strong particle network structure controlled by capillary forces. When a small amount of a second, immiscible fluid is added to the

continuous phase of a suspension, texture and flow of the admixture are dramatically altered due to the formation of a strong particle network within the suspension. Particles stick together due to capillary forces induced by liquid bridges formed by the secondary fluid. This phenomenon not only alters the rheology of the system, it also stabilizes the suspension. Settling is prevented since particles are trapped in the network [11]. Such capillary suspensions were successfully used as a precursor for manufacturing porous sintered materials [10,16,40,41]. The bulk fluid can be removed from the suspension without collapse of the particle network that forms the backbone of the subsequently sintered part, since the remaining liquid bridges between particles formed by the secondary fluid largely provide the integrity of the structure if the pair of fluids is chosen appropriately. Following thermal debinding and sintering steps transfer the highly open-porous precursor into sintered a part with a high porosity and a uniform pore structure. This new processing route gives access to a broad range of pore structures including previously hardly accessible porosity and pore size ranges (porosity $\varepsilon > 50\%$, median pore diameter by volume $x_{50,3} < 10\mu m$) with a very high repeatability regarding pore structure.

In this article we report about development of ceramic capillary suspension based inks for filament based DIW. We discuss sample preparation and composition providing stability, homogeneity and rheological properties enabling a stable DIW process. Then a method to transfer the printed specimen into sintered parts. Especially the latter step is the most crucial one since crack-formation and deformation during drying has to be prohibited for mechanical stable and functional sintered parts. We manufactured cellular structures in the shape of log-piles as well as hexagonal honeycombs. The first were primary for evaluating printing behavior while the latter were for mechanical testing. The nature inspired hierarchical, honeycomb structure promises excellent mechanical strength at low density.

6.2 Experimental procedure

6.2.1 Raw materials

Commercial grade aluminum oxide (α-Al_2O_3) particles were obtained from Almatis GmbH (CT3000SG) and Sumitomo Chemical (AKP-50). The average particle size according to the manufacturer is $x_{50,3} = 0.5$ µm for CT3000SG and $x_{50,3} = 0.2$ µm for AKP-50. Both particle types have a density of $\rho = \sim 3.9$ g/cm³ and exhibit an arbitrary, isometric shape. .

As bulk phase we used a mixture of highly liquid paraffin ($\eta = 0.035$ Pa s, $\rho = 0.85$ g/cm³; Merck KGaA), odorless mineral spirits ($\rho = 0.752$ g/cm³; Sigma-Aldrich) and palm wax ($\rho = 1.0$ g/cm³; Candle Wiz; received from A.C. Moore, Somerville, USA). The composition of the bulk phase

was: 48.6 vol% paraffin, 50.3 vol% mineral spirits and 1.1 vol% palm wax. The wax was dissolved in the two liquid phases by mixing the components in a planetary mixer (Speedmixer DAC 600.2; FlackTek Inc.) for 10 min at 2350 rpm. The melting temperature of the palm wax is T_m = 80-87°C. The bulk phase mixture has a surface tension of Γ_s = 25.4 ± 0.2 mN/m.

The secondary phase was a mixture of 50 vol% D(+)-sucrose (Carl Roth) in pure water. The aqueous sucrose solution has a surface tension of Γ_s = 77.3 ± 0.1 mN/m.

We determined the three-phase contact angle θ_{SB} of the secondary fluid towards the α-Al_2O_3 particle surface using the Young-Duprée equation [29] with the surface tensions of the surrounding bulk phase Γ_{Ba} = 25.4 ± 0.2 mN/m and the secondary phase Γ_{Sa} = 77.3 ± 0.1 mN/m, the interfacial tension of the two fluids Γ_{SB} = 28.3 ± 0.3 mN/m, and the contact angles of the fluids on Al_2O_3 against air θ_{Sa} = 55 ± 3° and θ_{Ba} = 0°. The calculations result in a three-phase contact angle of θ_{SB} = 47 ± 9°. Thus, the secondary phase preferentially wets the alumina particles and the capillary suspensions within this work are in the pendular state [11].

6.2.2 Sample preparation, printing, and sintering procedures

Suspensions were prepared by mixing alumina particles into the bulk phase in a planetary mixer. We mixed a sample volume of 50 ml in 100 ml cups for 1 min at 800 rpm and 2 min at 2000 rpm. Subsequently, the secondary fluid was added and the suspension was mixed for 2 min at 2000 rpm. The emerging capillary suspension was homogenized for 14-20 h in a ball mill (long roll jar mill; US Stoneware) to prevent agglomerates. We used spherical grinding media with 25 mm ball diameter (zirconia balls; Inframat Advanced Materials). Solids content of suspensions with CT3000SG and AKP-50 particles was ϕ_{solid} = 31 vol% and ϕ_{solid} = 23 vol%, respectively. The ratio of secondary liquid to solid volume was ϕ_{sec}/ϕ_{solid} = 0.165 for capillary suspensions based on CT3000SG particles and ϕ_{sec}/ϕ_{solid} = 0.1 for suspensions based on AKP-50 particles.

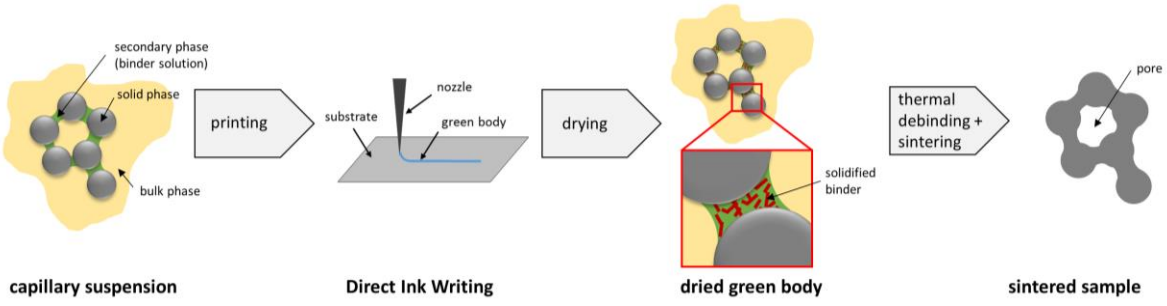

Fig. 47: Flow sheet of the processing route for direct ink writing of capillary suspension based inks. The open-porous structure of the sintered filaments is based on the open-porous network of capillary suspensions that serve as precursor for the ceramic part. *Reproduced with permission from Elsevier.*

Fig. 47 shows the processing steps for manufacturing ceramic structures via filamentary based direct ink writing. The capillary suspensions were extruded through tapered nozzles (inner diameters of: 200 µm, 250 µm, 610 µm; Nordson EFD). A syringe pump (PHD Ultra; Harvard Apparatus) was mounted on a custom made 3D positioning station (ABG 10000; Aerotech Inc.) for extruding the inks at a constant volumetric flow rate. 10 ml syringes (with Luer-Lok tip; BD) were loaded with the capillary suspension based ink and installed on the syringe pump. For loading syringes with bubble-free ink we opened the back of the syringe and loaded it with ink using a spatula. After each portion of added material fitful movements of the syringe (e.g. hitting the syringe slightly towards the edge of a table) forwarded the ink to the syringe tip without entrapped air bubbles. This is possible due to the high degree of shear thinning of capillary suspension type pastes. For translation in x-y-z direction the positioning station was programmed, while the syringe pump enabled printing at constant volumetric flow rate. Printing parameters, i.e. translation velocity and volumetric flow rate, are summarized in Table 5.

Table 5: Printing parameters for different ink compositions and nozzle diameters.

composition	nozzle diameter	translation velocity	volumetric flow rate
CT3000SG, ϕ_{sec}/ϕ_{solid} = 0.165	200 µm	42 mm/s	0.5 ml/min
CT3000SG, ϕ_{sec}/ϕ_{solid} = 0.165	250 µm	40 mm/s	0.5 ml/min
CT3000SG, ϕ_{sec}/ϕ_{solid} = 0.165	610 µm	55 mm/s	1.2 ml/min
AKP-50, ϕ_{sec}/ϕ_{solid} = 0.1	610 µm	55 mm/s	1.2 ml/min

The capillary suspension based inks were printed on rectangular glass slides (75x50 mm), coated with a thin layer of polyethylene glycol (PEG 1500, Sigma-Aldrich). For a homogeneous PEG layer the glass slides as well as the polyethylene glycol were heated up to T = 90°C, and afterwards the PEG was spread with a razorblade to a smooth and homogeneous layer. We printed so-called log-pile structures as well as cellular honeycomb structures on the coated glass slides. The log-pile structures had dimensions of 25x25 mm in green state and consisted of 10-16 printed layers. These structures are excellent test structures to evaluate the printing behavior of an ink, since they consist of many spanning elements that break due to deliquescence or bend strongly if the rheological properties of the ink are not appropriate. The log-pile structures

were printed with nozzle diameters of 200, 250 and 610 µm. Cellular honeycombs were printed with 200 and 610 µm nozzles and had dimensions between 23x34x8 mm and 60x40x8 mm in green state. The honeycomb structures consisted of 10-20 printed layers. To control the overall porosity of the structures we varied the number and size of the hexagonal cells. The honeycomb structures typically exhibited between 8 and 50 hexagonal cells. Fig. 48 exemplarily shows a green body on a glass slide coated with PEG.

After printing of the ceramic specimen was finished the PEG layer was wetted with pure water around the sample as well as in the pores. Fig. 48 shows this step schematically. Afterwards, the green body was dried in a laboratory oven at T = ~94°C for 15 min. This allows for evaporation of the mineral spirit in the bulk phase of the specimen and leads to a strong decrease of the palm wax solubility in the bulk phase. Even a small temperature drop below the melting point (80-87°C) of the wax immediately induces crystallization. The slippery PEG/water layer enables the sample to shrink in the xy-plane and prohibits adhesion on the substrate during drying. After drying the green body was exposed to room temperature for 30-60 sec allowing for crystallization of the palm wax in the residual bulk phase. The specimen were stable enough to move them gently onto a porous ceramic sintering plate, while the slippery PEG/water layer was still liquid and served as lubricating film.

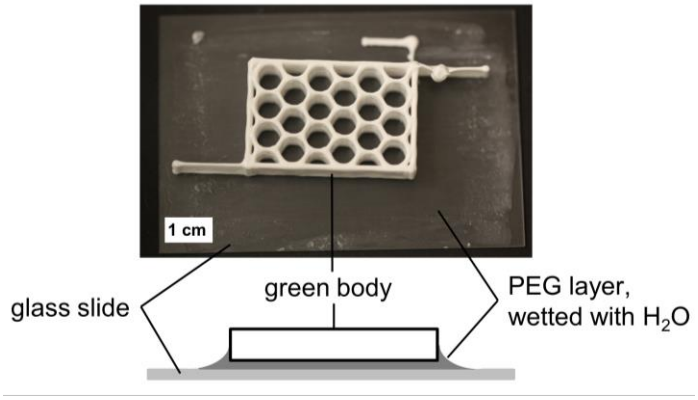

Fig. 48: Top view image of a green body. The specimen is printed on a glass slide coated with polyethylene glycol (PEG 1500). The PEG layer was wetted with pure water before the drying step was performed in a laboratory oven at T = ~94°C for 15 min. The schematic side view shows the printed body, the lubrication layer and the support during drying. *Reproduced with permission from Elsevier.*

Organic binder components in the green bodies were burned out in a debinding furnace. The samples were heated from room temperature to 200°C at a rate of 2°C/min. Subsequently, the temperature was held constant for 1 h at 200°C. Afterwards, the temperature was increased to 700°C with 1°C/min and was held for 1 h at 700°C. Finally, the oven was cooled down to 400°C

with 1.5°C/min. After 15 min at a constant temperature of 400°C, the oven was further cooled down to room temperature without temperature regulation.
For sintering we used a custom made high temperature furnace. Sintering temperatures were between 1200 and 1400°C. The furnace was heated up to the sintering temperature at 3°C/min. The final temperature was held constant for 2 h. Subsequently, the furnace cooled down to 50°C at 2°C/min.

6.2.3 Measurements

Rheological measurements were performed with a stress-controlled rheometer (Haake Mars II, Thermo Fisher Scientific, Karlsruhe, Germany). Plate-plate geometry (upper plate: titanium, lower plate: stainless steel) with a diameter of 35 mm was used. Both plates were rough (sandblasted surface) to prevent wall slip. The experiments were conducted at a gap height of 1 mm at T = 20°C.
Porosity of the struts ε_s of the sintered cellular specimen was determined using the Archimedes' principle according to DIN EN 993-1. True porosity of the cellular ceramics ε^* was calculated from sample dimensions and sample weight.
Dimensions of printed struts and pores in green bodies and sintered parts were determined via manual image analysis using a light microscope.
Scanning-electron-microscope (SEM) micrographs (S-4500; Hitachi High-Technologies Europe GmbH) of the surface and of the crosscut of sintered parts were used to analyze their microstructure. Pore size was calculated via image analysis using the Line Intercept Count Method [36]. Therefore, SEM micrographs of sample cross sections were examined. To prepare appropriate cross sections of sintered parts we infiltrated them with epoxy resin, cured the resin at elevated temperature (70°C for 20h), and grinded and polished the specimens afterwards.
For compressive strength tests the honeycomb structures were grinded to a fully flat surface. Preliminary tests confirmed that vertical boundaries do not affect mechanical strength, so we did not remove these parts from all specimens. Compressive strength tests of cellular honeycombs were performed with material testing machines (Zwick Roell). The samples were loaded displacement controlled at a rate of 0.05 mm/s for the 10 kN load cell (machine model: ProLine Z010) and 0.05 mm/min for the 300kN load cell (machine model: Zwick 300) until they failed.

6.3 Results and Discussion

6.3.1 Rheology

We observed gel-like, pasteous behavior and a high yield stress in capillary suspensions based on CT3000SG and AKP-50 particles. Texture and gel-strength of the suspensions change strongly with addition of the secondary liquid. Fig. 49 shows the texture of a pure suspension and an appropriate capillary suspension. The latter keeps the shape without any deliquescence and it consequently shows excellent printing behavior.

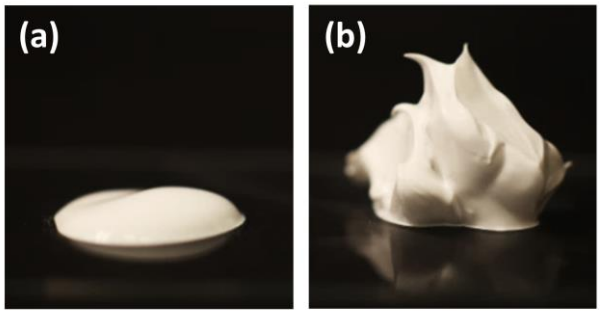

Fig. 49: Image of (a) a freely flowing pure suspension (ϕ_{solid} = 31 vol%, ϕ_{sec}/ϕ_{solid} = 0) and (b) a capillary suspension (CT3000SG, ϕ_{solid} = 31 vol%, ϕ_{sec}/ϕ_{solid} = 0.165) based on CT3000SG particles. Paste (b) shows excellent printing behavior. *Reproduced with permission from Elsevier.*

Rheological measurements proofed the gel-like behavior of both suspensions. We performed oscillatory shear experiments for pure suspensions as well as capillary suspensions based on the alumina powders CT3000SG and AKP-50. Paste composition was adjusted such that suspensions from both material systems show similar rheological and hence similar printing behavior. Due to the smaller size of AKP-50 particles a lower particle volume fraction was sufficient compared to the CT3000SG system to get suspensions as well as capillary suspensions with similar properties [35]. A solids content of ϕ_{solid} = 31 vol% for CT3000SG and ϕ_{solid} = 23 vol% for AKP-50 based suspensions was chosen. Furthermore, the ratio of secondary liquid to solid volume was set to ϕ_{sec}/ϕ_{solid} = 0.165 and ϕ_{sec}/ϕ_{solid} = 0.1 for capillary suspensions based on CT3000SG and AKP-50 particles, respectively.

Fig. 49a exemplarily shows the storage and loss moduli, G' and G'', for the CT3000SG based suspension with and without added secondary fluid. In both cases the moduli are independent of frequency in the whole investigated range (ω = 0.1 – 100 rad/s) and G' is about one order of magnitude larger than G''. Adding the secondary fluid, however, results in a transition from a weak to a strong gel with an almost three orders of magnitude increase in modulus (from 10^3 Pa

to 10^6 Pa). Similar results were fund for the AKP-50 based system (G' increased from 10^3 Pa to 10^6 Pa).

The yield stress τ_y is an important indicator for evaluating the printing behavior of a paste since pastes with high yield stress are less prone to deliquescence of printed filaments [18,200]. We determined the yield stress τ_y of the suspensions via oscillatory shear amplitude sweep measurements at a constant frequency of $\omega = 1$ rad/s. Fig. 50 exemplarily shows the data for the CT3000SG particle based system. At a certain stress amplitude G' and G'' drop drastically from the plateau in the linear viscoelastic regime (LVE). This drop indicates the transition of the suspension from solid to fluid-like behavior [39]. We define a drop of G' for more than one decade compared to the plateau in the LVE regime as the criterion to determine the onset of yielding and the corresponding stress amplitude value is treated as the apparent yield stress τ_y. For CT3000SG particles the yield stress of the pure suspension is $\tau_y = 8.8 \pm 2.5$ Pa and of the capillary suspension $\tau_y = 2287 \pm 157$ Pa. For AKP-50 suspensions the yield stresses are $\tau_y = 5.1 \pm 1.6$ Pa and $\tau_y = 2131 \pm 148$ Pa, respectively. The yield stress of the capillary suspension is for both material systems more than two orders of magnitude larger than that of the corresponding pure suspension.

These results are in agreement with prior works on capillary suspensions [28,35]. The high yield stress and storage modulus values for the capillary suspensions result from the strong percolating particle network consisting of capillary bridges that is much stronger than the van der Waals network that is predominant in the pure suspensions. In steady shear experiments we observed a strong wall-slip for the capillary suspension based inks. Furthermore, capillary suspensions are known to exhibit strong shear thinning [10,15,40] and an immediate structural recovery after shearing [28]. These rheological features are ideal prerequisites for 3D printable pastes that can be extruded easily through small nozzles, and at the same time lead to stable extruded filaments without uncontrolled deliquescence, due to the high τ_y and G' [18,200,201,216].

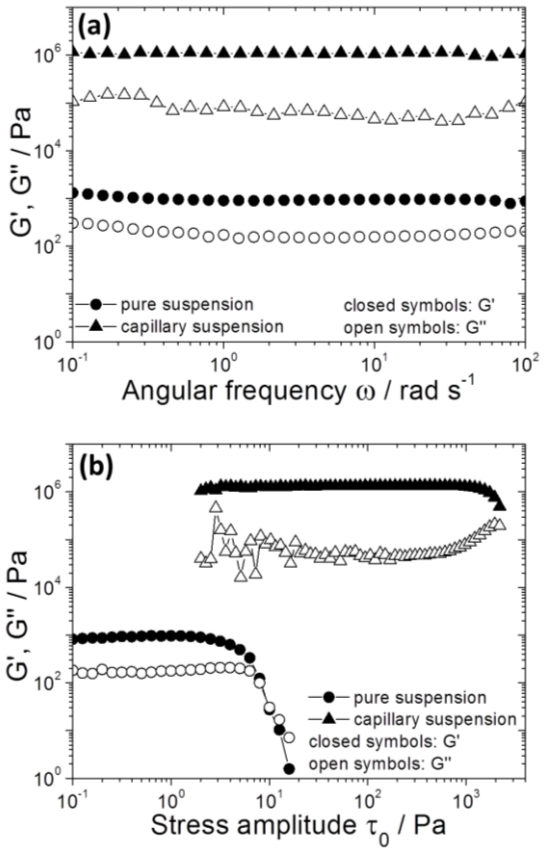

Fig. 50: Rheological data from oscillatory shear experiments of a pure suspension (CT3000SG, ϕ_{solid} = 31 vol%, ϕ_{sec}/ϕ_{solid} = 0) and a capillary suspension (CT3000SG, ϕ_{solid} = 31 vol%, ϕ_{sec}/ϕ_{solid} = 0.165). (a) Storage modulus G' and loss modulus G'' are plotted vs. angular frequency ω. Stress amplitude τ_0 was 0.5 Pa for the pure suspension and 10 Pa for the capillary suspension. (b) Storage modulus G' and loss modulus G'' plotted vs. shear stress amplitude τ_0 at fixed angular frequency ω = 1 rad/s. *Reproduced with permission from Elsevier.*

6.3.2 Hierarchical ceramics

We printed cellular log-pile structures as well as honeycomb structures with capillary suspension based inks including AKP-50 and CT3000SG particles. Log-pile structures were printed for judging the printing behavior of the pastes. These structures exhibit tiny spanning elements and thus they are common in ink development for testing on deliquescence and stability of printed filaments from DIW processes. Fig. 51 shows a schematic of these printed structures that consist of multiple layers of printed filaments where the filaments of each layer are perpendicular to that of the layer below. Capillary suspension based inks showed good behavior for extruding thin filaments through small nozzles (200-610 µm) without unwanted deliquescence, while printing of pure suspensions was not feasible at all. Extruded filaments did not hold shape and deliquesced instantly. With capillary suspension based inks it was possible to create spanning elements that bridge up to 2 mm.

Accuracy in shape for pores in the xy-plane was excellent for capillary suspensions printed with all tested nozzle diameters. Printed pores in the xy-plane had dimensions between 490 – 570 µm. For pores in the xz- and yz-plane the print quality differed depending on the selected nozzle diameter. Prints from 200 and 250 µm nozzles partially exhibited closed pores, while all prints from the 610 µm nozzle were excellent. The worse print quality with decreasing nozzle diameter may result from material overflow at the nozzle during extrusion. This results from too high volumetric flow rates of the inks or too low translation velocities of the nozzle. We monitored this material overflow by measuring the strut width of green bodies with a light microscope and related this to the nozzle diameter. Dried green bodies (drying conditions: 94°C, 15 min, cf. Fig. 48) from CT3000SG suspensions that were printed with the 250 µm nozzle had strut widths of 490.5 ± 33.1 µm, while samples from 610 µm nozzles had strut widths of 634.5 ± 44.4 µm. The ratio of dried strut width to nozzle diameter is for small nozzles nearly twice as high as for the larger nozzles. However, further iteration of printing parameters is necessary to reach good printing results for feature sizes ≤ 250 µm.

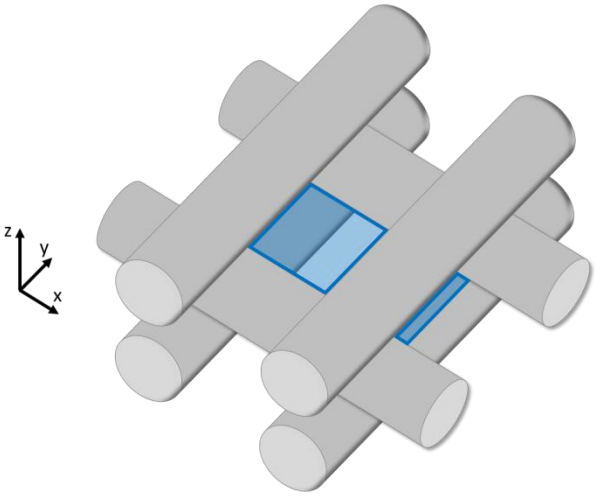

Fig. 51: Schematic of the printed log-pile structures. Blue shaded areas mark the printed pores. *Reproduced with permission from Elsevier.*

Furthermore, we printed hexagonal honeycomb structures for lightweight construction materials mimicking natural materials with high specific mechanical strength, like wood [198]. These structures were used for mechanical tests, later on. Capillary suspension based inks were printed with 200 µm and 610 µm nozzles. The honeycombs exhibit large aspect ratio structures with wall height to width ratios in range of 4 to 11. Typically, wall thicknesses were 0.7-1.5 mm and heights 6-8 mm. The large aspect ratio structures did not show any deformation resulting from deliquescence.

All cellular green bodies were dried, thermally debinded and sintered. The samples shrank uniformly (10 - 26%) during the debinding and sintering process and did not show any macroscopically visible defects or deformations, as shown in Fig. 52. The small filaments poking out of the log-pile structures (top right of Fig. 52a) show the end point of 3D printing, where the nozzle departs from the specimen with high velocity. The filaments poking out of the cellular honeycombs (top right and bottom left of Fig. 52c) result from the chosen 3D printing procedure that includes additional print paths and dwell times for each printed layer, this procedure prevents nozzle clogging and guarantees high printing quality.

Flawless cellular honeycomb specimens were manufactured up to green body dimensions of approximately 60x40x8 mm with true porosity in a range of ε^* = 60-88%. True porosity ε^* of the cellular structure was varied by changing cell size, cell number, sample dimensions and sintering conditions, which directly impact the strut porosity ε_s.

Strut porosity ε_s as well as shrinkage of the cellular samples were controlled by the sintering temperature. Both parameters occurred to be independent of printed geometry or nozzle diameter, indicating that the microstructure of the ceramic is not affected by the printing process. Porosity measurements confirmed that the struts are fully open-porous in agreement with previous work on capillary suspension based porous sintering materials [10,16,40,41]. Fig. 53 shows how strut porosity decreases with increasing sintering temperature, while shrinkage of the samples increases in xy-plane. The strut porosities were in a range of ε_s = 59.5 ± 0.5% and 45.7 ± 1.8% for sintering temperatures between 1200 and 1400°C. Shrinkage in the xy-plane was between 10 and 26%. Up to a sintering temperature of 1300°C porosity and shrinkage barely vary. For T > 1300°C, however, sintering is strongly accelerated and porosity strongly decreases while shrinkage increases substantially.

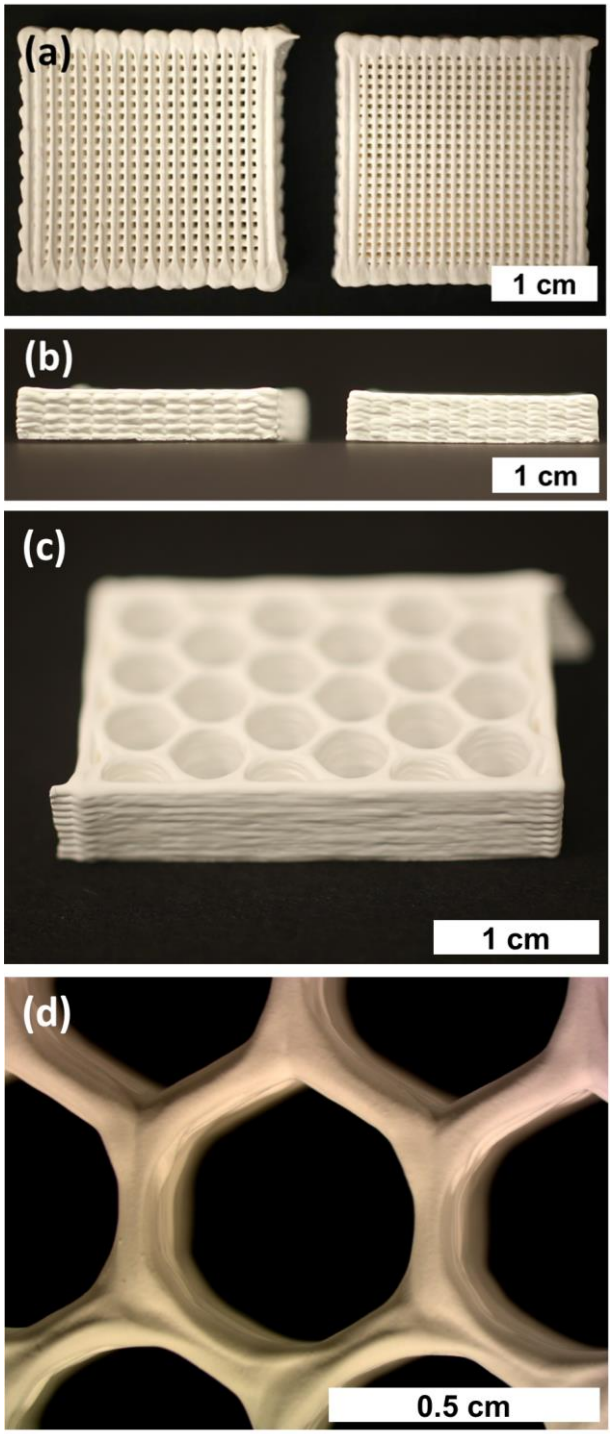

Fig. 52: Images of sintered cellular specimens from capillary suspensions based on CT3000SG powder. (a) Top view of a log-pile structure printed with a 610 µm nozzle (left) and a 250 µm nozzle (right). Printing parameters are summarized in Table 1. Geometrical settings for the structure shown on the left: distance between adjacent filaments = 1830 µm (= 3 x nozzle diameter), layer height = ~730 µm (= 1.2 x nozzle diameter); geometrical settings for the structure on the right: distance between adjacent filaments = 1000 µm (= 4 x nozzle diameter), layer height = 300 µm (= 1.2 x nozzle diameter). (b) Side view on the two log-pile structures. The sintered bodies show no deformation and are free of cracks. The left sample consists of 10 printed layers, the right one of 16. (c) And (d) are hexagonal honeycomb structures, printed with a nozzle diameter of 200 µm. Sintering conditions: T_s = 1300°C, 2h. *Reproduced with permission from Elsevier.*

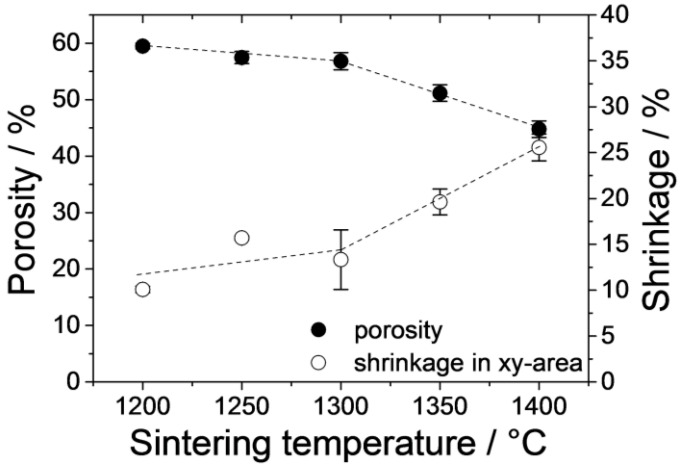

Fig. 53: Strut porosity ε_s and shrinkage in xy-plane vs. sintering temperature (t = const. = 2 h) of specimens printed with different nozzle diameter (200-610µm). The data shown are average values of at least 3-5 honeycombs or log-pile structures. The samples are made from CT3000SG particles. Strut porosity measurements were performed according to DIN EN 993-1. *Reproduced with permission from Elsevier.*

As mentioned earlier the sintered cellular parts are flawless and do not show any defects, even microscopically. Top view SEM images of the samples, Fig. 54a and b, show a smooth and crack-free surface of the printed filaments that are well connected to perpendicular filaments on the layer below. Even at the junctures no cracks are visible. The higher magnification in Fig. 54b reveals the open-porous surface of the filaments and a homogeneous, narrow pore size distribution. SEM images of crosscut sections, Fig. 54c and d, are better to visualize the microstructure of the porous struts. Fig. 54c shows a crosscut of a log-pile sample that was printed with a nozzle diameter of 610 µm. The cross-cut filaments are nearly circular in shape and the printed pores in xy- and yz-plane (cf. blue shaded areas in Fig. 51) are fully open. Fig. 54d shows a crosscut of a porous strut at a higher magnification. The pore structure of the sintered struts is similar to that of typical capillary suspension based moulded glass [40] or ceramic membranes [10,16,41]. We determined the pore size distribution of sintered struts via SEM image analysis of cross sections. Table 6 summarizes the $x_{50,3}$ as well as $x_{10,3}$ and $x_{90,3}$ values for samples based on CT3000SG and AKP-50 particles sintered at different sintering temperatures T_s. The average pore size $x_{50,3}$ as well as the pore size distribution width ($x_{90,3}$ – $x_{10,3}$) of CT3000SG samples changes from $x_{50,3}$ = 5.3 ± 0.7 µm at T_s = 1200°C to $x_{50,3}$ = 4.8 ± 1.0 µm at T_s = 1400°C, consistent with decrease in porosity from 59.5 ± 0.5% to 45.7 ± 1.8% shown in Fig. 53. At constant sintering conditions (T_s = 1300°C, 2h) the ink based on the smaller AKP-50 particles yields a smaller average pore size of $x_{50,3}$ = 1.9 ± 0.6 µm (compared to $x_{50,3}$ = 4.8 ± 1.0 µm for the CT3000SG system) as expected [16], while the relative width of pore size distribution, $(x_{90,3}-x_{10,3})/x_{50,3}$ = 1.32 and 1.58, respectively, and porosity are almost the same.

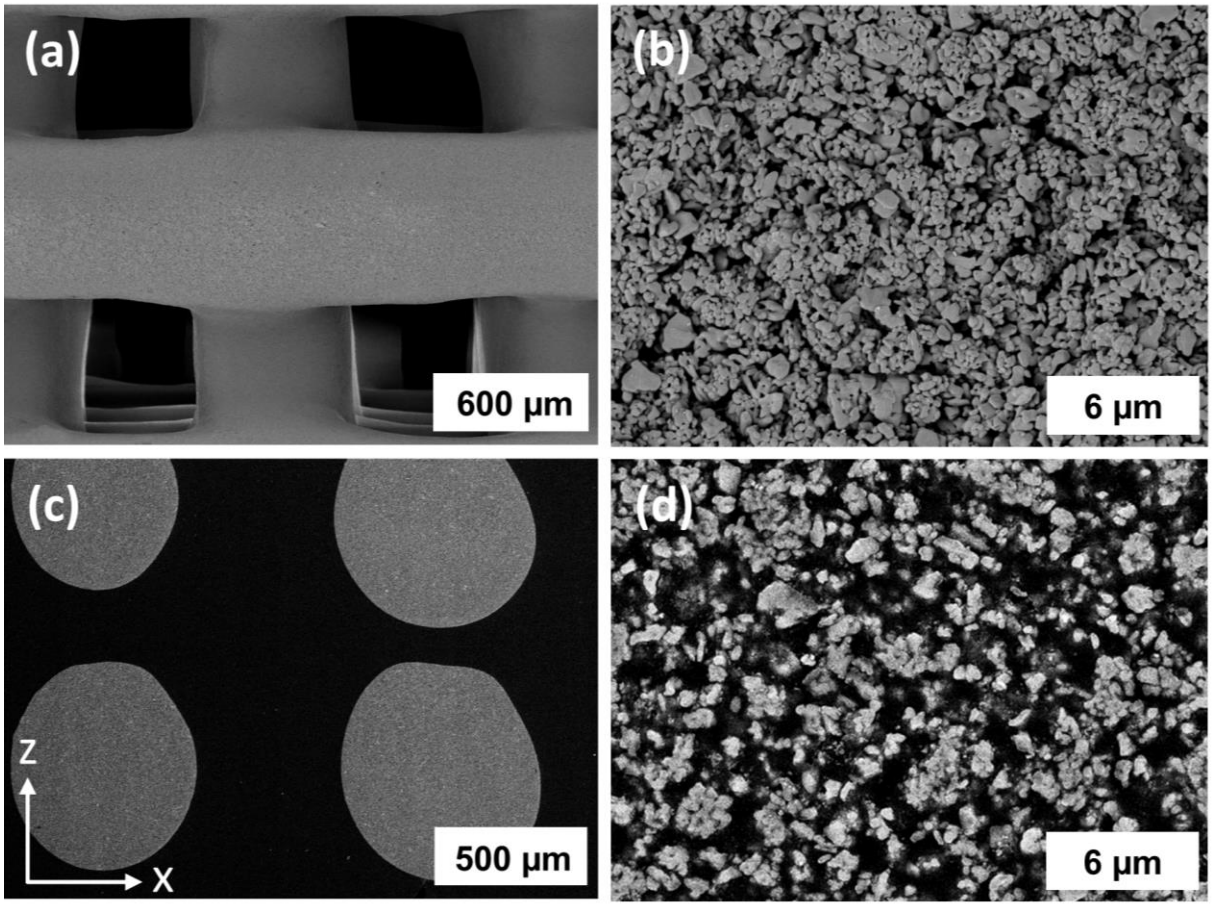

Fig. 54: SEM images of sintered log-pile structures based on capillary suspensions from CT3000SG particles, printed with a 610 µm nozzle. (a) Top view and (b) magnified surface of printed filaments. (c) Crosscut image of printed filaments. The coordinate system is equivalent to that in Fig. 5. (d) Crosscut image with the unique microstructure of sintered capillary suspensions. Sintering conditions: T_s = 1300°C, 2h. *Reproduced with permission from Elsevier.*

Table 6: Microstructural properties of sintered parts based on capillary suspensions.

material	**sintering conditions**	**strut porosity ε_s**	**pore size $x_{10.3}$**	**pore size $x_{50.3}$**	**pore size $x_{90.3}$**
Almatis, CT3000SG	1200°C, 2h	59.5 ± 0.5 %	2.4 ± 0.0 µm	5.3 ± 0.7 µm	8.3 ± 0.1 µm
Almatis, CT3000SG	1300°C, 2h	56.3 ± 1.6 %	2.4 ± 0.0 µm	5.7 ± 0.4 µm	10.0 ± 0.0 µm
Almatis, CT3000SG	1400°C, 2h	45.7 ± 1.8 %	1.8 ± 0.0 µm	4.8 ± 1.0 µm	9.5 ± 0.1 µm
Sumitomo, AKP 50	1300°C, 2h	55.4 ± 1.6 %	0.7 ± 0.1 µm	1.9 ± 0.6 µm	3.2 ± 0.2 µm

6.3.3 Mechanical properties

Compressive strength of a honeycomb structure is strongly influenced by the overall density ρ^* of the sample. Fig. 55 shows typical engineering stress-strain curves of selected samples with different ρ^*. The samples were loaded perpendicular to the cell orientation ("in-plane"). Structures consisted of 18 hexagonal cells and were printed with a 200 µm nozzle. Dimensions of all three samples were similar in the green state; the overall density ρ^* was varied by changing the sintering temperature. The initial non-linear increase in stress for strains < 0.015 may result from orientation of the experimental setup at low loads [217]. The stress-strain graph allows for calculating the Young's modulus E from the slope of the respective curve, but in this work we focus on the compressive strength σ^*, i.e. the maximum load that the sample can resist without fracturing.

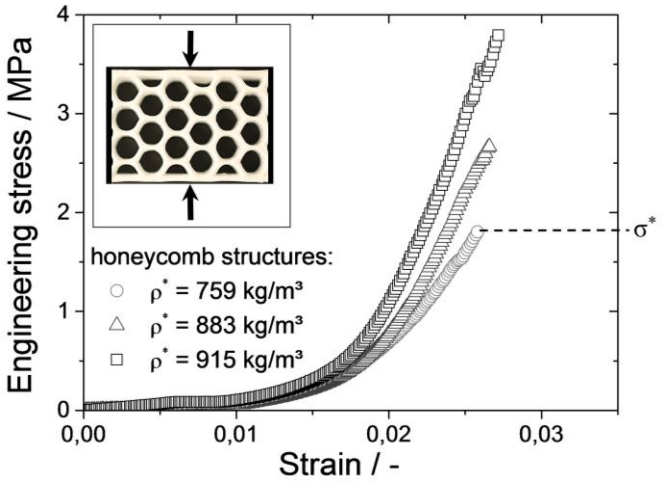

Fig. 55: Engineering stress vs. strain curves of honeycomb structures loaded perpendicular to cell orientation in compression test. The dashed line exemplarily indicates the compressive strength σ^* (i.e. stress at failure) for one sample. The insert schematically shows a honeycomb in compression test. *Reproduced with permission from Elsevier.*

The honeycomb structures printed here show superior mechanical strength at low relative density ρ^*/ρ_m (with m for matrix, i.e. here Al_2O_3 with ρ_m = 3.9 g/cm³) compared to slip-cast beams of sintered capillary suspensions made from Al_2O_3 [16] and glass [40] as well as to other open-porous ceramics manufactured via 3D printing processes [212–214,218]. Fig. 56a shows the compressive strength σ^* of the specimens normalized to the tensile strength of the matrix material $\sigma_{ts,m}$, thus excluding material specific differences in strength vs. relative density ρ^*/ρ_m. For the honeycomb structures, σ^* is only a function of ρ^*, and not of sample geometry (number and size of cells, sample dimensions) varied to change overall density. The honeycombs show equal relative strength $\sigma^*/\sigma_{ts,m}$ at lower relative density ρ^*/ρ_m compared to most ceramics from

3D printing processes that show open-porous struts [212–214,218]. Only the recently published results for 3D printed, open-porous alumina foams from Minas et al. [18] showed a higher specific mechanical strength. This might be due to a more round and thus smoother pore shape of these latter parts. Our ceramic honeycomb structures based on capillary suspensions even reach the relative strength to relative density range that is covered by wood [198], which is a highly appreciated lightweight construction material, at least under in-plane load. However, wood gains its high mechanical strength from the strong cell walls and the strength gain due to the cellular structure is lower than for ceramic structures. As shown in Fig. 56b, considering absolute values the specific strength of the ceramic honeycombs fabricated from capillary suspensions approach that of Balsa wood, the prime example of wood with high specific strength [198,200]. However, other cellular structures manufactured in 3D printing processes exhibit distinctly higher specific strength than the open porous ceramics presented here, but in all cases their struts are either dense or of closed porosity [18,215,217,219,220]. Instead, 3D printed open porous structures offer additional opportunities with respect to filtration or catalysis applications.

With the cellular structures obtained from 3D printing we decreased the overall density ρ^* of sintered capillary suspensions by about a factor of 2-3 compared to uniform bars or disks without losing mechanical strength. Relative densities ρ^*/ρ_m of the cast beams and 3D printed honeycomb structures are in the range of 0.3-0.56 (ρ^* = 1200-2200 kg/m³) and 0.12-0.25 (ρ^* = 490-1000 kg/m³), respectively. Overall porosities ε^* are between 43-70% and 75-88%. Exemplarily picking a honeycomb structure loaded perpendicular to cell orientation (“in-plane”) with a density of ~790 kg/m³, this specimen shows the same compressive strength of ~3 MPa as a slip-cast specimen with a clearly higher density of ~1330 kg/m³. This effect gets even stronger when we load the honeycomb structures parallel to cell orientation (“out-of-plane”). The structures behave highly anisotropic and a similar strength (~3 MPa) is achieved now at a density of only ~490 kg/m³. In turn, at a given density strength increases by a factor 2-3 comparing in-plane to out-of-plane loading.

As can be seen from Fig. 56b, the compressive strength of hexagonal honeycombs is well described by [19,198,199]

$$\frac{\sigma^*}{\sigma_{ts,s}} = C\left(\frac{\rho^*}{\rho_s}\right)^k \qquad (15)$$

where σ^* is the compressive strength of the honeycomb, $\sigma_{ts,s}$ is the tensile strength of the struts, ρ^* is the true density of the honeycomb, ρ_s is the strut density, and *C* and *k* are constants that depend on type of cellular structure and loading direction. For hexagonal honeycombs C = 1/3 while k = 2 and 1 for in-plane [198,199] and out-of-plane [19,198] loading, respectively. This

scaling model is based on the mechanisms of failure of hexagonal cellular structures under load. For in-plane loading these structures are nearly ideal bending-dominated lattices (k=2), while for out-of-plane loading they show ideal stretch-dominated behavior (k=1) [221]. Generally, stretch-dominated structures exhibit a higher stiffness and strength than bending-dominated structures. This anisotropic behavior is well-known for biological hierarchical cellular structures such as wood, weed or bones [19,198].

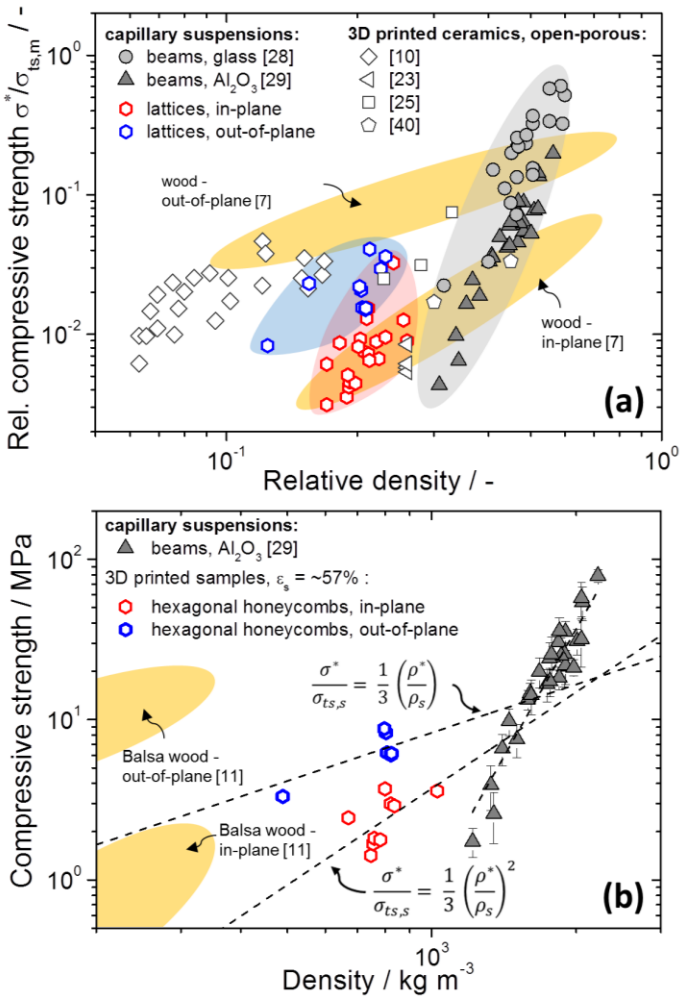

Fig. 56: Mechanical strength data of the 3D printed honeycomb structures. One data point represents the result of one tested sample in compression strength test. (a) Relative compressive strength vs. relative density for honeycomb structures and other 3D printed ceramics and glasses that exhibit fully open-porous struts [16,18,40,212,214,218]. The orange shaded areas show the characteristic rel. strength - rel. density range of wood [198]. (b) Compressive strength as a function of density. The graph shows data for honeycomb structures with constant strut porosity ε_s = ~57% and slip-cast specimens based on capillary suspensions from Dittmann et al. [16]. The dependence of strength on density for the 3D printed samples fits well to the scaling laws for in-plane and out-of-plane loaded hexagonal honeycomb structures [221]. The orange shaded areas show the characteristic strength - density range of Balsa wood [200]. *Reproduced with permission from Elsevier.*

Fig. 56b shows a set of data for hexagonal honeycombs with various overall densities ρ*, but constant strut porosity of ε_s = 57%, in a compressive strength versus density representation. The scaling law introduced in Eq. (1) with exponents k=2 for in-plane loaded specimens and k=1 for out-of-plane loaded specimens describes the dependence of strength on density very well. We focus on the scaling here, determination of the pre-factor C is not possible here, since this would require knowledge of the tensile strength of the porous struts $\sigma_{ts,s}$ not available so far. For porous ceramics this quantity is in general hardly accessible, since brittle materials tend to undefined stresses in the tensile test thus causing erroneous results. However, the term $\sigma_{ts,s}\ C\ \left(\frac{1}{\rho_s}\right)^k = C^*$ is constant if strut density ρ_s as well as tensile strength $\sigma_{ts,s}$ of the porous struts are constant [16], as it is the case here. From a fit of Equation (1) to the data in Fig. 56b we determine *C** and with ρ_s = 1694 kg/m³ (i.e. ε_s = ~57%) as well as C = 1/3 we estimate consistent tensile strength values $\sigma_{ts,s}$ = 31 ± 3 MPa and $\sigma_{ts,s}$ = 42 ± 3 MPa from the in-plane and out-of-plane data sets, respectively. This seems to overestimate the true tensile strength of the struts expected to be about a factor of 5 to 10 lower than the compressive strength [222] which in our case is ~20 ± 5 MPa [16].

However, the scaling laws describe the density dependence of mechanical strength of the hexagonal honeycomb structures very well. In both cases of loading, in-plane and out-of-plane, the 3D printed structures are mechanically more efficient than cast beams, strength of slip-cast samples is significantly more sensitive to a decrease of density than the lattice structures. This high mechanical efficiency of lattice structures was also reported by Minas et al. [18] and Muth et al. [201] who successfully used different ink compositions, emulsions and foams including ceramic particles, instead of capillary suspensions for direct ink writing of hierarchically structured cellular solids as well as by Compton et al. [200], who manufactured triangular honeycombs from organic composite materials.

6.4 Conclusions

We introduced a processing route for manufacturing hierarchically structured, highly open-porous cellular structures with high specific strength. We developed inks based on ceramic capillary suspensions that show excellent printing behavior for 3D printing cellular structures with high aspect ratios (height/width = 4-11) as well as small spanning elements. The ink concept is versatile and can be applied to a wide range of ceramic particles with different particle size, while rheological behavior of the ink can be adjusted easily according to printing and processing demands in a wide range. We successfully used a filamentary based direct ink writing technique for printing cellular ceramic structures with nozzle diameters ≥ 200 µm. An innovative processing

strategy enabled us to debind and sinter these filigree structures without crack formation or undesired deformation of the specimens. Hierarchically structured, cellular samples with overall porosities in the range of 60-88 % were produced. The printed struts are fully open porous (ε_s = 45-60 %) and show average pore sizes $x_{50,3}$ < 6 µm.

We printed ceramic hexagonal honeycomb structures that show exceptionally high specific strength compared to common capillary suspension based ceramics and to most 3D printed open porous ceramics from other processes. The overall density of the honeycomb structures is significantly decreased compared to slip-cast uniform samples, but the cellular structure still guaranteed a high mechanical strength in compression. Specific strength of the honeycomb structures is about a factor of 2-3 larger than the strength of cast specimens. Honeycomb structures behave anisotropic under compression load, and the compressive strength of in-plane loaded samples is about 2-3 times larger than that of out-of-plane loaded specimens. The obtained compression strength data are very well described by commonly accepted scaling laws.

The concept introduced here offers further opportunities for fabrication of cellular solids with even higher mechanical strength in the range of e.g. Balsa wood, one of the prime examples for natural cellular materials with unique specific strength [200]. Two promising strategies are to use the so-called smart capillary suspension concept [41] to reinforce the sintering necks in the porous struts finally resulting in a higher overall mechanical strength or to use capillary suspensions based on glass particles yielding smoother pore structure beneficial for high mechanical strength at low density [40].

Beyond that the open porous hierarchical structures spanning the length scales from 10^{-3} m to 10^{-7} m enabled by DIW of capillary suspension type ceramic inks may find application in separation and filtration processes, e.g. as microfluidic crossflow filters for hot gas filtration or as catalyst supports with smart flow channels for fast chemical reactions requiring high internal surface.

6.5 Acknowledgement

We would like to thank Jennifer A. Lewis and Joseph T. Muth from Harvard University for providing experimental assistance and fruitful discussion of the work. We would also like to thank the Karlsruhe House of Young Scientists for the financial support that included travel expenses and allowed for the collaboration between Karlsruhe Institute and Technology and Harvard University. We thank the Almatis GmbH for the donation of alumina particles as well as the smooth collaboration. Further thanks are given to Thomas Lebe for the support at the SEM-microscope.

7 Summary

In 2012 Dittmann et al. [110] introduced for the first time a processing route for manufacturing highly porous ceramics using so-called capillary suspensions as precursors. It allows for manufacturing macroporous sintered materials with a variable microstructure, ranging from a porosity - pore size range of $\varepsilon > 50\%$ at $x_{50,3} < 10$ µm up to sintered parts with a controlled, well-defined broad pore size distribution. Various scientific studies investigated the basics of capillary suspensions and also introduced the principle process using these three-phase suspensions as precursors for sintered materials. We present in this dissertation an experimental study on the tailored formulation of capillary suspensions for product applications that were not in the focus of other researchers, so far. The main results of this cumulative dissertation are divided into three parts.

In **part I** we investigated the impact of the particle shape on capillary suspensions in the wet state. So far, research neglected the influence of the particle shape and focused only on spherical or nearly isometric particles. We investigated capillary suspensions from particles with different shape and saw strong discrepancies in rheology and microstructure. For needle shaped or scalenohedral calcium carbonate particles no formation of a capillary network was observable. In contrast, for suspensions from spherical and plate-shaped particles we observed the characteristic three regimes in yield stress σ_y and storage modulus G' with varying secondary fluid content ϕ_{sec}. However, the three regimes of the two different types of particles are not identically pronounced and we assumed that capillary bridges between plate-like particles are of different shape and can accommodate much higher amounts of secondary fluid until spherical agglomeration sets in than e.g. spherical particles. Similar results were observed for spherical and plate-shaped graphite particles, as identified by a cooperating scientist. These results underline the strong influence and significance of particle shape for the tailored formulation of capillary suspension based products.

Part II of this thesis focused on the solid state of capillary suspensions. Solid specimens with an improved microstructure resulting in a high permeability and mechanical strength were processed and characterized. In *chapter 3* we developed and characterized highly porous glass membranes from capillary suspensions as precursors. The membranes had a narrow pore size distribution with average pore sizes between 1 – 50 µm at porosities ≥ 50 %. The development of this innovative manufacturing process results from the collaboration of several scientists, while the relevant conception, the implementation and, in particular, the optimization of the process for manufacturing outstanding filters stems from the author of this dissertation. These new glass membranes showed a smooth and homogeneous pore structure that result in a high

permeability and good mechanical properties. At given porosity the mechanical strength of the glass membranes were comparable to that of ceramics, even if these exhibit much higher matrix strength. Liquid and gas permeability tests showed that the permeability of the new glass membranes excel that of ceramic or commercial glass membranes, especially at pore sizes $x_{50,3}$ < 10 µm. The smooth pore structure and the homogeneity of the membranes are a clear advantage compared to benchmark products.

In *chapter 4* we introduced a new concept for manufacturing solid materials with excellent mechanical strength at high porosity. The concept can be used for a broad range of materials, ranging from polymers to ceramics. In a collaboration of several scientists we developed and applied the so-called *smart capillary suspension concept* in which the secondary liquid is used as carrier for active ingredients like reactive resins, solvents or small particles. The self-organized distribution of the secondary liquid in the capillary suspensions guarantees the presence of active ingredients exactly where these are needed: between the coarse particles that should be sintered, glued or fused. We introduced an example where a reactive resin is used as secondary fluid to glue plate-shaped graphite particles to highly porous membranes with excellent properties, regarding strength (up to 1 MPa) and pore structure (ε = 60-75 %, $x_{50,3}$ = ~15 µm). In a further example, that was solely conceived and conducted by the author of this thesis, we showed a strategy to manufacture membranes from UHMWPE particles. UHMPE is a type of polyethylene with particularly high molecular weight that is hardly to process to products. Using capillary suspensions of UHMWPE particles with an organic solvent (m-xylene or paraffin oil) as secondary phase allowed the production of sintered parts at a sintering temperature that was approximately ~40 K below that of conventional sintering processes. The sintered membranes had a smooth pore structure and high porosities > 62%. In a third approach, where the author of this dissertation participated in parts, the secondary liquid was used as carrier for a fraction of fine sinter-active particles. Porous ceramics with smooth pore structure and an exceptional high mechanical strength were manufactured at significantly reduced sintering temperature.

Part III introduced two applications of capillary suspensions: a processing strategy to produce crack-free coatings and a method for 3D-printing ceramic lightweight materials with hierarchical pore structure.

In *chapter 5* we examined the benefits of capillary suspension based formulations for thin film coatings that otherwise tend strongly to drying cracks. This concept allowed us to realize crack-free coatings with thicknesses that exceed the critical cracking thickness of appropriate pure suspensions significantly. The strong capillary network conserves particle cohesion and depending on the chosen secondary liquid it can even increase the drying rate. Thin films of

various ceramic and metallic particles were processed, dried and characterized. We were even able to transfer these crack-free films into sintered state, as shown for Al_2O_3 films. Coatings of Ni were tested on electric conductivity and sintered, porous Al_2O_3 films were tested on liquid permeability and filtration cut-off. Scientific results of this chapter are from excellent cooperation between multiple authors, like in previous chapters of this work. The investigations on thin films from Al_2O_3-particles were conceived and conducted nearly exclusively by the originator of this dissertation.

An innovative strategy for additive manufacturing of complex ceramic parts with hierarchical pore structure was inaugurated in *chapter 6*. We developed capillary suspension based inks that exhibit excellent flow behavior for the direct ink writing technique. Printed green bodies were dried gently, debinded and sintered to get undeformed and crack-free sintered parts. We manufactured cellular ceramics with fully open-porous struts (ε = 45-60%, $x_{50,3}$ < 6 µm) and overall porosities up to 88%. Hexagonal honeycomb samples from this process behave anisotropic under load and depending on loading direction compressive strength varies about a factor of 2-3. In-plane loaded honeycombs showed a specific strength that was up to a factor of 3 larger than that of slip-casted specimens from capillary suspensions. With this new concept it will be possible in the near future to manufacture cellular structures that combine the high specific strength of natural materials, e.g. like balsa wood, with the excellent thermal and chemical resistivity of glasses or ceramic materials.

8 Zusammenfassung

Erstmals im Jahr 2012 präsentierten Dittmann et al. [110] ein innovatives Verfahren zur Herstellung hochporöser keramischer Werkstoffe auf Basis sogenannter Kapillarsuspensionen als Precursor. Das neuartige Verfahren ermöglicht die Herstellung von makroporösen Sinterwerkstoffen mit variabler Mikrostruktur. So kann sowohl eine schmale Porengrößenverteilung im Porosität - Porengrößenbereich von $\varepsilon > 50\%$ bei $x_{50,3} < 10\ \mu m$ als auch eine definierte, breite Porengrößenverteilung eingestellt werden. Zahlreiche wissenschaftliche Studien untersuchten bereits die Grundlagen der Kapillarsuspensionen und auch das Verfahren zur Nutzung dieser als Precursor für Sinterwerkstoffe. Diese Dissertation ist eine experimentelle Arbeit mit Schwerpunkt auf der maßgeschneiderten Formulierung von Kapillarsuspensionen zum Einsatz in Produktanwendungen mit besonderen Materialeigenschaften, was bisher nicht im Mittelpunkt anderer wissenschaftlicher Arbeiten stand. Die Ergebnisse dieser kumulativen Dissertation wurden in drei Teile unterteilt.

Der **erste Teil** dieser Arbeit konzentriert sich auf die Untersuchung des Einflusses der Partikelform auf Rheologie und Struktur von Kapillarsuspensionen. Wissenschaftliche Arbeiten fokussierten sich bisher primär auf Suspensionen mit kugelförmigen oder nahezu isometrischen Partikeln und vernachlässigten den Einfluss der Partikelform gänzlich. In dieser Arbeit wurden erstmals Kapillarsuspensionen aus Partikeln mit unterschiedlicher Form systematisch untersucht, wobei große Unterschiede in der Rheologie und der Mikrostruktur beobachtetet wurden. So konnte bei nadelförmigen oder skalenoedrischen Calciumcarbonat Partikeln keine Ausbildung des für Kapillarsuspensionen typischen Partikelnetzwerks beobachtet werden. Im Gegensatz dazu zeigten dreiphasige Suspensionen aus kugelförmigen und plättchenförmigen Partikeln deutlich die drei charakteristischen Regimes in Fließgrenze σ_y und Speichermodul G‘ bei variiertem Zweitflüssigkeitsanteil ϕ_{sec}. Die Ausprägung der Regimes unterscheidet sich je nach Partikelform signifikant, was nur durch Unterschiede in der Form der Kapillarbrücken zu erklären ist. Eine besondere Form der Kapillarbrücken zwischen plättchenförmigen Partikeln könnte dazu führen, dass diese eine deutlich größere Menge an Zweitflüssigkeit aufnehmen können bis die typische sphärische Agglomeration eintritt als dies beispielsweise bei kugelförmigen Partikeln der Fall ist. Äquivalente Ergebnisse zeigten Untersuchungen an Suspensionen aus kugelförmigen und plättchenförmigen Graphitpartikeln welche ein von einem an der Studie mitwirkenden Wissenschaftler durchgeführt wurden. Diese Ergebnisse unterstreichen deutlich den Einfluss und die Relevanz der Partikelform für die maßgeschneiderte Entwicklung von Produkten auf Basis von Kapillarsuspensionen.

Der Fokus des **zweiten Teils** dieser Dissertation liegt auf Festkörpern auf Basis von Kapillarsuspensionen. Dabei wurden hier Festkörper mit einer verbesserten Mikrostruktur, die zu einer hohen Permeabilität und einer gesteigerten mechanischen Festigkeit führt, hergestellt und charakterisiert.

Zunächst wird in *Kapitel 3* ein innovatives, neuartiges Verfahren präsentiert das sich zur Herstellung von gesinterten Glasfiltern auf Basis von Kapillarsuspensionen mit einer Porosität ≥ 50 % bei einer mittleren Porengröße von 1 – 50 µm eignet. Dieses neuartige Verfahren wurde zusammen mit weiteren Wissenschaftlern entwickelt, während die maßgebliche Konzeption, die Umsetzung und insbesondere die Optimierung des Verfahrens zur Herstellung herausragender Sinterfilter vom Autor dieser Dissertation erfolgten. Die Glasfilter besitzen eine sehr schmale Porengrößenverteilung mit einer äußerst gleichmäßigen und runden Porenstruktur. Aufgrund dieser sehr glatten Porenstruktur wiesen die Filter eine hohe Permeabilität und eine große mechanische Festigkeit auf. Bei konstanter Porosität erreichten die Glasfilter so eine mechanische Festigkeit die vergleichbar mit keramischen Materialien war, obwohl diese über eine deutlich größere Matrixfestigkeit verfügten. Untersuchungen der Flüssigkeits- und Gaspermeabilität zeigten deutlich, dass die neuartigen Glasmembranen keramische und kommerzielle Glasmembranen auch diesbezüglich übertreffen. Dies wurde insbesondere bei kleinen Porengrößen $x_{50,3}$ < 10 µm sichtbar. Die sehr glatte, homogene Porenstruktur verschafft den neuen Glasfiltern einen signifikanten Vorteil gegenüber den Benchmark-Produkten.

Im *vierten Kapitel* stellen wir ein neues Konzept zur Herstellung von Festkörpern mit sehr guter mechanischer Festigkeit und hoher Porosität vor, das für eine Vielzahl an Materialien angewendet werden kann. In einer Zusammenarbeit mehrerer Wissenschaftlern wurden zur Herstellung dieser Festkörper sogenannte „smart capillary suspensions“ entwickelt in welchen die Zweitphase als Träger für aktive Substanzen dient. Diese sind beispielsweise Reaktivharze, organische Lösungsmittel oder kleine sinteraktive Partikel. Die selbstorganisierte Verteilung der Zweitphase ermöglicht den Transport der aktiven Substanzen exakt zu den Stellen an welchen diese aktiv wirken können: Die Kontaktstellen zwischen den Partikeln, welche anschließend gesintert, verschweißt oder verklebt werden sollen. Ein erstes Beispiel zeigt die Herstellung von hochporösen Graphitmembranen durch den Einsatz eines Reaktivharzes als Zweitphase in einer Suspension aus plättchenförmigen Graphitpartikeln. Nach Aushärten des Harzes wiesen die somit über Punktverklebung hergestellten Membranen sehr gute Eigenschaften hinsichtlich mechanischer Festigkeit (bis zu 1 MPa) und Porenstruktur auf (ε = 60-75 %, $x_{50,3}$ = ~15 µm). Ein weiteres Beispiel, welches vollständig vom Autor dieser Dissertation entwickelt und durchgeführt wurde, zeigt ein Verfahren zur Herstellung von Membranen aus UHMWPE, einem Polyethylen mit sehr hohem Molekulargewicht das äußerst schwer zu Produkten verarbeitbar ist. Der Einsatz

eines organischen Lösungsmittels (m-Xylol oder Paraffinöl) als Zweitphase in einer Kapillarsuspension aus UHMWPE-Partikeln, ermöglichte, verglichen zu herkömmlichen Sinterverfahren, die Sintertemperatur des Materials um bis zu 40 K abzusenken. Über dieses Verfahren hergestellte Membranen wiesen eine äußerst glatte Porenstruktur und eine hohe Porosität von > 62% auf. In einem dritten Ansatz, in welchem der Autor dieser Doktorarbeit in Teilen mitwirkte, wurde die Zweitflüssigkeit als Träger einer Fraktion feiner, sehr sinteraktiver Partikel eingesetzt. Mit Hilfe dieser Strategie konnten bei deutlich reduzierter Sintertemperatur poröse keramische Körper mit glatter Porenstruktur und außergewöhnlich hoher Festigkeit hergestellt werden.

Im **dritten Teil** dieser Dissertation werden zwei Konzepte zur Nutzung von Kapillarsuspensionen in Produktanwendungen vorgestellt: Zunächst ein Verfahren zur Herstellung rissfreier, dünner Beschichtungen und anschließend ein Verfahren zur Produktion 3D-gedruckter Leichtbaukomponenten.

Kapitel 5 zeigt die Möglichkeiten und Vorteile von Kapillarsuspensionen zur Herstellung dünner Beschichtungen. Herkömmliche Pasten für Beschichtungen neigen sehr häufig zur Bildung von Trocknungsrissen, wodurch die Funktion der Schichten teilweise oder vollständig beeinträchtigt wird. Mit Hilfe des Kapillarsuspension-Konzepts konnten wir jedoch rissfreie Beschichtungen in Schichtdicken herstellen, die die kritische Rissdicke von herkömmlichen Suspensionen deutlich übersteigen. Die starken Kapillarkräfte die in Kapillarsuspensionen vorherrschen, ermöglichen die Erhaltung die Partikel-Partikel Kontakte, modifizieren die Mikrostruktur und abhängig von der Wahl der Zweitflüssigkeit können diese auch die Trocknungsrate erhöhen. Die rissfreien Beschichtungen können sogar in den gesinterten Zustand überführt werden, wie wir anhand eines Modellsystems aus Al_2O_3 Partikeln zeigten. Dünne Schichten zahlreicher Materialien wurden hergestellt, getrocknet und charakterisiert. Nickel Beschichtungen wurden auf ihre elektrische Leitfähigkeit untersucht und gesinterte, poröse Schichten aus Al_2O_3 wurden in Filtrationstests hinsichtlich Permeabilität und minimaler Trenngrenze untersucht. Wie in Teilen der vorangehendenden Untersuchungen stammen auch wissenschaftliche Ergebnisse dieses Kapitels aus einer engen Zusammenarbeit mehrerer Wissenschaftler. Die Konzeption und die Durchführung von Untersuchungen an Beschichtungen aus Al_2O_3-Partikeln stammen jedoch nahezu vollständig vom Autor dieser Dissertation.

Ein innovatives Verfahren zur additiven Herstellung von komplexen keramischen Strukturen mit hierarchischer Porenstruktur, die sich besonders für den Einsatz im Leichtbaubereich eignen, wird in *Kapitel 6* vorgestellt. Hierzu wurden zunächst spezielle Pasten auf Basis von Kapillarsuspensionen entwickelt die optimale Fließeigenschaften zur Verarbeitung im sog. Direkten Tintenschreiben (engl.: Direct Ink Writing) haben. Mit Hilfe eines ausgeklügelten

Verfahrens konnten die gedruckten Grünkörper getrocknet, entbindert und gesintert werden ohne, dass es zu einer Beschädigung der Probekörper durch Rissbildung oder Deformationen kam. Die zellulären keramischen Körper wiesen eine Gesamtporosität von bis zu 88% und vollständig offenporige Stege auf (ε = 45-60%, $x_{50,3}$ < 6 µm). Keramische Sinterkörper in Form von hexagonalen Honigwaben verhielten sich in Belastung stark anisotrop und abhängig von der Belastungsrichtung variierte die Druckfestigkeit um Faktor 2-3. Honigwaben die senkrecht zur Ausrichtung der Honigwaben belastet wurden zeigten eine spezifische Festigkeit die um bis zu Faktor 3 größer war als herkömmliche Sinterkörper auf Basis von Kapillarsuspensionen. Mit Hilfe dieses neuen Herstellungsverfahrens könnte die die Herstellung von zellulären Strukturen, die die hohe spezifische Festigkeit von Biomaterialien wie z.B. Balsaholz, mit der thermischen und chemischen Beständigkeit von Glas- oder Keramikmaterialien vereinigen, bereits in naher Zukunft möglich sein.

9 Outlook

9.1 Innovative filter geometries

We introduced a simple method for manufacturing ceramic and glass filter disks that show excellent filtration behavior due to a smooth and homogeneous pore structure. However, due to their simple disk shape they are barely relevant for industrial applications. Industrial relevance for this filter media may be reached if processing techniques are developed that enable the manufacturing of more complex filtration modules. Following studies could focus on the development of an extrusion process that allows for manufacturing capillary suspension based hollow tubes or hollow fibers. These filter modules may be further coated with a thin, fine pored membrane layer that guarantees a good particle separation at a high volumetric flow rate of the filtrate.

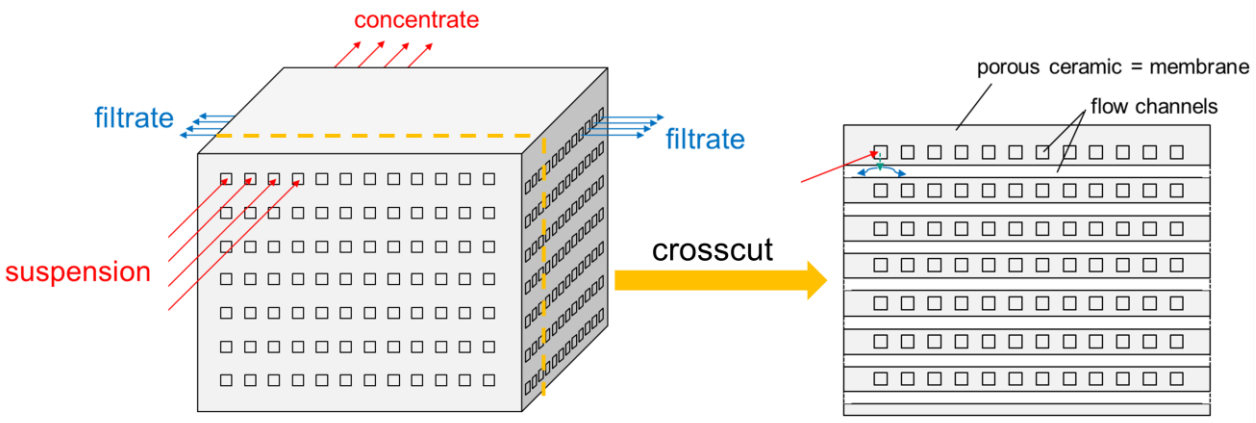

Fig. 57: Schematic of a cross-flow filter that may be 3D printed with capillary suspension based inks.

3D printing of capillary suspension based pastes may be an interesting method for manufacturing even more complex filter geometries, like crossflow filters. Fig. 57 shows a schematic of a model filter that may be realized with the fully open porous structure of sintered capillary suspensions. The model filter introduces a new kind of a crossflow-filter with a high number of parallel feed channels and orthogonal filtrate channels. This filter can be used for filtration/purification or concentration purposes. A pressure difference between feed and filtrate channels will prohibit backmixing between the two types of flow channels. The model filter can be flanged easily to an appropriate pipe system, thus sealing of each single flow channel separately will not be necessary. This new ceramic crossflow-filter may be used in the field of microfluidics, for filtration processes at high temperatures (e.g. hot-gas filtration) or where

chemically aggressive media are filtered or used as cleaning agents. One example is the filtration of fruit juice, where usually aggressive chemicals are used to clean the filter from fouling layers.

9.2 Catalytic applications

Ceramics based on capillary suspensions exhibit a fully open porous microstructure and a high inner surface. This microstructure has ideal properties for the application in catalytic purposes, i.e. as catalyst supports. Therefore, the high inner surface of the sintered parts can be coated with a catalytic active material via common coating techniques, like chemical vapor deposition (CVD) [223–225] or wash coatings [225]. The open-porous structure guarantees a good accessibility of the deposited active material by the reactants.

A further approach to make catalytically active sintered parts based on capillary suspensions could be to use catalytically active particles directly in the ceramic precursor suspension. Consequently, the coating step of the specimens with a catalytic active material may be skipped. The challenge will be the transfer of the particle network into a sintered body without changing the catalytic properties. Zeolite particles are one example of a catalytically active material that might serve as solid phase in the suspensions. Zeolites are microporous aluminosilicates with a high inner surface that are often used for catalysis. The main challenge, here, will be the sintering step, since zeolite particles are very sensitive to high temperatures. A drastic decrease of the specific inner surface area is supposed to occur even before reaching the sintering temperature of the particles ($T < 1000°C$). A way to treat with this problem could be the *smart capillary suspension concept* [41] as introduced in chapter 4 of this thesis: Small particles with a high sinter activity can be deposited at the contact points of the larger zeolite particles using the secondary liquid as carrier. This allows for decreasing the sintering temperature of the sample significantly ($T_{sinter} < 800°C$). This concept could allow for manufacturing mechanically stable and catalytic active parts in one step.

Both concepts may be combined with the 3D printing technique, introduced in chapter 6. Further investigations should focus on the development of capillary suspension based inks that are appropriate for catalytic purposes, and on the design of catalyst geometries that can be exclusively processed via 3D printing. The flexibility in design may allow for creating catalyst supports with optimized perfusion properties. Hardly accessible active centers that lead to diffusion limits and consequently to lower yields or a poor selectivity may be avoided.

9.3 Lightweight construction materials

Further research should focus on strategies to create 3D printed cellular structures with further increased mechanical strength. A great challenge will be manufacturing of lightweight construction materials with specific strength that is close to that of Balsa wood, one of the prime examples for natural cellular materials with unique specific strength [200]. The cellular structures that were printed in preliminary studies (cf. chapter 6 or [43]) already show excellent mechanical efficiency and strength. Further studies should try to increase the strut strength of the printed lattice structures. A possible approach for reaching higher strut strengths is to decrease the pore roughness of the porous structures, as was already shown for porous bulk parts by using glass particles (cf. chapter 3 or [40]) or by the *smart capillary suspension concept* (cf. chapter 4 or [41]). The former concept is of special interest since the application of glass particles additionally decreases the density ρ^* of the sintered samples by about 30%.

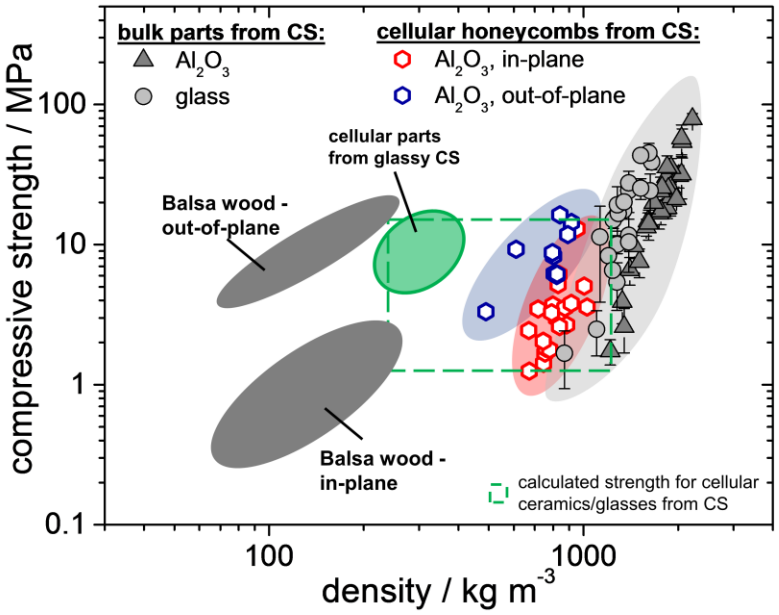

Fig. 58: Compressive strength as a function of density of cellular materials manufactured via DIW after [200]. Data from bulk parts based on capillary suspensions (=CS) is from [16,40] and data from cellular honeycombs based on CS are from [43]. The green shaded area shows the expected mechanical strength of DIW processed lightweight structures based on capillary suspensions with improved microstructure and reduced density (e.g. with glass particles). Densities are calculated, assuming printed cellular parts with a scaffold porosity of 55-80% and a strut porosity of 30-70%. Mechanical strength values are extrapolated from [16,40] using the Gibson&Ashby model for open-cellular materials [19].

Fig. 58 shows compressive strength data of capillary suspension based ceramics from previous publications [16,40]. The green marked strength-density area predicts the field that might be accessible by 3D printed ceramics or glasses based on capillary suspensions. Therefore, the

Gibson & Ashby model for open-porous, brittle fracturing materials was applied on data from porous ceramic and glass parts of [16,40]. The strength data of 3D printed, cellular ceramics presented in chapter 6 fits excellent into the calculated area. In future work that focusses on higher strut strengths, the green shaded area close to balsa wood might be accessible.

10 Bibliography

[1] O. Şan, C. Özgür, J. Memb. Sci. 305 (2007) 169–175.
[2] C. Özgür, O. Şan, Ceram. Int. 37 (2011) 965–970.
[3] A. Lehtovaara, W. Mojtahedi, Bioresour. Technol. 46 (1993) 113–118.
[4] F.A. Acosta, A.H. Castillejos, J.M. Almanza, A. Flores, Metall. Mater. Trans. B. 26 (1995) 159–171.
[5] A. Cybulski, J.A. Moulijn, Structured Catalysts and Reactors, CRC Press, 2005.
[6] P. Colombo, Philos. Trans. R. Soc. A. 364 (2006) 109–124.
[7] C. Migliaresi, A. Motta, Scaffolds for Tissue Engineering: Biological Design, Materials, and Fabrication, Pan Stanford Publishing, 2014.
[8] G. Vunjak-Novakovic, R.I. Freshney, Culture of Cells for Tissue Engineering, Wiley-Liss, New Jersey, USA, 2006.
[9] M.F. Ashby, Materials Selection in Mechanical Design, third Edit, Elsevier, 2005.
[10] J. Dittmann, E. Koos, N. Willenbacher, J. Am. Ceram. Soc. 96 (2013) 391–397.
[11] E. Koos, N. Willenbacher, Science. 331 (2011) 897–900.
[12] S. Wollgarten, C. Yuce, E. Koos, N. Willenbacher, Food Hydrocoll. 52 (2016) 167–174.
[13] S. Hoffmann, E. Koos, N. Willenbacher, Food Hydrocoll. 40 (2014) 44–52.
[14] M. Schneider, E. Koos, N. Willenbacher, Sci. Rep. 6 (2016) 1–10.
[15] B. Bitsch, J. Dittmann, M. Schmitt, P. Scharfer, W. Schabel, N. Willenbacher, J. Power Sources. 265 (2014) 81–90.
[16] J. Dittmann, N. Willenbacher, J. Am. Ceram. Soc. 97 (2014) 3787–3792.
[17] T. Ohji, M. Fukushima, Int. Mater. Rev. 57 (2012) 115–131.
[18] C. Minas, D. Carnelli, E. Tervoort, A.R. Studart, Adv. Mater. (2016).
[19] L. Gibson, M. Ashby, Cellular Solids: Structure and Properties, Cambridge University Press, Cambridge, UK, 1997.
[20] A.G. Fane, R. Wang, M.X. Hu, Angew. Chemie - Int. Ed. 54 (2015) 3368–3386.
[21] Grand View Research, (2016). https://www.grandviewresearch.com/industry-analysis/catalyst-market.
[22] A.R. Studart, U. Gonzenbach, E. Tervoort, L. Gauckler, J. Am. Ceram. Soc. 89 (2006) 1771–1789.
[23] I. Akartuna, A.R. Studart, E. Tervoort, L.J. Gauckler, Adv. Mater. 20 (2008) 4714–4718.
[24] A. Imhof, D.J. Pine, Nature. 389 (1997) 948–951.
[25] V.N. Manoharan, A. Imhof, J.D. Thorne, D.J. Pine, Adv. Mater. 13 (2001) 447–450.
[26] F. Bossler, E. Koos, Langmuir. 32 (2016) 1489–1501.
[27] W. Pietsch, H. Rumpf, Chemie Ing. Tech. 15 (1967) 885–893.
[28] E. Koos, W. Kannowade, N. Willenbacher, Rheol. Acta. 53 (2014) 947–957.
[29] E. Koos, J. Johannsmeier, L. Schwebler, N. Willenbacher, Soft Matter. 8 (2012) 6620.
[30] H.J. Butt, M. Kappl, Adv. Colloid Interface Sci. 146 (2009) 48–60.
[31] T. Domenech, S.S. Velankar, Soft Matter. 11 (2015) 1500–1516.
[32] C.D. Willett, M.J. Adams, S. a. Johnson, J.P.K. Seville, Langmuir. 16 (2000) 9396–9405.
[33] D. Megias-Alguacil, L.J. Gauckler, AIChE J. 55 (2009) 1103–1109.
[34] S. Strauch, S. Herminghaus, Soft Matter. 8 (2012) 8271.
[35] E. Koos, Curr. Opin. Colloid Interface Sci. 19 (2014) 575–584.
[36] J. Russ, R. Dehoff, Practical Stereology, Kluwer Academic / Plenum Publishers, 2000.
[37] B. Bitsch, B. Braunschweig, N. Willenbacher, Langmuir. 32 (2016) 1440–1449.
[38] F. Bossler, L. Weyrauch, R. Schmidt, E. Koos, Colloids Surfaces A Physicochem. Eng. Asp. 518 (2017) 1–40.
[39] J. Maurath, B. Bitsch, Y. Schwegler, N. Willenbacher, Colloids Surfaces A Physicochem. Eng. Asp. 497 (2016) 316–326.
[40] J. Maurath, J. Dittmann, N. Schultz, N. Willenbacher, Sep. Purif. Technol. 149 (2015)

470–478.
[41] J. Dittmann, J. Maurath, B. Bitsch, N. Willenbacher, Adv. Mater. 28 (2016) 1689–1696.
[42] M. Schneider, J. Maurath, S.B. Fischer, M. Weiß, N. Willenbacher, E. Koos, ACS Appl. Mater. Interfaces. 9 (2017) 11095–11105.
[43] J. Maurath, N. Willenbacher, J. Eur. Ceram. Soc. 37 (2017) 4833–4842.
[44] F. Dullien, Porous Media: Fluid Transport and Pore Structure, 2nd editio, Academic Press Inc., San Diego, 1992.
[45] F.A.L. Dullien, AIChE J. 21 (1975) 299–307.
[46] S.S. Velankar, Soft Matter. 11 (2015) 8393–8403.
[47] S.J. Heidlebaugh, T. Domenech, S. V Iasella, S.S. Velankar, Langmuir. 30 (2014) 63–74.
[48] E. Koos, N. Willenbacher, Soft Matter. 8 (2012) 3988.
[49] S. Herminghaus, Adv. Phys. 54 (2005) 221–261.
[50] H.J. Butt, Langmuir. 24 (2008) 4715–4721.
[51] T.P. Farmer, J.C. Bird, J. Colloid Interface Sci. 454 (2015) 192–199.
[52] H. Schubert, Powder Technol. 37 (1984) 105–116.
[53] E.B. Webb, C. a Koh, M.W. Liberatore, Ind. Eng. Chem. Res. 53 (2014) 6998–7007.
[54] Y. Zhang, M.C. Allen, R. Zhao, D.D. Deheyn, S.H. Behrens, J.C. Meredith, Langmuir. 31 (2015) 2669–2676.
[55] Y. Zhang, J. Wu, H. Wang, J.C. Meredith, S.H. Behrens, Angew. Chemie. 126 (2014) 13603–13607.
[56] T. Domenech, S. Velankar, Rheol. Acta. 53 (2014) 593–605.
[57] J. Xu, L. Chen, H. Choi, H. Konish, X. Li, Sci. Rep. 3 (2013) 1730.
[58] G.B. Jeffery, Proc. R. Soc. A. 102 (1922) 161–179.
[59] G.I. Taylor, Proc. R. Soc. London A. 138 (1932) 41–48.
[60] J.M. Rallison, J. Fluid Mech. 84 (1978) 237–263.
[61] S. Haber, H. Brenner, J. Colloid Interface Sci. 97 (1984) 496–514.
[62] H. Brenner, Int. J. Multiph. Flow. 1 (1974) 195–341.
[63] I. Santamaría-Holek, C.I. Mendoza, J. Colloid Interface Sci. 346 (2010) 118–126.
[64] H. Giesekus, Disperse Systems: Dependence of Rheological Properties on the Type of Flow with Implications for Food Rheology, in: R. Jowitt (Ed.), Phys. Prop. Foods, Applied Science Publishers, 1983.
[65] A.B.D. Brown, S.M. Clarke, P. Convert, A.R. Rennie, J. Rheol. 44 (2000) 221–233.
[66] S. Yamamoto, T. Matsuoka, Comput. Mater. Sci. 14 (1999) 169–176.
[67] W. Pabst, E. Gregorová, C. Berthold, J. Eur. Ceram. Soc. 26 (2006) 149–160.
[68] H.A. Barnes, J.F. Hutton, K. Walters, An Introduction to Rheology, 3rd ed., Elsevier, Amsterdam, London, New York,Tokyo, 1993.
[69] D.A. Weitz, Science. 303 (2004) 968–969.
[70] R.G. Larson, The structure and rheology of complex fluids, Oxford University Press, New York, USA, 1999.
[71] J. Mewis, N.J. Wagner, Colloidal Suspension Rheology, Cambridge University Press, New York, USA, 2012.
[72] R. Faddoul, N. Reverdy-Bruas, A. Blayo, Mater. Sci. Eng. B. 177 (2012) 1053–1066.
[73] R. Faddoul, N. Reverdy-Bruas, A. Blayo, T. Haas, C. Zeilmann, Microelectron. Reliab. 52 (2012) 1483–1491.
[74] H. Mühlenweg, E.D. Hirleman, Part. Part. Syst. Char. 15 (1998) 163–169.
[75] Z. Ma, H.G. Merkus, J. de Smet, C. Heffels, B. Scarlett, Powder Technol. 111 (2000) 66–78.
[76] E. Halder, D.K. Chattoraj, K.P. Das, Indian J. Chem. - Sect. A Inorganic, Phys. Theor. Anal. Chem. 45 (2006) 2591–2598.
[77] Q. Nguyen, D. V. Boger, Annu. Rev. Fluid Mech. 24 (1992) 47–88.
[78] R. Brummer, Rheology Essentials of Cosmetic and Food Emulsions, Springer Berlin-Heidelberg, 2006.

[79] Y.G. Tselishchev, V.A. Val'tsifer, Colloid J. Russ. Acad. Sci. Kolloidn. Zhurnal. 65 (2003) 385–389.
[80] D. Megias-Alguacil, L.J. Gauckler, Powder Technol. 198 (2010) 211–218.
[81] S. Herminghaus, Wet Granular Matter: A Truly Complex Fluid, World Scientific, 2013.
[82] A. Donev, I. Cisse, D. Sachs, E. a Variano, F.H. Stillinger, R. Connelly, et al., Science. 303 (2004) 990–993.
[83] J. Li, C. Daniel, D. Wood, J. Power Sources. 196 (2011) 2452–2460.
[84] S. Faraji, F. Nasir, Renew. Sustain. Energy Rev. 42 (2015) 823–834.
[85] F. Cheng, J. Chen, Chem. Soc. Rev. 41 (2012) 2172.
[86] S. Litster, G. McLean, J. Power Sources. 130 (2004) 61–76.
[87] J.B. Xu, T.S. Zhao, RSC Adv. 3 (2012) 16–24.
[88] H. Harakawa, A. Kasari, A. Tominaga, M. Yatuba, Prog. Org. Coatings. 34 (1997) 84–90.
[89] S. Ripperger, J. Altmann, Sep. Purif. Technol. 26 (2002) 19–31.
[90] The Freedonia Group, Membrane Separation Technologies - industry study with forecasts for 2016 & 2021, 2012.
[91] B.K. Nandi, R. Uppaluri, M.K. Purkait, LWT - Food Sci. Technol. 44 (2011) 214–223.
[92] W. Yuan, Y. Tang, X. Yang, Z. Wan, Appl. Energy. 94 (2012) 309–329.
[93] T.F. Zhao, C.Q. Chen, Mech. Mater. 70 (2014) 33–40.
[94] J.C. Lee, H.J. You, H.S. Lee, M.C. Shin, J.S. Cha, S. Park, Colloids Surfaces A Physicochem. Eng. Asp. 241 (2004) 185–190.
[95] D.B. Purchas, K. Sutherland, Handbook of Filter Media, second edi, Elsevier Advanced Technology, Oxford, UK, 2002.
[96] N. Lifshutz, Int. Nonwovens J. 14 (2005) 18–23.
[97] A. Inayat, B. Reinhardt, H. Uhlig, W.-D. Einicke, D. Enke, Chem. Soc. Rev. (2013) 3753–3764.
[98] A.M.M. Santos, W.L. Vasconcelos, J. Non. Cryst. Solids. 273 (2000) 145–149.
[99] K. Sutherland, Filters and Filtration Handbook, fourth edi, Elsevier Advanced Technology, Oxford, UK, 2008.
[100] B. Reinhardt, J. Herwig, S. Rannabauer, M. Scheffler, D. Enke, J. Eur. Ceram. Soc. 34 (2014) 1465–1470.
[101] A. Sadighzadeh, M. Ghoranneviss, A. Salar Elahi, J. Porous Mater. 21 (2014) 993–999.
[102] M. Bortolotti, M. Brugnara, C. Della Volpe, S. Siboni, J. Colloid Interface Sci. 336 (2009) 285–297.
[103] E. Roos, K. Maile, Werkstoffkunde für Ingenieure: Grundlagen, Anwendung, Prüfung, 4th editio, Berlin Heidelberg, 2011.
[104] G. Hauser, Hygienische Produktionstechnologie, Wiley-VCH Verlag, Weinheim, 2008.
[105] W. Tanikawa, T. Shimamoto, Hydrol. Earth Syst. Sci. (2006).
[106] J. Bear, Dynamics of Fluids in Porous Media, American Elsevier Publishing Company Inc., New York, USA, 1972.
[107] M. Sahimi, Flow and Transport in Porous Media and Fractured Rock, 2nd editio, Wiley-VCH, Weinheim, 2011.
[108] U.T. Gonzenbach, A.R. Studart, E. Tervoort, L.J. Gauckler, J. Am. Ceram. Soc. 90 (2007) 16–22.
[109] S. Woyansky, C.E. Scott, W.P. Minnear, Am. Ceram. Soc. Bull. 71 (1992) 1674–1682.
[110] J. Dittmann, B. Hochstein, E. Koos, N. Willenbacher, Verfahren zur Herstellung einer porösen Keramik und eines porösen polymeren Werkstoffes sowie damit erhältliche Keramiken und Werkstoffe, Ger. DE102011106834, 2012.
[111] M. Inagaki, J. Qiu, Q. Guo, Carbon N. Y. 87 (2015) 128–152.
[112] B. Nagel, S. Pusz, B. Trzebicka, J. Mater. Sci. 49 (2014) 1–17.
[113] R.W. Pekala, R.W. Hopper, J. Mater. Sci. 22 (1987) 1840–1844.
[114] J.H. Yang, G.Z. Yang, D.G. Yu, X. Wang, B. Zhao, L.L. Zhang, et al., Carbon N. Y. 53 (2013) 231–236.

[115] X. Kuang, G. Carotenuto, L. Nicolais, Adv. Perform. Mater. 4 (1997) 257–274.
[116] S. Ramesh, K.L. Aw, C.H. Ting, C.Y. Tan, I. Sopyan, W.D. Teng, Adv. Mater. Res. 47–50 (2008) 801–804.
[117] R. Telle, H. Salmang, H. Scholze, Keramik, 7th ed., Springer Verlag Berlin Heidelberg, 2007.
[118] S. Spiegelberg, Characterization of Physical, Chemical and Mechanical Properties of UHMWPE, in: S.M. Kurtz (Ed.), UHMWPE Biomater. Handb., 2nd ed., Elsevier, Oxford, UK, 2009: pp. 355–368.
[119] S. Hambir, J.P. Jog, Bull. Mater. Sci. 23 (2000) 221–226.
[120] J.M. Kelly, J. Macromol. Sci. Part C Polym. Rev. 42 (2002) 355–371.
[121] B. Aydinli, T. Tincer, J. Appl. Polym. Sci. 59 (1996) 1489–1492.
[122] S. Santhanagopalan, Z. Zhang, Separators for Lithium-Ion Batteries, in: X. Yuan, H. Liu, J. Zhang (Eds.), Lithium-Ion Batter. Adv. Mater. Technol., CRC Press, 2011: pp. 198–244.
[123] K. Boahene, Synthetic Implants, in: I. Papel (Ed.), Facial Plast. Reconstr. Surg., 3rd ed., Thieme Medical Publishers, 2009: pp. 67–75.
[124] M. Scheffler, P. Colombo, Cellular Ceramics: Structure, Manufacturing, Properties and Applications, Wiley, Weinheim, Germany, 2005.
[125] R.W. Rice, J. Am. Ceram. Soc. 76 (1993) 1801–1808.
[126] F.P. Knudsen, J. Am. Ceram. Soc. 42 (1959) 367–387.
[127] S. Kwon, G. Messing, J. Mater. Sci. 33 (1998) 913–921.
[128] J. Smith, G. Messing, J. Am. Ceram. Soc. 67 (1984) 238–242.
[129] R.H.J. Hannink, P.M. Kelly, B.C. Muddle, J. Am. Ceram. Soc. 83 (2004) 461–487.
[130] W.H. Tuan, R.Z. Chen, T.C. Wang, C.H. Cheng, P.S. Kuo, J. Eur. Ceram. Soc. 22 (2002) 2827–2833.
[131] L. Heymann, S. Peukert, N. Aksel, Rheol. Acta. 41 (2002) 307–315.
[132] S. Mueller, E.W. Llewellin, H.M. Mader, Proc. R. Soc. A. 466 (2010) 1201–1228.
[133] H.D. Dörfler, Interfaces and Colloid-Disperse Systems: Physics and Chemistry, Springer, Heidelberg Berlin, Germany, 2002.
[134] T.G. Metzger, The Rheology Handbook, Vincentz Network, Hannover, Germany, 2011.
[135] N. Mathews, Y.M. Lam, S.G. Mhaisalkar, A.C. Grimsdale, Int. J. Mater. Res. 101 (2010) 236–250.
[136] F. Juillerat, P. Bowen, H. Hofmann, Langmuir. 22 (2006) 2249–2257.
[137] J.H. Park, J.H. Cho, W. Park, D. Ryoo, S.J. Yoon, J.H. Kim, et al., J. Power Sources. 195 (2010) 8306–8310.
[138] M. Bardosova, F.C. Dillon, M.E. Pemble, I.M. Povey, R.H. Tredgold, J. Colloid Interface Sci. 333 (2009) 816–819.
[139] B.G. Prevo, E.W. Hon, O.D. Velev, J. Mater. Chem. 17 (2007) 791.
[140] J. Zarzycki, M. Prassas, J. Phalippou, J. Mater. Sci. 17 (1982) 3371–3379.
[141] E.R. Dufresne, D.J. Stark, N. a. Greenblatt, J.X. Cheng, J.W. Hutchinson, L. Mahadevan, et al., Langmuir. 22 (2006) 7144–7147.
[142] E.R. Dufresne, E.I. Corwin, N. Greenblatt, J. Ashmore, D.Y. Wang, a D. Dinsmore, et al., Phys. Rev. Lett. 91 (2003) 1–4.
[143] Y. Xu, G.K. German, A.F. Mertz, E.R. Dufresne, Soft Matter. 9 (2013) 3735–3740.
[144] W. Man, W. Russel, Phys. Rev. Lett. 100 (2008) 198302.
[145] G.W. Scherer, J. Am. Ceram. Soc. 73 (1990) 3–14.
[146] A. Nakahara, Y. Matsuo, J. Stat. Mech. Theory Exp. 2006 (2006) P07016–P07016.
[147] P. Fratzl, H.S. Gupta, F.D. Fischer, O. Kolednik, Adv. Mater. 19 (2007) 2657–2661.
[148] V.R. Dugyala, H. Lama, D.K. Satapathy, M.G. Basavaraj, Nat. Publ. Gr. (2016) 1–7.
[149] M.A. Winnik, Curr. Opin. Colloid Interface Sci. 2 (1997) 192–199.
[150] A.M. Almanza-Workman, C.P. Taussig, A.H. Jeans, R.L. Cobene, J. Mater. Chem. 21 (2011) 14185–14192.
[151] F. Boulogne, F. Giorgiutti-Dauphiné, L. Pauchard, Oil Gas Sci. Technol. - Rev. IFP

Energies Nouv. 69 (2013) 397–404.
[152] M.I. Smith, J.S. Sharp, Langmuir. 27 (2011) 8009–8017.
[153] X. Tang, Surf. Coatings Technol. 221 (2013) 37–43.
[154] E.J. Kappert, D. Pavlenko, J. Malzbender, A. Nijmeijer, N.E. Benes, P.A. Tsai, Soft Matter. 11 (2015) 882–8.
[155] J.H. Prosser, T. Brugarolas, S. Lee, A.J. Nolte, D. Lee, Nano Lett. 12 (2012) 5287–5291.
[156] L. Wang, X.S. Zhao, J. Phys. Chem. C. 111 (2007) 8538–8542.
[157] E. Santanach Carreras, F. Chabert, D.E. Dunstan, G. V. Franks, J. Colloid Interface Sci. 313 (2007) 160–168.
[158] T. Kanai, T. Sawada, Langmuir. 25 (2009) 13315–13317.
[159] J.Y. Kim, K. Cho, S. Ryu, S.Y. Kim, B.M. Weon, Sci. Rep. (2015) 1–9.
[160] M. Schneider, E. Koos, N. Willenbacher, Sci. Rep. 6 (2016) 31367.
[161] Q. Jin, P. Tan, A.B. Schofield, L. Xu, Eur. Phys. J. E. 36 (2013) 1–5.
[162] R.C. Chiu, M.J. Cima, J. Am. Ceram. Soc. 76 (1993) 2769–2777.
[163] K. Singh, M. Tirumkudulu, Phys. Rev. Lett. 98 (2007) 218302.
[164] K.B. Singh, L.R. Bhosale, M.S. Tirumkudulu, Langmuir. 25 (2009) 4284–4287.
[165] V.P. Mehrotra, K.V.S. Sastry, Powder Technol. 25 (1980) 203–214.
[166] C. Gao, Appl. Phys. Lett. 71 (1997) 1801–1803.
[167] H.-J.J. Butt, Langmuir. 24 (2008) 4715–4721.
[168] F. Brochard-Wyart, J.M. Di Meglio, D. Quere, P.G. De Gennes, Langmuir. 7 (1991) 335–338.
[169] H.-J. Butt, K. Graf, M. Kappl, Physics and Chemistry of Interfaces, 3rd ed., Wiley-VCH, Weinheim, Germany, 2013.
[170] K. Yamamoto, C. Tanuma, N. Gemma, Jpn. J. Appl. Phys. 34 (1995) 4176.
[171] W. Pietsch, Chemie Ing. Tech. 15 (1967) 885–893.
[172] H. Weingärtner, Chemische Thermodynamik: Einführung für Chemiker und Chemieingenieure, 1., B. G. Teubner Verlag, 2003.
[173] C.K. Ho, K.S. Udell, Int. J. Heat Mass Transf. 38 (1995) 339–350.
[174] J. Schwarzbach, E.U. Schlünder, Chem. Eng. Process. Process Intensif. 32 (1993) 13–32.
[175] H.J. Vogel, H. Hoffmann, K. Roth, Geoderma. 125 (2005) 203–211.
[176] R.C. Chiu, T.J. Garino, M.J. Cima, J. Am. Ceram. Soc. 76 (1993) 2257–2264.
[177] M.S. Tirumkudulu, W.B. Russel, Langmuir. 21 (2005) 4938–4948.
[178] L. Xu, S. Davies, A.B. Schofield, D.A. Weitz, Phys. Rev. Lett. 101 (2008) 94502.
[179] H. Günzler, H.-U. Gremlich, IR Spectroscopy An Introduction, Wiley-VCH Verlag GmbH, 2002.
[180] P.M. Kumar, S. Badrinarayanan, M. Sastry, Thin Solid Films. 358 (2000) 122–130.
[181] Y. Gao, Y. Masuda, Z. Peng, T. Yonezawa, K. Koumoto, J. Mater. Chem. 13 (2003) 608–613.
[182] A.H. Demond, A.S. Lindner, Environ. Sci. Technol. 27 (1993) 2318–2331.
[183] B.E. Lang, J. Chem. Data. 57 (2012) 2221–2226.
[184] J.W. Vanderhoff, E.B. Bradford, W.K. Barrington, J. Polym. Sci. 41 (1973) 155–174.
[185] A.F. Routh, Reports Prog. Phys. 76 (2013) 46603.
[186] J.T. Su, P.B. Duncan, A. Momaya, A. Jutila, D. Needham, J. Chem. Phys. 132 (2010) 44506.
[187] A.T. Florence, D. Attwood, Physicochemical Principles of Pharmacy, 5., Royal Pharmaceutical Society, London, 2011.
[188] S.G. Croll, J. Coatings Technol. 58 (1986).
[189] S.G. Croll, J. Coatings Technol. 59 (1987) 81–92.
[190] R.D. Deegan, O. Bakajin, T.F. Dupont, G. Huber, S.R. Nagel, T.A. Witten, Nature. 389 (1997) 827–829.
[191] P.J. Yunker, T. Still, M. a Lohr, a G. Yodh, Nature. 476 (2011) 308–311.

[192] J. Caro, Chem. Soc. Rev. 45 (2015) 3468–3478.
[193] B.J. Last, D.J. Thouless, Phys. Rev. Lett. 27 (1971) 1719–1721.
[194] K. Hauf, E. Koos, Chemie Ing. Tech. 88 (2016) 1361–1361.
[195] F. Akhtar, L. Andersson, S. Ogunwumi, N. Hedin, L. Bergström, J. Eur. Ceram. Soc. 34 (2014) 1643–1666.
[196] E.C. Hammel, O..-R. Ighodaro, O.I. Okoli, Ceram. Int. 40 (2014) 15351–15370.
[197] W.-Y. Yeong, W.Y. Yeong, C.-K. Chua, C.K. Chua, K.-F. Leong, K.F. Leong, et al., Trends Biotechnol. 22 (2004) 643–652.
[198] L.J. Gibson, J. R. Soc. Interface. 9 (2012) 2749–2766.
[199] N.A. Fleck, V.S. Deshpande, M.F. Ashby, Proc. R. Soc. A Math. Phys. Eng. Sci. 466 (2010) 2495–2516.
[200] B.G. Compton, J.A. Lewis, Adv. Mater. 26 (2014) 5930–5935.
[201] J.T. Muth, P.G. Dixon, L. Woish, L.J. Gibson, J.A. Lewis, Proc. Natl. Acad. Sci. 114 (2017) 1832–1837.
[202] A. Zocca, P. Colombo, C.M. Gomes, J. Günster, J. Am. Ceram. Soc. 98 (2015) 1983–2001.
[203] N. Guo, M.C. Leu, Front. Mech. Eng. 8 (2013) 215–243.
[204] B. Wendel, D. Rietzel, F. Kühnlein, R. Feulner, G. Hülder, E. Schmachtenberg, Macromol. Mater. Eng. 293 (2008) 799–809.
[205] J.I. Lipton, M. Cutler, F. Nigl, D. Cohen, H. Lipson, Trends Food Sci. Technol. 43 (2015) 114–123.
[206] VDI, Statusreport - Additive Fertigungsverfahren, 2014.
[207] K.F. Leong, C.M. Cheah, C.K. Chua, Biomaterials. 24 (2003) 2363–2378.
[208] J.A. Lewis, Adv. Funct. Mater. 16 (2006) 2193–2204.
[209] J. Deckers, J. Vleugels, J.-P. Kruth, J. Ceram. Sci. Technol. 5 (2014) 245–260.
[210] E.M. Sachs, M.J. Cima, P.A. Williams, D. Brancazio, J. Cornie, J. Manuf. Sci. Eng. 114 (1992) 481–488.
[211] J. Song, M. Edirisinghe, J. Evans, J. Am. Ceram. Soc. 82 (1999) 3374–3380.
[212] H. Seitz, U. Deisinger, B. Leukers, R. Detsch, G. Ziegler, Adv. Eng. Mater. 11 (2009) 41–46.
[213] A. Garcia, I. Izquierdo-Barba, M. Colilla, C.L. De Laorden, M. Vallet-Regi, Acta Biomater. 7 (2011) 1265–1273.
[214] Y.W. Moon, I.J. Choi, Y.H. Koh, H.E. Kim, Ceram. Int. 41 (2015) 12371–12377.
[215] Q. Fu, E. Saiz, A.P. Tomsia, Adv. Funct. Mater. 21 (2011) 1058–1063.
[216] J.E. Smay, J. Cesarano III, J.A. Lewis, Langmuir. 18 (2002) 5429–5437.
[217] J. Bauer, S. Hengsbach, I. Tesari, R. Schwaiger, O. Kraft, Proc. Natl. Acad. Sci. 111 (2014) 2453–2458.
[218] C. Polzin, D. Gunther, H. Seitz, J. Ceram. Sci. Technol. 6 (2015) 141–145.
[219] X. Zheng, H. Lee, T.H. Weisgraber, M. Shusteff, J. DeOtte, E.B. Duoss, et al., Science. 344 (2014) 1373–1377.
[220] L.R. Meza, S. Das, J.R. Greer, Science. 345 (2014) 1322–1326.
[221] M.F. Ashby, Philos. Trans. A. Math. Phys. Eng. Sci. 364 (2006) 15–30.
[222] Informationszentrum Technische Keramik, Brevier Technische Keramik, Fahner Verlag, Lauf, Germany, 2003.
[223] M. Faust, M. Seipenbusch, Surf. Coatings Technol. 259 (2014) 577–584.
[224] M. Faust, M. Enders, M. Bruns, S. Bräse, K. Gao, M. Seipenbusch, Surf. Coatings Technol. 230 (2013) 284–289.
[225] V. Meille, Appl. Catal. A Gen. 315 (2006) 1–17.

11 Verification of the contribution from the co-authors

This chapter is not included in the online version.